The Pennsylvania State University

The Graduate School

Department of Geosciences

MODELING NOVEL ISOTOPIC PROXIES OF THE OXYGENATION OF THE EARTH'S SURFACE

A Thesis in

Geosciences and Astrobiology

by

Shawn D. Domagal-Goldman

Submitted in Partial Fulfillment
of the Requirements
for the Degree of

Doctor of Philosophy

August 2007

The thesis of Shawn Domagal-Goldman was reviewed and approved* by the following:

James D. Kubicki
Associate Professor of Geochemistry
Thesis Co-Advisor
Co-Chair of Committee

James F. Kasting
Professor of Geosciences
Thesis Co-Advisor
Co-Chair of Committee

Michael A. Arthur
Professor of Geosciences

Jorge O. Sofo
Associate Professor of Physics
Associate Professor of Materials Science and Engineering

Timothy J. Bralower
Professor of Geosciences
Department Head

* Signatures are on file in the Graduate School

ABSTRACT

Tracking the evolution of the oxidation state of the Earth's surface environment has increased understanding of the biological, atmospheric, oceanic, and geological evolution of the Earth, and may allow us to broaden the search for life on extrasolar planets. In this thesis, two relatively new proxies for the evolution of the Earth's surface oxidation state are examined. Both proxies use stable isotope measurements to identify a permanent oxidation of the surface that occurred between ~2.4 and ~1.8 billion years ago (Ga).

Measurements of the stable isotopes of Fe (^{54}Fe, ^{56}Fe, and ^{57}Fe) in sediments demonstrate an increase in maximum ^{56}Fe/^{54}Fe prior to ~1.8 billion years ago (Ga) and an increase in the maximum and decrease in the minimum ^{56}Fe/^{54}Fe prior to ~2.3 Ga. These data have been interpreted as being the result of stepwise changes to the oxidation state of the Earth's oceans. However, the measurement of Fe isotopes has also been proposed as a way to identify a history of life in a sample, as Fe isotopes have been shown to fractionate during metabolic processes and upon complexation with organic acids. In the first two chapters of the thesis, the fractionation associated with complexation of Fe with organic ligands is modeled. Equilibrium constants are predicted for equilibrium isotope exchange for redox and ligand exchange reactions. These predictions allow comparison of these two types of fractionation and place the two proposed uses of Fe isotopes in better theoretical context.

Another novel tool for tracking the redox history of the Earth is the measurement of multiple S isotopes. In sediments younger than ~2.3 Ga, the fractionation of the stable

S isotopes (^{32}S, ^{33}S, ^{34}S, and ^{36}S) follows specific trends that depend on the mass of the isotopes. This behavior is classified as mass-dependent fractionation, and is witnessed for almost all known kinetic, equilibrium, and biological fractionation processes. However, sediments older than ~2.45 Ga do not follow this trend. As such they are said to exhibit mass-independent fractionation of Sulfur isotopes (S-MIF), a process that has been recreated in the laboratory using photolysis of SO_2 using UV light. The presence of S-MIF in these older rocks is commonly accepted as evidence that atmospheric O_2 concentrations permanently rose at ~2.4 Ga, establishing an ozone shield that shielded SO_2 from UV radiation and prevented the creation of S-MIF in the lower atmosphere. Subsequent analyses have uncovered secondary features in the S-MIF record. The most notable excursion is a decline in the magnitude of S-MIF between ~3.2 and ~2.7 Ga that has been used to invalidate the aforementioned use of S-MIF to date the rise of atmospheric O_2.

Chapter 3 proposes a new control on S-MIF – namely an organic haze that could have shielded SO_2 from UV radiation and prevented S-MIF in an anoxic atmosphere. This is modeled with a 1-dimensional photochemical code that predicts reaction rates for photolysis of SO_2. Chapter 4 examines the climatic implications of the haze and of other hydrocarbon species that would have been present in the Archean atmosphere, given the constraints placed by isotopic and other geochemical indicators. Finally, Chapter 5 summarizes this work by explaining Archean trends in C, S, and Fe isotopes with a sequence of changes to the Earth's biosphere, atmosphere, and climate.

TABLE OF CONTENTS

LIST OF FIGURES

LIST OF TABLES

PREFACE

Five chapters comprise this thesis, the first three of which are multi-authored papers previously submitted for publication. I am first author on all three papers, having prepared all three initial manuscripts. Chapters 4 and 5 are entirely my own work; the calculations for Chapter 4 are also included in an independent paper submitted to *Astrobiology* on which I am second author (that paper shares very little text with Chapter 4). Chapters 1 and 2 were submitted to *Geochimica et Cosmochimica Acta*, and Chapter 3 was submitted to *Earth and Planetary Science Letters*. All three chapters on which I am first author have undergone peer-review and have been re-submitted. The re-submitted versions of those three maunsrcipts on very closely resemble their corresponding chapters. The following delineates my contributions to those three manuscripts:

Chapter 1 **Density Functional Theory Predictions of Equilibrium Isotope Fractionation of Iron due to Redox Changes and Organic Complexation**

I and my co-advisor, Dr. James D. Kubicki, were the only two authors of this manuscript. All the work in Chapter 1 is the result of my research, guided by Dr. Kubcki and revised by Dr. Clark M. Johnson, Dr. Venimian B. Polyakov, Dr. Edwin Schauble and one anonymous reviewer. My former advisor, Dr. Ariel Anbar, independently reviewed the manuscript and provided us with questions that drove some of the work done during revisions.

Chapter 2 **Molecular Modeling of the Fe(III)-Desferrioxamine B Siderophore Complex – Electronic Structure, IR Vibrational Frequencies, and Equilibrium Fractionation in Solution**

Dr. Kubicki and I collaborated with Dr. Kris W. Paul and Dr. Don L. Sparks on this paper; Dr. Paul and Dr. Sparks provided the calculations described in the methods section of the manuscript; I wrote the first interpretations of all data. Dr. Kubicki and Dr. Paul provided substantial advice for revisions of this manuscript, as did three anonymous reviewers.

Chapter 3 **Organic Haze, Glaciations and Multiple Sulfur Isotopes**

I wrote this paper under the guidance of my other co-advisor, Dr. James F. Kasting. Because we were attempting to model long-term trends in sulfur isotope data, we asked Dr. David T. Johnston and Dr. James Farquhar, two experts on the subject, to collaborate with us on the project. The data presented in Table 3-1, Figure 3-1, and Figure 3-6 are primarily the work of Dr. Johnston and Dr. Farquhar, as are the corresponding sections of text discussing these data. The 1-D photochemical model results are my own work, and the interpretation of the results stem from a collaborative effort of all four authors.

ACKNOWLEDGEMENTS

I would like to acknowledge financial support from the ACS Petroleum Research Fund grant on "Experimental and Theoretical Investigation on Adsorption of Extracellular Compounds onto Mineral Surfaces," the Penn State Astrobiology Research Center (PSARC), the NASA Exobiology program, and the NASA Astrobiology Institute (NAI). Computational support was provided by the Center for Materials Simulation (CEMS) – a PSU MRSEC facility, and the Center for Environmental Kinetics Analysis (CEKA) at PSU – an NSF/DOE Environmental Molecular Sciences Institute.

I extend my sincere appreciation and gratitude to my colleagues. My two advisors, Dr. James D. Kubicki and Dr. James F. Kasting, are foremost in this regard as their guidance was a major driver of my progress in completing this manuscript. The following collaborators also deserve a great deal of credit for assisting me with the ideas and text presented within this document: Dr. David T. Johnston, Dr. Kris W. Paul, Dr. James Farquhar, Jacob Haqq-Misra, and Dr. Don L. Sparks. Finally, I would like to acknowledge the efforts of my Master's advisor, Dr. Ariel D. Anbar, who recruited me into the field and sparked my interest in stable isotopes and the evolution of Earth's climate.

On a more personal note, I would like to thank all my friends and family who supported me throughout my graduate career. In particular I owe a great deal of gratitude to my wife, Jennifer, without whom I would much less organized, productive, happy, and loved.

CHAPTER 1

Density Functional Theory Predictions of Equilibrium Isotope Fractionation of Iron due to Redox Changes and Organic Complexation

Abstract:

Molecular orbital/density functional theory (MO/DFT) calculations of Fe^{3+} and Fe^{2+} bonded to H_2O, oxalate, and catecholate were run to predict equilibrium Fe isotope fractionation factors. These predictions were used to compare fractionations associated with changes to the binding environment of Fe and those associated with changes to the oxidation state of Fe. Fractionation factors were calculated from MO/DFT predictions of vibrational frequencies whose accuracy was tested via comparisons to previously measured IR and Raman spectra. The predicted fractionation factors associated with equilibrium between Fe-organic and Fe-H_2O species were < 1.7‰ in vacuo and < 1.2‰ in solution. These fractionation factors were significantly smaller than those predicted for equilibrium between different oxidation states of Fe, for which $1000\ln\cdot(^{56\text{-}54}\alpha) > 2.8$‰ in vacuo and > 2.2‰ in solution. The predicted $^{56}Fe/^{54}Fe$ ratio was greatest in complexes containing Fe^{3+} and in complexes with shorter Fe-O bond lengths; both of these trends follow previous theoretical results. The fractionations caused by redox and organic ligand complexation can be additive, so that the largest predicted fractionations would involve conformational and redox changes that create fractionations in the same direction. However, the probable biologic pathways will not result in additive fractionations as organic complexation prefers Fe^{3+} over Fe^{2+}, leading to ^{56}Fe enrichement, but also favors

long Fe-O bond lengths, leading to ^{56}Fe depletion. These results imply that the most significant biological fractionations will be associated with processes that change the oxidation state of Fe and that identification of biologically-controlled Fe-isotope fractionation will be difficult when abiotic redox fractionations are present in the system. The models studied here also have important implications for theoretical isotope calculations, because we have discovered that an approximation made when predicting gas-phase fractionation factors breaks down for predictions of fractionation factors in aqueous-phase species.

1.1 Introduction

Fe has been of widespread interest in biogeochemistry due to its key role in protein chemistry, its high elemental abundance, and the use of Fe redox reactions as a source of energy. Recent advances in mass spectrometry have greatly expanded the proposed applications of Fe isotope analysis to studies of surface and subsurface geological processes. Because of the high biological demand for Fe and complex biochemistry of Fe, Beard et al. (1999) suggested that Fe isotopes could be useful as a biomarker. Thus, a suite of laboratory studies have been undertaken that examine Fe isotope fractionations due to biological processing.

When organisms mediate redox changes for metabolic purposes, reported fractionations are typically ~1.3-1.5‰ between substrate and dissolved Fe, with larger δ^{56}Fe values in the oxidized phase (BEARD et al., 1999; BEARD et al., 2003; CROAL et al., 2004; JOHNSON et al., 2005). Equilibrium fractionations smaller than ~1.0‰ have been

reported in biological systems where Fe does not metabolically promote redox change, such as during dissolution (BRANTLEY et al., 2001; BRANTLEY et al., 2004; WIEDERHOLD et al., 2006). In an effort to place these biological fractionations within the context of abiotic reactions that may occur in nature or in the laboratory, additional studies have examined fractionation of Fe isotopes via abiotic pathways. As with biological fractionations, the largest equilibrium fractionation reported is associated with redox change ($\Delta Fe(III)_{aq}$-$Fe(II)_{aq}$ = 3.00 ± 0.23‰ at 22ºC, (WELCH et al., 2003). Smaller, yet significant, fractionations associated with abiotic precipitation (WIESLI et al., 2004) and adsorption (ICOPINI et al., 2004; TEUTSCH et al., 2005) have also been reported. Upon review of these studies (ANBAR, 2004; BEARD and JOHNSON, 2004; DAUPHAS and ROUXEL, 2006; JOHNSON et al., 2004), it becomes clear that the main driver of equilibrium Fe isotope fractionation in nature is redox reactions, regardless of whether or not biota are involved (an important caveat must be made here for kinetic fractionations greater than 10‰ that have been reported during complexation of Fe with organic ligands (MATTHEWS et al., 2004) and during anion column chemistry (ANBAR et al., 2000)). Consistent with this analysis is the proposed use of Fe isotopes to interpret the redox state of the early Earth (BEARD et al., 2003; ROUXEL et al., 2005; YAMAGUCHI et al., 2005), as global redox change would alter the reactions available to fractionate Fe isotopes.

Despite the growth of experimental studies, first-principles research into the reactions responsible for observed fractionations has been limited to studies of inorganic systems. Pioneering work by Polyakov and Mineev (POLYAKOV, 1997; POLYAKOV and MINEEV, 1999; POLYAKOV and MINEEV, 2000) predicted the fractionation factors for equilibrium between various mineral phases using data from Mössbauer spectroscopy.

This work on mineral phases was followed by predictions of equilibrium fractionations between various soluble complexes by Schauble et al. (2001) using experimental frequencies and the MUBUFF force field. The most recent work in predicting Fe isotope fractionation comes from Anbar et al. (2005) and Jarzecki et al. (2004), who predict equilibrium fractionation of Fe between Fe^{3+} and Fe^{2+} in water using MO/DFT. These models predicted Fe-isotope fractionations of 2.5-3‰ when this reaction occurs at 22°C. Welch et al. (2003) report equilibrium fractionation between Fe^{3+} and Fe^{2+} in solution of 3.00 ± 0.23‰, on par with the values predicted in the theoretical study. The MO/DFT study resolved a previous conflict between the experimental data and empirical models that predicted fractionations of 5‰ in this system (SCHAUBLE et al., 2001), a disagreement that the MO/DFT studies found to be the result of experimentally mislabeled vibrational modes used in the MUBFF study. These theoretical predictions of Fe isotope fractionations have been useful in interpreting the results of many of the abiotic experiments cited above.

Currently, we know of no theoretical predictions of Fe isotope fractionation upon complexation with organic ligands. The ability to determine which organic ligands have higher $^{56}Fe/^{54}Fe$ ratios at equilibrium can help the interpretation of experiments by Brantley et al. (BRANTLEY et al., 2001) which claims fractionation during ligand-promoted leaching of hornblende is a function of the Fe affinity of the ligand, and that when leaching occurs in the presence of bacteria, fractionation exists between solution and cell matter. Similar experiments on goethite dissolution measured ligand-promoted leaching to have a fractionation of -1.4‰ (BRANTLEY et al., 2004) and -1.7% (WIEDERHOLD et al., 2006). The magnitude of these fractionations is similar to those of

biological fractionations of -1.3‰ reported during dissimilatory Fe reduction (BEARD and JOHNSON, 1999) and 1.5‰ reported for phototrophic Fe-oxidizing bacteria (CROAL et al., 2004). Although isotopic exchange in the outer layers of Fe oxides has been shown as a reasonable explanation of the fractionation during dissimilatory Fe reduction (CROSBY et al., 2005), equilibrium isotope exchange between various ligands may still be the cause of fractionation during Fe-oxidation. This study expands predictions of equilibrium Fe isotope fractionations to Fe-organic complexes, in order to gain reaction-level knowledge of fractionations occurring in solution during ligand-promoted Fe dissolution and to help place fractionations arising during reactions involving complexation with organic material in the context of equilibrium redox reactions, and vice versa.

1.2 Methods

1.2.1 Complexes Modeled

Fe is often leached from inorganic phases by ligands that can form hexadentate complexes in octahedral coordination around Fe. We examined three complexes with octahedral coordination about a central Fe atom, in both Fe^{3+} and Fe^{2+} oxidation states (Figure 1-1): hexaaquo iron ($Fe^{III}(H_2O)_6^{3+}$ and $Fe^{II}(H_2O)_6^{2+}$), iron trisoxalate ($Fe^{III}(Ox)_3^{3-}$ and $Fe^{II}(Ox)_3^{4-}$), and iron triscatechol ($Fe^{III}(Cat)_3^{3-}$ and $Fe^{II}(Cat)_3^{4-}$).

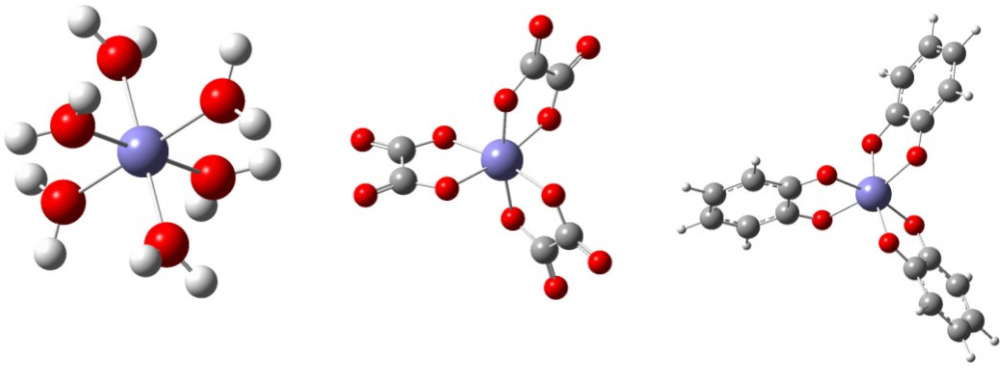

Figure 1-1: Optimized structures of $Fe^{III}(H_2O)_6^{3+}$ (left), $Fe^{III}(Ox)_3^{3-}$ (middle), and $Fe^{III}(Cat)_3^{3-}$ (right), calculated using Gaussian 03 and B3LYP/6-311G(d) basis sets and functionals, and drawn using Gaussview (Gaussian Inc., Wallingford, CT). In this figure, purple atoms represent Fe, grey atoms represent C, red atoms represent O, and white atoms represent H.

1.2.2 Modeling Methodology

Fractionation factors were calculated through a five-step process:

(1) energy minimize the structure for each complex;

(2) calculate the vibrational frequencies for each vibrational mode in the complex and scale the frequencies to account for systematic errors in MO/DFT predictions (HEHRE et al., 1985);

(3) compare the predicted vibrational frequencies to observed vibrational frequencies to ensure model accuracy;

(4) if the model frequencies are sufficiently accurate, re-calculate the vibrational frequencies for each of the stable isotopes of Fe (^{54}Fe, ^{56}Fe, and ^{57}Fe) using the geometries from (1) and the force constants from (2); and

(5) calculate the reduced partition function values for each complex from the model frequencies, and calculate the fractionation factor for equilibrium between any two complexes using the partition function values for the two complexes in question.

Classical mechanical energy minimizations were carried out with the Cerius^2 software package (ACCELRYS, 2003) in order to obtain initial structures for the quantum mechanical energy minimizations. The molecules were modeled using the Universal Force Field 1.02, (UFF, RAPPE et al., 1992). This force field has no Fe^{3+} atom type, so models were constructed using charge equilibration (RAPPE and GODDARD, 1991) to attribute a +3 charge to a Fe^{2+} atom type. Vibrational frequencies were calculated using this methodology but were shown to be insufficiently accurate to predict fractionation factors (Section 2.3).

MO/DFT was chosen for this study because of its relative accuracy and moderate computational costs (HEHRE et al., 1985), and because previous studies have used MO/DFT to accurately model similar complexes. Anbar et al. (2005) used MO/DFT methods to accurately predict inorganic Fe isotope fractionations, and Ohstrom and Michaud-Soret (1999) used MO/DFT to predict isotopic frequency shifts in the νFe-O modes of Fe^{3+}-catecholate and Fe^{3+}-oxalate, but not Fe^{2+} or solvated complexes. Thus, except where otherwise noted, the Gaussian 03 software package (FRISCH et al., 2004) was used to apply MO/DFT methods to the complexes considered here.

MO/DFT methods calculate the electron correlation based on functionals of the electron density. This study utilized B3LYP, which consists of Becke's 3-parameter hybrid of the gradient-corrected and Hartree-Fock exchanges (BECKE, 1997), combined with Lee-Yang Parr correlation functionals (LEE et al., 1988). The basis set used to

describe the electron density was the all-electron 6-311G(d) basis set (KRISHNAN et al., 1980; MCLEAN and CHANDLER, 1980). Hydration effects were modeled implicitly using the Integrated Equation Formalism Polarized Continuum Model (IEFPCM, CANCES et al., 1997).

1.2.3 Vibrational Frequency Predictions

Vibrational frequencies were calculated at energy-minimized structures. If negative vibrational frequencies were reported, the geometry was re-optimized and frequencies recalculated. This process was repeated until all predicted vibrational frequencies were positive. Once a set of positive frequencies were found for a complex, the frequencies were scaled to account for systematic errors resulting from anharmonic effects, which were not considered explicitly in these calculations. In this study, a scaling factor of 0.956 was used; this number was derived in previous a previous study of Fe-organic complexes (EDWARDS et al., 2005). The force constants calculated for each complex were saved and used to recalculate vibrational frequencies after isotopic substitution of the central Fe atom.

Comparing these predicted frequencies to observed frequencies allows for analysis of the accuracy of a particular modeling method. Accurately predicting vibrational frequencies is of particular importance in predicting fractionation factors due to the quadratic dependence of $1000 \cdot \ln(\beta)$ on changes in vibrational frequencies upon isotopic substitution. If the models were a perfect representation of real-world chemistry and there were no errors in experimental determination of vibrational frequencies, then a

plot of calculated frequencies versus observed frequencies would have data points that fall on the line y = x, where y represents the predicted frequencies and x represents the measured frequencies. If we assume deviations from this relationship represent errors in predictions of vibrational frequencies, the errors in our model frequencies can be quantified. Plots of model vs. experimental frequencies are shown in Figure 1-2 for molecular modeling calculations (2a), MO/DFT calculations in vacuo (2b), and MO/DFT calculations in solution (2c). The slope (m), y-intercept, and correlation coefficient (r^2) of the best-fit lines for each model, along with the standard deviations (σ) of each model from the line y = x are shown in Table 1-1.

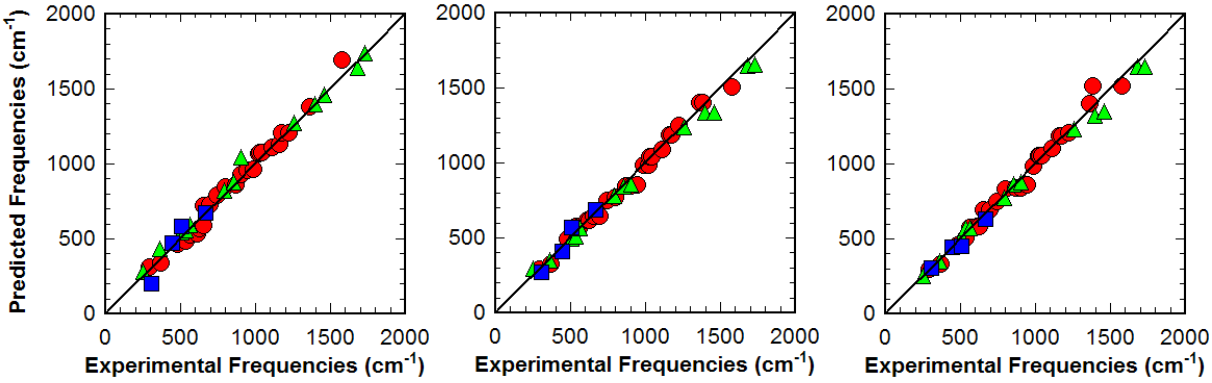

Figure 1-2: Predicted frequencies from (a) UFF, (b) MO/DFT, and (c) MO/DFT/IEFPCM models plotted versus observed frequencies. Red circles represent predictions for $Fe^{III}(Cat)_3^{3-}$, green triangles represent predictions for $Fe^{III}(Ox)_3^{3-}$, and blue squares represent predictions for $Fe^{III}(H_2O)_6^{3+}$. The solid black line is the line y=x, which represents any model that is a perfect simulation of reality. UFF predictions were made using the Cerius[2] software suite (ACCELRYS, 2003), and MO/DFT predictions were made using the Gaussian 03 software suite (FRISCH et al., 2004). Experimental frequencies for $Fe^{III}(Ox)_3^{3-}$ are from direct studies of the complex in solution (JABER et al., 1980), experimental frequencies for $Fe^{III}(Cat)_3^{3-}$ are from a precipitated semiquinone-iron complex (BARRETO et al., 2005), and experimental frequencies for $Fe^{III}(H_2O)_6^{3+}$ are from two studies of CsFe alums (BEST et al., 1980; BEST et al., 1984).

The model frequencies for $Fe^{III}(H_2O)_6^{3+}$ were compared to the same set of frequencies that previous studies (ANBAR et al., 2005; JARZECKI et al., 2004; SCHAUBLE et al., 2001) used for benchmarking, originally taken from IR measurements of Cs β alums (BEST et al., 1980) and Raman measurements of $CsFe(SO_4)_2$ (BEST et al., 1984). The predictions of $Fe^{III}(H_2O)_6^{3+}$ frequencies are the least accurate of all complexes modeled in this study. Possible causes of these large discrepancies include: (1) the possibility that the different net charge in this complex (+3 instead of -3) causes greater model inaccuracies and (2) complications in the experimental assignments of Fe-O modes arising from the necessity to use Ce alums to analyze an otherwise insoluble complex in solution. Of the different methods used, the MO/DFT calculations in vacuo handled this complex the best, with a smaller y-intercept, slope close to unity, and low average error. Despite having similar average errors, the IEFPCM frequencies are preferred to the UFF frequencies because the errors in the UFF predictions exhibited large systematic positive errors that will maximize the impact these errors have on $1000 \cdot \ln(\beta)$ values.

Table 1-1: Descriptions of the best-fit lines for the data points plotted in Figure 1-2, where m and b respectively represent the slope and y-intercept for the best fit line for a particular complex and level of theory. r^2 values indicate the root mean squared deviation of the data from the best-fit line, and σ values represent the standard deviation between the predicted and experimental frequencies.

Complex	Model	*m*	*b*	r^2	σ	% error
Ox	UFF	0.9594	46.09	0.9944	38.04	3.42
Ox	Vacuum	0.9383	8.91	0.9966	29.13	6.06
Ox	IEFPCM	0.9366	15.76	0.9970	27.29	4.77
Cat	UFF	1.0496	-41.42	0.9860	41.29	4.98
Cat	vacuum	0.9938	-6.85	0.9891	33.72	3.15
Cat	IEFPCM	1.0076	-13.75	0.9884	35.25	3.66
H_2O	UFF	0.7891	219.53	0.8931	49.14	24.76
H_2O	Vacuum	0.9995	-34.27	0.9577	37.78	9.39
H_2O	IEFPCM	0.7211	45.18	0.8579	52.81	18.06
All	UFF	0.9902	51.07	0.9750	59.77	7.91
All	vacuum	0.9679	-0.04	0.9901	37.41	5.06
All	IEFPCM	0.9661	-26.35	0.9789	56.15	6.48

The predictions of vibrational frequencies in Fe-organic complexes were significantly better for all three levels of theory. We compared our vibrational frequencies for the $Fe^{III}(ox)_3^{3-}$ complexes to the IR frequencies reported in Jaber et al. (1980) and the Raman frequencies reported in Sima and Makanova (1997); the frequencies for $Fe^{III}(cat)_3^{3-}$ were compared to IR peaks of a precipitated Fe-semiquinone-catecholate complex (BARRETO et al., 2005). Because of the improvement in UFF and IEFPCM predictions, there is a smaller difference in the absolute errors produced by different methods. UFF was not used to calculate $1000 \cdot \ln(\beta)$ factors due to consistent over-predictions of experimental frequencies. The largest errors in the Fe-organic

predictions from all models are attributable to modes internal to the bound ligands. These modes are not strongly affected by isotopic substitution of the Fe atom, and are therefore less important when calculating fractionation factors.

The relatively smaller errors in our predictions of $Fe^{III}(Ox)_3^{3-}$ and $Fe^{III}(Cat)_3^{3-}$ compared to $Fe^{III}(H_2O)_6^{3+}$ frequencies give confidence in the former models, as similar methods to those employed here accurately predicted $1000 \cdot \ln(\alpha)$ for equilibrium between $Fe^{III}(H_2O)_6^{3+}$ and $Fe^{II}(H_2O)_6^{2+}$ (ANBAR et al., 2005; JARZECKI et al., 2004). Because our frequency predictions of the Fe-organic complexes are more accurate than those for complexes already modeled accurately using MO/DFT, we concluded the use of MO/DFT frequencies and force constants to calculate $1000 \cdot \ln(\beta)$ factors was warranted. This is also supported by the relatively low, well distributed errors with which the MO/DFT models predicted the vibrational frequencies of both complexes when compared to the size and distribution of errors from the UFF models.

1.2.4 Calculating 1000•ln(β) From Vibrational Frequency Predictions

The scaled frequencies from the MO/DFT calculations were used to predict equilibrium fractionation factors between $Fe(ox)_3$, $Fe(cat)_3$, and $Fe(H_2O)_6$ in vacuum and in aqueous solution and for both redox states of Fe. First, the $1000 \cdot \ln(\beta)$ values for these complexes were calculated. β represents the equilibrium constant for isotopic exchange in a molecule within a reservoir of the isotopically active element. For example, ${}^{a\text{-}b}\beta(XY)$ represents the equilibrium constant for isotopic exchange of isotopes *a* and *b* of X within XY, when XY is free to exchange isotopes with a limitless reservoir of X:

$^{b}XY \leftrightarrow {}^{a}XY$, and

$${}^{a\text{-}b}\beta = [{}^{a}XY]/[{}^{b}XY].$$

β can also be calculated from the Gibbs' free energy of the isotopic exchange, which in turn is given by the ratio of the reduced partition functions of the molecule for each isotope:

$${}^{a-b}\beta = \left({}^{a}Q_{vib}/{}^{b}Q_{vib}\right) = \prod_{i=1}^{3N-6}\left({}^{a}q_i/{}^{b}q_i\right)\left({}^{a}\nu_i/{}^{b}\nu_i\right),$$

where ${}^{a}Q_{vib}$ is the total vibrational partition function for isotope *a*, *N* is the number of atoms in the molecule, *i* is a label for individual vibrational modes, of which there are a total of *3N-6*, ${}^{a}\nu_i$ is the vibrational frequency for mode *i* and isotope *a*, and ${}^{a}q_i$ is the i^{th} vibrational partition function. Rotational partition functions can be ignored for the species studied here due to symmetry about the isotopically substituted atom. ${}^{a}q_i$ can be calculated from the vibrational frequency of the mode, with the energy defined to be 0 at the bottom of the potential energy well:

$${}^{a}q_{vib} = \frac{e^{-h\nu_i/2kT}}{1-e^{-h\nu_i/kT}},$$

where *h* is Planck's constant, ν_i is the vibrational frequency of mode *i*, *k* is Boltzmann's constant, and *T* is temperature. Because changes in the value of β are small upon isotopic substitution, values are normally reported as $1000\cdot\ln(\beta)$, given by:

$$1000\cdot\ln\left({}^{a-b}\beta\right) = 1000\cdot\left[\ln\left(\prod_{i=1}^{3N-6}\frac{e^{-h^{a}\nu_i/2kT}}{e^{-h^{b}\nu_i/2kT}}\frac{1-e^{-h^{b}\nu_i/kT}}{1-e^{-h^{a}\nu_i/kT}}\right) - \ln\left(\prod_{i=1}^{3N-6}{}^{b}\nu_i/{}^{a}\nu_i\right)\right]. \quad \text{(Eq. 1.1)}$$

Normally, Fe isotope fractionations are measured with respect to changes in $^{56}Fe/^{54}Fe$, so unless explicitly stated the rest of this paper will use *a=56*, *b=54*, and the term $1000 \cdot \ln(\beta)$ as shorthand for $1000 \cdot \ln({}^{56-54}\beta)$.

In previous studies (ANBAR et al., 2005; JARZECKI et al., 2004; WILSON et al., 1980), the second term in Eq. 1.1 was calculated using the ratios of the reduced masses for the complex instead of the ratios of the frequencies, according to the Redlich-Teller product rule (UREY, 1947):

$$\left(\frac{m_a M_b}{m_b M_a}\right)^{3/2}\left(\frac{A_b B_b C_b}{A_a B_a C_a}\right)^{1/2} = \prod_{i=1}^{3N-6} {}^{b}\nu_i / {}^{a}\nu_i ,$$

where m_a is the mass of isotope a and M_a is the mass of the entire molecule when m_a is the mass of the isotopically active atom. Using this approximation to substitute for the second term, the equation used for calculation of $1000 \cdot \ln(\beta)$ can be rewritten as:

$$1000 \cdot \ln\left({}^{a-b}\beta\right) = 1000 \cdot \left[\ln\left(\prod_{i=1}^{3N-6} \frac{e^{-h^a \nu_i / 2kT}}{e^{-h^b \nu_i / 2kT}} \frac{1-e^{-h^b \nu_i / kT}}{1-e^{-h^a \nu_i / kT}} \right) - \ln\left(\frac{m_a M_b}{m_b M_a}^{3/2} \cdot \frac{A_b B_b C_b}{A_a B_a C_a}^{1/2} \right) \right], \quad \text{(Eq. 1.2)}$$

Unfortunately, the Redlich-Teller product rule was not applicable in our IEFPCM models. We can use the following equation to quantify the disagreement:

$$\varepsilon_{R-T} = \left| \left(\frac{m_a M_b}{m_b M_a}\right)^{3/2}\left(\frac{A_b B_b C_b}{A_a B_a C_a}\right)^{1/2} - \prod_{i=1}^{3N-6} {}^{b}\nu_i / {}^{a}\nu_i \right|. \quad \text{(Eq. 1.3)}$$

Table 1-2 displays ε_{R-T} values for each complex modeled. For in vacuo calculations, $\varepsilon_{R-T} < 3 \cdot 10^{-3}$, but for IEFPCM calculations ε_{R-T} were generally > 0.1. There was no correlation between ε_{R-T} and errors in vibrational frequency prediction, so this is not the result of

errors in frequency prediction and the significant $\varepsilon_{R\text{-}T}$ values persisted regardless of starting point geometry, grid size, convergence criteria, and basis set size.

Table 1-2: Model disagreement with the Redlech-Teller product rule, as calculated in Eq. 1.3.

Complex	vacuo $\varepsilon_{R\text{-}T}$	IEFPCM $\varepsilon_{R\text{-}T}$
$Fe^{III}(Ox)_3^{3-}$	$8.84\cdot10^{-4}$	$4.10\cdot10^{-3}$
$Fe^{II}(Ox)_3^{4-}$	$2.11\cdot10^{-3}$	$5.10\cdot10^{1}$
$Fe^{III}(Cat)_3^{3-}$	$2.26\cdot10^{-3}$	$2.40\cdot10^{-1}$
$Fe^{II}(Cat)_3^{4-}$	$2.99\cdot10^{-3}$	$6.02\cdot10^{-1}$
$Fe^{III}(H_2O)_6^{3+}$	$5.33\cdot10^{-5}$	$8.46\cdot10^{-1}$
$Fe^{II}(H_2O)_6^{2+}$	$5.42\cdot10^{-4}$	$5.46\cdot10^{-1}$

If we consider how IEFPCM models differ from in vacuo models, a possible explanation for the large $\varepsilon_{R\text{-}T}$ values in the solvated models presents itself. The Redlich-Teller product equates the ratio of vibrational frequencies to the ratio of the reduced mass of the complex. In doing so, an implicit assumption is made that all the masses affecting the vibrations are explicitly included in the model. When IEFPCM (or any other implicit solvation technique) is employed, this is not the case: solute molecules affect the structure and chemistry of a complex without inclusion of solvent atoms in the model geometry. It appears that the Redlich-Teller product rule is not appropriate for IFEPCM calculations, so we calculated $1000\cdot\ln(\beta)$ values directly from vibrational frequency ratios Eq. 1.1 and recommend that future studies do the same. The 1000·ln(b) values predicted in this study are listed in Table 1-3 and plotted in Figure 1-3 as a function of $10^6/T^2$.

Table 1-3: 1000·ln(β) predictions from B3LYP/6-311G(d) calculations in vacuo and using IEFPCM to model solvation effects. +/- values come from error analysis as described in section 1.3.1.

		in vacuo					
T (K)	**$10^6/T^2$**	**$Fe^{III}(H_2O)_6^{3+}$**	**$Fe^{II}(H_2O)_6^{2+}$**	**$Fe^{III}(Ox)_3^{3-}$**	**$Fe^{II}(Ox)_3^{4-}$**	**$Fe^{III}(Cat)_3^{3-}$**	**$Fe^{II}(Cat)_3^{4-}$**
273.15	13.40	9.9 +0.30/-0.30	6.72 +0.21/-0.21	9.41 +0.30/-0.30	5.24 +0.17/-0.18	8.65 +0.28/-0.28	4.87 +0.16/-0.17
283.15	12.47	9.27 +0.28/-0.28	6.28 +0.20/-0.20	8.79 +0.28/-0.28	4.89 +0.16/-0.16	8.08 +0.26/-0.26	4.55 +0.15/-0.16
293.15	11.64	8.69 +0.27/-0.27	5.89 +0.19/-0.19	8.24 +0.27/-0.27	4.58 +0.15/-0.15	7.56 +0.25/-0.25	4.25 +0.14/-0.15
295.15	11.48	8.58 +0.26/-0.27	5.81 +0.19/-0.19	8.13 +0.26/-0.26	4.52 +0.15/-0.15	7.47 +0.24/-0.25	4.2 +0.14/-0.14
298.15	11.25	8.42 +0.26/-0.26	5.7 +0.18/-0.19	7.98 +0.26/-0.26	4.43 +0.15/-0.15	7.33 +0.24/-0.24	4.11 +0.14/-0.14
303.15	10.88	8.17 +0.25/-0.26	5.52 +0.18/-0.18	7.73 +0.25/-0.25	4.29 +0.14/-0.14	7.1 +0.23/-0.23	3.98 +0.14/-0.14
313.15	10.20	7.69 +0.24/-0.24	5.2 +0.17/-0.17	7.27 +0.24/-0.24	4.03 +0.14/-0.14	6.67 +0.22/-0.22	3.74 +0.13/-0.13
323.15	9.58	7.25 +0.23/-0.23	4.89 +0.16/-0.16	6.85 +0.22/-0.23	3.79 +0.13/-0.13	6.28 +0.21/-0.21	3.52 +0.12/-0.12
333.15	9.01	6.85 +0.22/-0.22	4.62 +0.15/-0.15	6.46 +0.21/-0.21	3.58 +0.12/-0.12	5.93 +0.20/-0.20	3.31 +0.11/-0.11
343.15	8.49	6.48 +0.21/-0.21	4.36 +0.14/-0.15	6.1 +0.20/-0.20	3.38 +0.11/-0.12	5.6 +0.19/-0.19	3.13 +0.11/-0.11

IEFPCM							
T (K)	**$10^6/T^2$**	**$Fe^{III}(H_2O)_6^{3+}$**	**$Fe^{II}(H_2O)_6^{2+}$**	**$Fe^{III}(Ox)_3^{3-}$**	**$Fe^{II}(Ox)_3^{4-}$**	**$Fe^{III}(Cat)_3^{3-}$**	**$Fe^{II}(Cat)_3^{4-}$**
273.15	13.40	10.14 +0.29/-0.30	6.81 +0.21/-0.21	9.08 +0.28/-0.28	6.51 +0.21/-0.21	8.81 +0.27/-0.28	5.92 +0.19/-0.19
283.15	12.47	9.49 +0.28/-0.28	6.36 +0.20/-0.20	8.49 +0.26/-0.26	6.08 +0.19/-0.20	8.23 +0.26/-0.26	5.52 +0.18/-0.18
293.15	11.64	8.9 +0.26/-0.27	5.96 +0.19/-0.19	7.95 +0.25/-0.25	5.69 +0.18/-0.18	7.71 +0.24/-0.24	5.17 +0.17/-0.17
295.15	11.48	8.79 +0.26/-0.27	5.88 +0.18/-0.19	7.85 +0.24/-0.25	5.61 +0.18/-0.18	7.61 +0.24/-0.24	5.1 +0.17/-0.17
298.15	11.25	8.62 +0.26/-0.26	5.77 +0.18/-0.18	7.7 +0.24/-0.24	5.5 +0.18/-0.18	7.46 +0.23/-0.24	5 +0.16/-0.16
303.15	10.88	8.36 +0.25/-0.25	5.59 +0.18/-0.18	7.46 +0.23/-0.23	5.33 +0.17/-0.17	7.23 +0.23/-0.23	4.84 +0.16/-0.16
313.15	10.20	7.87 +0.24/-0.24	5.26 +0.17/-0.17	7.02 +0.22/-0.22	5.01 +0.16/-0.16	6.8 +0.22/-0.22	4.55 +0.15/-0.15
323.15	9.58	7.42 +0.23/-0.23	4.95 +0.16/-0.16	6.61 +0.21/-0.21	4.71 +0.15/-0.15	6.4 +0.20/-0.21	4.28 +0.14/-0.14
333.15	9.01	7.01 +0.21/-0.22	4.67 +0.15/-0.15	6.23 +0.20/-0.20	4.44 +0.14/-0.15	6.04 +0.19/-0.19	4.03 +0.13/-0.13
343.15	8.49	6.63 +0.20/-0.21	4.41 +0.14/-0.14	5.89 +0.19/-0.19	4.19 +0.14/-0.14	5.7 +0.18/-0.18	3.8 +0.13/-0.13
353.15	8.02	6.27 +0.19/-0.20	4.17 +0.13/-0.14	5.58 +0.18/-0.18	3.97 +0.13/-0.13	5.4 +0.17/-0.18	3.6 +0.12/-0.12

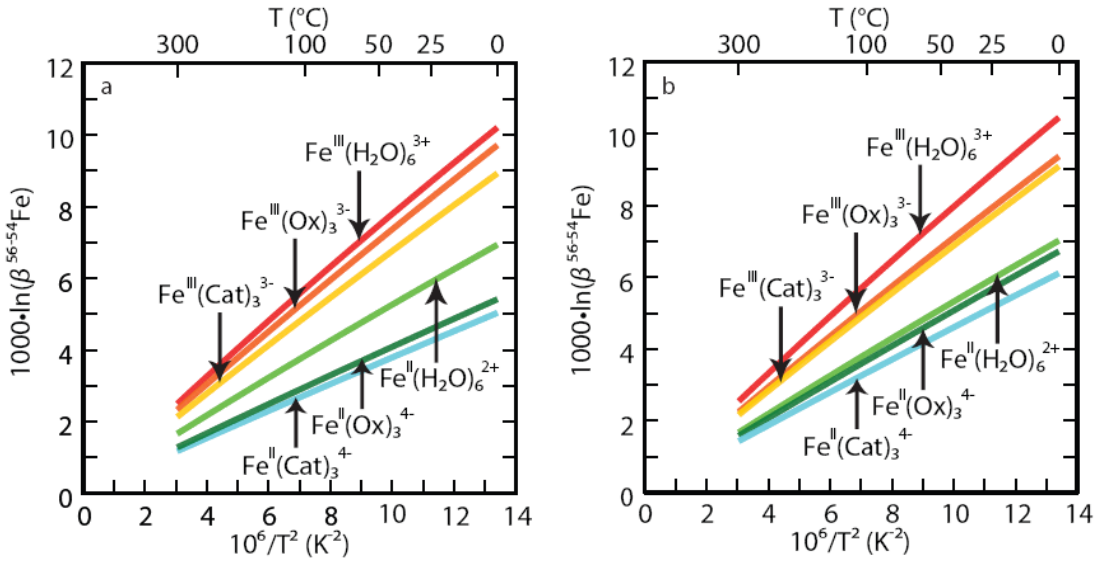

Figure 1-3: 1000·ln(β) vs.$10^6/T^2$ (bottom x-axis) and T (top x-axis) for models in vacuo (a) and using IEFPCM (b). Temperature increases toward the left of the graph, and predicted $^{56}Fe/^{54}Fe$ increases toward the top of the graph. Note the behavior at high temperature (the left side of the graph): all predicted fractionations approach zero in accordance with theoretical expectations. Also note the grouping of the models based on the oxidation state of the Fe – this is responsible for the large fractionations associated with redox change.

1.3 Errors in 1000•ln(β) Predictions

1.3.1 Uncertainties from Vibrational Frequency Errors

The importance of accurate vibrational frequency prediction is highlighted by inaccuracies in MUBFF predictions (SCHAUBLE et al., 2001) shown by Anbar et al. (2005) to be primarily the result of mislabeled vibrational modes from the experimental literature. Here, we quantify the errors in our predictions of fractionation factors resulting

from errors in vibrational frequency predictions. Given that the measurements of Fe-H_2O frequencies have been called into question (ANBAR et al., 2005) and given the previously demonstrated accuracy of fractionation factor predictions for equilibrium between $Fe^{3+}(H_2O)_6$ and $Fe^{2+}(H_2O)_6$ (ANBAR et al., 2005), we will calculate inaccuracies based on the ability of the models to predict frequencies in Fe-organic compounds. We discuss the accuracy of vibrational frequency predictions for $Fe(Ox)_3^{3-}$ and $Fe(Cat)_3^{3-}$ above, and report predictions of Fe bound to the siderophore desferrioxamine B in Chapter 2.

On average, the predicted frequencies for Fe-organic complexes contained 3.65% error for our in vacuo models and 3.50% error for our solvated models. In order to place a limit on the $1000 \cdot \ln(\beta)$ values possible given these uncertainties, we recalculated $1000 \cdot \ln(\beta)$ from (Eq. 1.1) after increasing each frequency by 3.65% for in vacuo calculations and by 3.50% for IEFPCM calculations. Likewise, the lower limits were found by recalculating $1000 \cdot \ln(\beta)$ after decreasing each frequency by 3.65% for in vacuo calculations and by 3.50% for IEFPCM calculations.

There is an assumption made during this error analysis that errors are systematic and that all frequencies were either overestimated or underestimated. Internal testing showed a random distribution of frequency prediction errors would lead to smaller uncertainties in $1000 \cdot \ln(\beta)$. Given the relatively even distribution of errors in our MO/DFT models, this assumption of systematic error in the calculated frequencies likely overestimates the uncertainties in calculated $1000 \cdot \ln(\beta)$, so the error estimates reported here should be considered upper limits to the uncertainties resulting from inaccurate vibrational frequency predictions.

The largest error for in vacuo calculations of $1000 \cdot \ln(\beta)$ was +0.30/-0.30 for $Fe^{III}(H_2O)_6^{3+}$ at 273.15 K, and the largest error for IEFPCM calculations was +0.29/-0.30 for $Fe^{III}(H_2O)_6^{3+}$ at 273.15 K. Uncertainties resulting from inaccurate frequency predictions are the largest source of error considered here, so we use these errors when reporting uncertainty ranges in $1000 \cdot \ln(\beta)$ and propagated them to calculate uncertainty ranges in $1000 \cdot \ln(\alpha)$.

1.3.2 Temperature Dependence of the Dielectric Constant

The values of ν were predicted in each molecule for each isotope of Fe at 273.15 K. For the gas-phase models, structures and frequencies were not dependent on temperature, so the frequencies calculated at 273.15 K were used to calculate $1000 \cdot \ln(\beta)$ over a wide range of temperatures. Because the dielectric constant of water has an influence on geometries and vibrational frequencies and is a function of temperature, we re-ran the IEFPCM model for $Fe^{III}(H_2O)_6^{3+}$ at 323.15 K ($\varepsilon = 69.88$) and at 373.15 K ($\varepsilon = 55.51$), in order to estimate the effect changes in the dielectric constant has on the fractionation factors. Because the dielectric constant of a solvent can affect the structure of a solute, the entire calculation – including geometry optimization – was repeated. Our results show that the effects of the change in the dielectric constant of water are small for temperatures between 273.15 and 373.15 K (Table 1-4). The errors caused by assumption of a constant dielectric constant over this temperature range were smaller than 0.17‰. This represents a maximum error in predictions of fractionation factors, as use of a constant dielectric constant led to underestimations of $1000 \cdot \ln(\beta)$ for both $Fe^{III}(H_2O)_6^{3+}$

and $Fe^{II}(H_2O)_6^{2+}$ at higher temperatures, so that calculations of $1000 \cdot \ln(\alpha)$ will lead to some degree of cancellation of this systematic error, and the discrepancies in $1000 \cdot \ln(a)$ predictions varied by 0.06‰ at 323.15 K and by 0.01% at 373.15 K. At higher temperatures the size of this effect relative to the size of fractionations may become more pronounced, so care should be taken to account for the temperature dependence of the dielectric constant of water in studies for which higher temperature-pressure conditions are relevant (e.g. analysis of fractionations caused during hydrothermal reactions). In this paper, which is primarily concerned with reactions relevant to low-T geochemistry, the effects of a changing dielectric constant are ignored when calculating $1000 \cdot \ln(\beta)$ and $1000 \cdot \ln(\alpha)$.

Table 1-4: 1000·ln(β) for $Fe^{III}(H_2O)_6^{3+}$ and $Fe^{II}(H_2O)_6^{2+}$, calculated using different methodologies. Our standard calculations, listed in the 2nd column, were made in vacuo using B3LYP/6-311G(d) and the Gaussian 03 default settings. Other column labels are as follows: "MUBFF" represents empirical calculations published by Schauble et al. (2001); "B3LYP/6-31G(d)" represents the previous MO/DFT predictions from Anbar et al. (2005) and Jarzecki et al. (2004); ε = X represents calculations in water using an implicit solvation method and a dielectric constant of X, with values of 78.39, 69,88, and 55.51 consistent with temperatures of 273.15K, 323.15K, and 373.15K, respectively; "Guess" represents calculations made with a different starting point geometry; and ultrafine represents calculations done with Gaussian03's "ultrafine" quadrature grid and "verytight" optimization criteria.

	$Fe^{III}(H_2O)_6^{3+}$ 1000·ln(β)							
T (K)	**B3LYP/6-311G(d)**	**MUBFF**	**B3LYP/6-31G(d)**	**ε = 78.39**	**ε = 69.88**	**ε = 55.51**	**Guess**	**Ultrafine**
273.15	9.90	13.6	11.09	10.14	10.31	10.26	9.83	9.87
283.15	9.27		10.39	9.49	9.65	9.60	9.20	9.24
293.15	8.69		9.75	8.90	9.05	9.01	8.63	8.67
295.15	8.58		9.45	8.79	8.94	8.90	8.53	8.56
298.15	8.42	11.6	9.17	8.62	8.78	8.73	8.37	8.40
303.15	8.17		8.64	8.36	8.51	8.47	8.11	8.15
313.15	7.69		8.15	7.87	8.01	7.97	7.64	7.67
323.15	7.25		7.70	7.42	7.56	7.52	7.20	7.23
333.15	6.85		7.29	7.01	7.14	7.10	6.81	6.83
343.15	6.48		6.91	6.63	6.75	6.72	6.44	6.46
353.15	6.14		6.56	6.27	6.39	6.36	6.10	6.12
363.15	5.82		6.23	5.95	6.07	6.03	5.79	5.81
373.15	5.53	7.6	3.97	5.65	5.76	5.73	5.50	5.52
473.15	3.51	5.9	2.75	3.58	3.66	3.64	3.49	3.50
573.15	2.42	4.1		2.47	2.52	2.51	2.40	2.41

	$Fe^{III}(H_2O)_6^{2+}$ 1000·ln(β)							
T (K)	**B3LYP/6-311G(d)**	**MUBFF**	**B3LYP/6-31G(d)**	**ε = 78.39**	**ε = 69.88**	**ε = 55.51**	**Guess**	**Ultrafine**
273.15	6.72	7.2	7.71	6.81	6.92	6.94	6.67	6.70
283.15	6.28		7.21	6.36	6.46	6.48	6.24	6.26
293.15	5.89		6.76	5.96	6.05	6.07	5.84	5.86
295.15	5.81		6.68	5.88	5.97	5.99	5.77	5.79
298.15	5.70	6.2	6.55	5.77	5.86	5.88	5.66	5.68
303.15	5.52		6.36	5.59	5.68	5.70	5.49	5.50
313.15	5.20		5.98	5.26	5.34	5.36	5.16	5.17
323.15	4.89		5.64	4.95	5.03	5.04	4.86	4.87
333.15	4.62		5.33	4.67	4.74	4.76	4.59	4.60
343.15	4.36		5.04	4.41	4.48	4.49	4.33	4.35
353.15	4.13		4.78	4.17	4.24	4.25	4.10	4.11
363.15	3.92		4.54	3.96	4.02	4.03	3.89	3.90
373.15	3.72	4.0	4.31	3.75	3.81	3.82	3.69	3.70
473.15	2.35	2.5	2.76	2.36	2.40	2.41	2.33	2.34
573.15	1.61	1.7	1.93	1.62	1.65	1.65	1.60	1.60

	$Fe^{III}(H_2O)_6^{3+}$- $Fe^{II}(H_2O)_6^{2+}$ 1000·ln(α)								
T (K)	**B3LYP/6-311G(d)**	**MUBFF**	**B3LYP/6-31G(d)**	**ε = 78.39**	**ε = 69.88**	**ε = 55.51**	**Guess**	**Ultrafine**	**Experimental**
273.15	3.18	6.4	3.38	3.33	3.39	3.32	3.16	3.17	3.57
283.15	2.98		3.18	3.13	3.19	3.12	2.96	2.97	
293.15	2.81		2.99	2.94	3.00	2.94	2.79	2.80	
295.15	2.77		2.95	2.91	2.97	2.90	2.76	2.77	3.00
298.15	2.72	5.4	2.90	2.85	2.92	2.85	2.71	2.72	
303.15	2.64		2.81	2.77	2.83	2.77	2.63	2.64	
313.15	2.50		2.65	2.61	2.67	2.61	2.48	2.49	
323.15	2.36		2.51	2.47	2.53	2.47	2.35	2.35	
333.15	2.23		2.37	2.34	2.39	2.34	2.22	2.23	
343.15	2.12		2.24	2.21	2.27	2.22	2.10	2.11	
353.15	2.01		2.13	2.10	2.16	2.11	2.00	2.00	
363.15	1.91		2.02	2.00	2.05	2.00	1.90	1.90	
373.15	1.82	3.6	1.92	1.90	1.95	1.91	1.81	1.81	
473.15	1.17	3.4	1.21	1.22	1.26	1.23	1.16	1.16	
573.15	0.81	2.4	0.82	0.84	0.87	0.85	0.80	0.81	

1.3.3 Uncertainties from Model Imprecision

Our results were also tested for sensitivity to the starting geometry and grid size. We ran UB3LYP/6-311G(d) calculations for $Fe^{3+}(H_2O)_6$ using a variety of initial structures. The resulting $1000 \cdot \ln(\beta)$ values were constant to within 0.07‰. Another way to test for the effects of different starting point geometries is to use more restrictive convergence criteria and a finer grid, thereby increasing the precision and accuracy of model predictions. When calculations were run with the "ultrafine" grid and "very tight" convergence options in Gaussian 03, the predicted $1000 \cdot \ln(\beta)$ was 0.03‰ lower than the one reported here. Thus, although errors associated with starting point geometry selection, grid size, and convergence criteria are present, they are all significantly smaller than those discussed in the preceding sections.

1.4 Results

1.4.1 1000•ln(α) Predictions

$1000 \cdot \ln(\alpha)$ was calculated by taking the difference of $1000 \cdot \ln(\beta)$ for each species in a reaction. For example, for isotopic equilibrium of X between XY and XZ, we have:

$$1000 \cdot \ln\left[{}^{a-b}\alpha(XY - XZ)\right] = 1000 \cdot \ln\left[{}^{a-b}\beta(XY)\right] - 1000 \cdot \ln\left[{}^{a-b}\beta(XZ)\right] \quad (4)$$

Note by these definitions, greater β values indicate stronger partitioning of the heavy isotope in a particular reservoir. Thus, positive values for α indicate preferential

incorporation of the heavy isotope into XY versus XZ. Negative values imply preferential incorporation of the heavy isotope into species XZ. We define all our relationships such that $1000 \cdot \ln(\alpha)$ will always be positive – in other words the complex with the higher $1000 \cdot \ln(\beta)$ factor will always appear first. We also use $1000 \cdot \ln(\alpha)$ to represent $1000 \cdot \ln({}^{56-54}\alpha)$ unless otherwise stated. In the species studied here, $1000 \cdot \ln(\alpha)$ values are an approximation of fractionation factors between species (SCHAUBLE, 2004; UREY, 1947). $1000 \cdot \ln(\alpha)$ values are listed in Table 1-5, and $1000 \cdot \ln(\alpha)$ for pure redox and pure ligand exchange reactions are plotted as a function of $10^6/T^2$ in Figure 1-4.

Table 1-5: Predicted $1000 \cdot \ln(\alpha)$ factors at 298.15 K for all equilibrium reactions studied. Values were calculated by subtracting the $1000 \cdot \ln(\beta)$ of the row from the $1000 \cdot \ln(\beta)$ of the column. Thus, a positive value indicates the complex above the number is predicted to have a higher $^{56}Fe/^{54}Fe$ ratio than the complex to the left of the number. +/- values indicate the square root of the sum of the squares of the errors in $1000 \cdot \ln(\beta)$ predictions for the two complexes in the reaction, calculated as described in Section 1.3.1.

in vacuo	$Fe^{II}(Cat)_3^{4-}$	$Fe^{II}(Ox)_3^{4-}$	$Fe^{II}(H_2O)_6^{2+}$	$Fe^{III}(Cat)_3^{3-}$	$Fe^{III}(Ox)_3^{3-}$	$Fe^{III}(H_2O)_6^{3+}$
$Fe^{II}(Cat)_3^{4-}$	-	0.32 +0.20/-	1.59 +0.23/-	3.21 +0.28/-	3.86 +0.29/-	4.31 +0.23/-0.23
$Fe^{II}(Ox)_3^{4-}$		-	1.27 +0.24/-	2.89 +0.28/-	3.55 +0.30/-	3.99 +0.30/-0.30
$Fe^{II}(H_2O)_6^{2+}$			-	1.62 +0.30/-	2.28 +0.32/-	2.72 +0.32/-0.32
$Fe^{III}(Cat)_3^{3-}$				-	0.65 +0.35/-	1.1 +0.35/-0.36
$Fe^{III}(Ox)_3^{3-}$					-	0.45 +0.37/-0.37

IEFPCM	$Fe^{II}(Cat)_3^{4-}$	$Fe^{II}(Ox)_3^{4-}$	$Fe^{II}(H_2O)_6^{2+}$	$Fe^{III}(Cat)_3^{3-}$	$Fe^{III}(Ox)_3^{3-}$	$Fe^{III}(H_2O)_6^{3+}$
$Fe^{II}(Cat)_3^{4-}$	-	0.50 +0.24/-	0.77 +0.24/-	2.46 +0.29/-	2.70 +0.29/-	3.62 +0.24/-0.24
$Fe^{II}(Ox)_3^{4-}$		-	0.27 +0.25/-	1.96 +0.29/-	2.20 +0.30/-	3.12 +0.31/-0.32
$Fe^{II}(H_2O)_6^{2+}$			-	1.69 +0.30/-	1.93 +0.30/-	2.85 +0.31/-0.32
$Fe^{III}(Cat)_3^{3-}$				-	0.24 +0.33/-	1.16 +0.35/-0.35
$Fe^{III}(Ox)_3^{3-}$					-	0.92 +0.35/-0.36

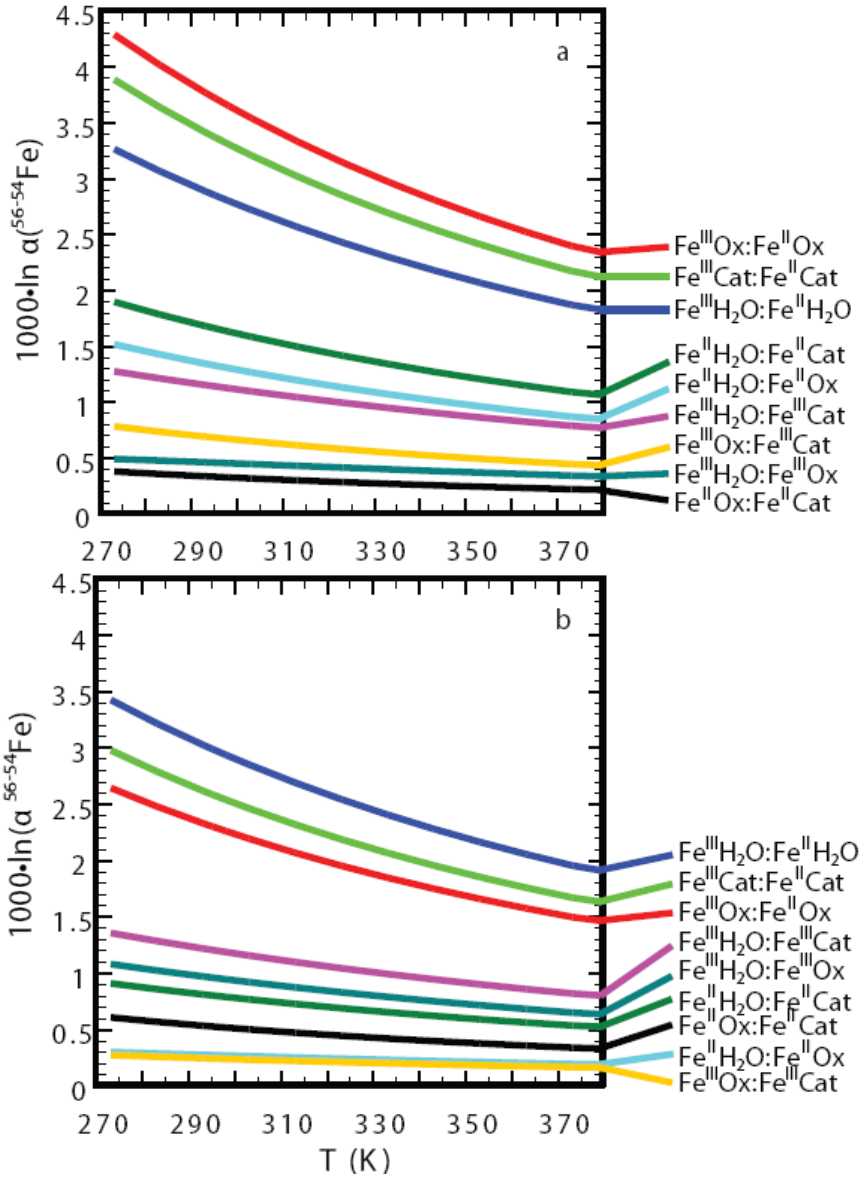

Figure 1-4: 1000·ln(α) vs. T for (a) MO/DFT in vacuo calculations and (b) MO/DFT IEFPCM calculations. Note the partitioning of fractionations into two groups: the greatest fractionations are predicted for changes in the oxidation state of Fe, and the smallest fractionations are predicted for changes in the bonding environment of Fe. This is the case for both sets of calculations, and illustrates the importance of redox reactions to fractionation of Fe isotopes.

1.4.2 Comparison of Results to Previous Studies

Although the in vacuo predictions of $1000 \cdot \ln(\alpha)$ for equilibrium between $Fe^{III}(H_2O)_6^{3+}$ and $Fe^{II}(H_2O)_6^{2+}$ compare reasonably well to the predictions reported in Anbar et al. (2005), the in vacuo predictions of $1000 \cdot \ln(\beta)$ show significant disagreement (Table 1-4). For example, our in vacuo prediction for $1000 \cdot \ln(\beta)$ of $Fe^{III}(H_2O)_6^{3+}$ at 273.15 K is 9.90, 1.19 less than the Anbar et al. (2005) prediction (11.09). This difference is greater than all uncertainties considered in section 3. There are three potential sources of the disagreement:

(1) the use of scaled frequencies in this study and unscaled frequencies in Anbar et al. (2005);

(2) the effects of different basis sets and symmetry constraints on geometry; and

(3) the effects of basis set size on calculations of vibrational frequencies at a given geometry.

Most of the discrepancy between the two models arises from the first effect, as calculations utilizing our unscaled frequencies resulted in a prediction of $1000 \cdot \ln(\beta) = 10.74$. The remaining error is attributed to the different optimized geometries resulting from differences in basis set and symmetry constraints. This was validated by frequency predictions using B3LYP/6-311G(d) at the geometries reported by Anbar et al. The resulting $1000 \cdot \ln(\beta)$ prediction (using unscaled frequencies) was 11.07, within 0.02 of the Anbar et al. prediction. Thus, by using unscaled frequencies at the geometries reported by Anbar et al., we are able to reproduce their results.

Our IEFPCM predictions show larger discrepancies with the PCM predictions from previous calculations (ANBAR et al., 2005; JARZECKI et al., 2004). We believe the main reason for the disagreement is the use of Eq. 1.2 to calculate $1000 \cdot \ln(\beta)$ in the previous study and the use of Eq. 1.1 to calculate $1000 \cdot \ln(\beta)$ in this study. Section 2.4 gives our rationale for choosing Eq. 1.1 for calculations using implicit solvation methods. When we calculated $1000 \cdot \ln(\beta)$ using reduced masses, as in Eq. 1.2, our results match the previous DFT results more closely and the disagreement is similar to that witnessed for in vacuo calculations. The remaining error is explainable by the differences in basis set size and symmetry constraints that caused the disagreement in the in vacuo predictions.

The discrepancies resulting from different basis sets, symmetry constraints, solvation effects, frequency scaling, and partition function equations indicates a need for consistent methodologies, both in predicting vibrational frequencies and in translating them into $1000 \cdot \ln(\beta)$ predictions. The scaled B3LYP/6-311G(d) symmetry-free models employed here should exhibit greater accuracy than the unscaled B3LYP/TZV-6-31G(d) hybrid models due to the larger basis sets used in the former model for O and H atoms, the extra freedom given to atoms during geometry optimization, the inclusion of scale factors to account for errors arising from neglecting anharmonic effects, and the elimination of disagreements with the Redlich-Teller product rule.

Our results compare favorably with experimental values published by Welch et al. (2003). Our predicted $Fe^{III}(H_2O)_6^{3+}/Fe^{II}(H_2O)_6^{2+}$ fractionation factors at 273.15 K are 3.18 in our gas-phase model and 3.33 in our aqueous model. The in vacuo value is just outside of the range of values reported by Welch et al. at 0°C (2003): 3.57 ± 0.38; the

solvated calculation is within the error estimates from the experimental study. Our models also yield accurate results at 295.15 K (22°C), where the predicted fractionation factor is 2.77 for the gas phase model and 2.92 for the aqueous model, in agreement with the value of 3.00 ± 0.23‰ reported by Welch et al.(2003).

1.4.3 1000•ln(β) and Bond Length

The fact that these calculations predict that the hexaaquo complexes favor the heavier isotope over the strong organic ligand complexes appears to contradict the general rule that stronger bonds favor heavy isotopes. However, our results are actually consistent with the expected trend. Figure 1-5 shows $1000 \cdot \ln(\beta)$ values plotted against average Fe-O bond distance. As in previous studies of transition metal fractionation, these two variables are inversely proportional (ANBAR et al., 2005; SCHAUBLE et al., 2001). This follows standard isotope theory: heavy isotopes are known to be partitioned into stronger bonds, which in turn are associated with shorter bond lengths. The surprising result is that the Fe-O bonds in the Fe-trioxalate and Fe-triscatecholate complexes are longer than for the Fe hexaaquo complexes. Lengthening of the bonds is undoubtedly associated with the change from a positively charged hexaaquo complex to the highly negatively charged (-3 or -4) organic complexes.

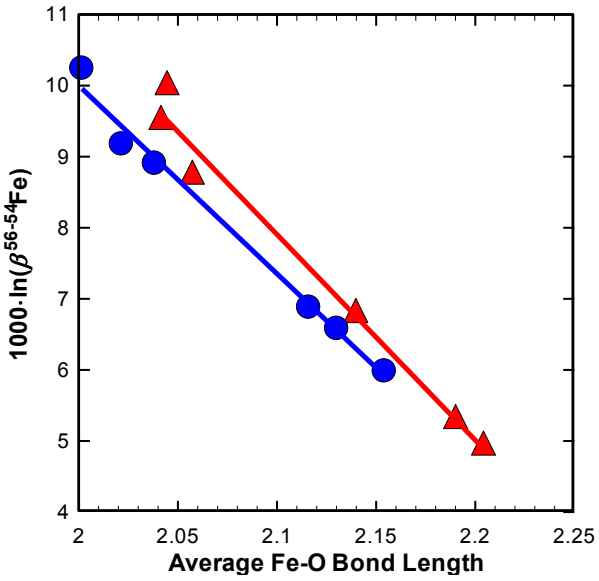

Figure 1-5: 1000·ln(α) vs. average Fe-O bond length (Å) for all complexes studied. Red triangles represent in vacuo calculations, and blue circles represent IEFPCM calculations. This figure displays the same general trends reported in previous studies on metal isotope fractionation (ANBAR et al., 2005; JARZECKI et al., 2004; SCHAUBLE, 2004; SCHAUBLE et al., 2001), as bond length is inversely proportional to 1000·ln(β). This suggests the chemical controls on Fe isotope fractionation will follow controls on Fe-O bond length.

The consistency of this trend in various studies using different methodologies implies that we may be able to qualitatively compare 1000·ln(β) from bond lengths; such comparisons would cut computational costs significantly. The other trend to note in figure 1-5 is the in vacuo calculations are shifted ~0.4-0.7‰ up from the IEFPCM calculations, even for similar molecules using otherwise similar methodology. Apparently, the method employed can shift the 1000·ln(β) predictions for a given bond length, a potential source of error that should be kept in mind when comparing predictions from different publications.

1.5 Discussion

There are two major types of Fe isotope fractionation we are attempting to predict in this study: fractionation associated with changes to the oxidation state of the Fe atom and fractionation associated with changes to the molecules bound to the Fe atom. Figure 1-3 shows a plot of $1000 \cdot \ln(\beta)$ vs, $10^6/T^2$ ($^{56}Fe/^{54}Fe$ ratios increase up the figure). There is a clear separation of $1000 \cdot \ln(\beta)$ between complexes containing Fe^{2+} and those containing Fe^{3+}, implying that fractionations due to redox changes should be relatively large.

There is also a consistent but less pronounced trend in the effects of complexation changes on $^{56}Fe/^{54}Fe$. Specifically, $Fe(H_2O)_6$ has the highest $^{56}Fe/^{54}Fe$, followed in order by $Fe(Ox)_3$ and $Fe(Cat)_3$. $^{56}Fe/^{54}Fe$ appears to decrease with increasing Fe affinity, as the Fe affinities of H_2O, oxalate, and catechol are -2.9 (NIST, 1998), 7.6 (NIST, 1998), and 19, (CRUMBLISS, 1991) respectively. This trend is expressed for both oxidation states of Fe and for models in solution and in vacuo, and follows from the Fe-O bond lengths of the different complexes (Figure 1-5, Section 1.4.3). The relationship between Fe affinity and $^{56}Fe/^{54}Fe$ at equilibrium helps explain experimental data on ligand-promoted leaching of Fe (BRANTLEY et al., 2001) that displays a positive relationship between ligand strength and the fractionation of light Fe isotopes into solution. According to our predictions, the ligands with higher Fe affinities would be expected to have lower $1000 \cdot \ln(\beta)$ values and thus would be more efficient at removing ^{54}Fe from the mineral surface. We should note that the theoretical calculations do not span as much parameter space as the experimental data does and that calculations on larger ligands such as

siderophores should be made to ensure this trend continues for complexes with higher Fe affinities (Chapter 2).

The implications of these models for Fe isotope fractionations are significant. The $1000 \cdot \ln(\alpha)$ values shown in Figure 1-4 and Table 1-5 predict the equilibrium Fe isotope fractionation between the complexes modeled. Again, a clear separation is seen: fractionations involving redox changes are consistently and significantly larger than fractionations that only involve changes to the ligands bound to the central Fe atom. When these two types of fractionation are combined to examine reactions involving both complexation and redox changes one can see that equilibrium Fe isotope fractionations will likely be greatest when Fe is reduced and moved to ligands with lower Fe affinities. The reactions that occur in natural systems do not normally express this pattern. Rather, complexation with organic material usually involves bonds between oxidized Fe and ligands with high Fe affinities because organisms need to increase the apparent solubility of Fe^{3+}. The low oxidation state favors heavy isotopes whereas complexation with strong ligands favors light isotopes. Therefore, the involvement of organic material suppresses the magnitude of fractionations in the system from what they would be for isotopic equilibrium between $Fe^{III}(H_2O)_6^{3+}$ and $Fe^{II}(H_2O)_6^{2+}$.

Consider, for example, fractionations at 298.15 K between $Fe(H_2O)_6$ and $Fe(cat)_3$ in solution (Table 1-5, IEFPCM). The lowest fractionations in the $Fe(H_2O)_6$-$Fe(cat)_3$ system arise when redox changes are absent: the fractionation factor for equilibrium between $Fe^{II}(H_2O)_6^{2+}$ and $Fe^{II}(cat)_3^{4-}$ is 0.77 +0.24/-0.24‰, and the fractionation factor for equilibrium between $Fe^{III}(H_2O)_6^{3+}$ and $Fe^{III}(cat)_3^{3-}$ is 1.16 +0.35/-0.35‰. Fractionations caused solely by redox changes in this system plot much higher:

equilibrium between $Fe^{III}(H_2O)_6^{3+}$ and $Fe^{II}(H_2O)_6^{2+}$ is predicted to produce fractionations of 2.85 +0.31/-0.32‰, and equilibrium between $Fe^{III}(cat)_3^{3-}$ and $Fe^{II}(cat)_3^{4-}$ is predicted to produce fractionations of 2.46 +0.29/-0.29‰.

"Mixed reactions" where both redox and ligand change are occurring can span a wide range of values: The predicted fractionation factor for $Fe^{III}(H_2O)_6^{3+}$ and $Fe^{II}(cat)_3^{4-}$ is 3.62 +0.24/-0.24‰, but a reaction between these two species should be rare in nature because Fe^{2+} is more soluble than Fe^{3+}, and siderophores have higher association constants with Fe^{3+} than Fe^{2+}. The predicted fractionation factor for the more common equilibrium between $Fe^{III}(cat)_3^{3-}$ and $Fe^{II}(H_2O)_6^{2+}$ is 1.69 +0.30/-0.30‰, a value significantly smaller than the pure redox fractionations. Thus, redox reactions should be the primary source of Fe isotope fractionation in the $Fe(H_2O)_6$-$Fe(cat)_3$, changes to the bound ligands should have a secondary effect, and the secondary fractionations most commonly found in nature should be smaller than the redox reactions.

The same patterns are found in the $Fe(H_2O)_6$-$Fe(ox)_3$ system and the $Fe(ox)_3$-$Fe(cat)_3$ system. We conclude that changes in the bonding environment have a second-order influence on Fe-isotopic fractionations compared to those induced by changes in Fe oxidation state. The largest fractionations modeled here resulting from reactions expected to occur in natural systems are those resulting from equilibrium between $Fe^{III}(H_2O)_6^{3+}$ and $Fe^{II}(H_2O)_6^{2+}$. Given the smaller fractionations for redox reactions in Fe-organic compounds, complexation with these ligands is likely to mitigate rather than enhance this observed fractionation.

1.6 Conclusions

The methodology employed here is accurate in predicting the vibrational frequencies of Fe-organic complexes. As a result, the predicted isotopic fractionation factors for equilibrium between the complexes considered here are reasonably accurate when compared to previous model predictions, theoretical expectations, and experimental measurements within ~0.3‰. MO/DFT methods can therefore be used to predict isotopic fractionations of Fe and other transition metals. Care must be taken to avoid inaccurate assumptions such as application of the Redlich-Teller product rule to aqueous models or the use of a T-independent dielectric constant for water at high temperatures and pressures.

The general pattern exhibited by our models is in agreement with the current consensus in the literature: changes in the oxidation state of Fe are more important to Fe isotope fractionation than are changes in the bonding environment of Fe. The main implication of this is that Fe isotopes are most useful as a proxy for processes that change the oxidation state of Fe. This does not preclude biological processes, as there are many organisms that oxidize or reduce Fe for energy or for inclusion of Fe into protein centers. However, there are also a plethora of abiotic processes that can change the oxidation state of Fe, so if Fe isotopes are used as a biomarker care must be taken to include either additional proxies for biological activity or tests designed to rule out inorganic redox reactions.

The recent trend of using Fe isotopes to track global changes in the oxidation state of the surface environment (BEARD and JOHNSON, 2005; ROUXEL et al., 2005;

YAMAGUCHI et al., 2005) is supported by this work, as such changes to the surface environment will bring about changes in the redox chemistry of Fe, thus altering the major pathways for isotopic fractionation. Regardless of whether these redox reactions occur inside or outside of cells, the increased mobility of Fe and potential for delivery to redox gradients greatly increases the potential for isotopic fractionation. Complexation reactions can enhance or diminish these effects, so observations must be interpreted with the significant (if secondary) equilibrium fractionations resulting from complexation in mind. Additionally, equilibrium reactions involving changes to the coordination of Fe bonds and all kinetic reactions have yet to be modeled at the MO/DFT level. Thus, despite the emerging consensus between field, laboratory, and theoretical work, further studies must predict kinetic and coordination effects before strong theoretical conclusions on the utility of Fe isotopes in nature are drawn.

CHAPTER 2

Molecular Modeling of the Fe(III)-Desferrioxamine B Siderophore Complex – Electronic Structure, IR Vibrational Frequencies, and Equilibrium Fe-Isotope Fractionation in Solution

Abstract:

Hybrid molecular orbital/density functional theory (MO/DFT) calculations were used to examine the electronic structure, vibrational frequencies, and equilibrium isotope fractionation factors of Fe-desferrioxamine B (DFO-B) complexes in solution. MO/DFT predicted structure and vibrational frequencies of the Fe(III)-DFO-B complex compared reasonably well with previously published experimental and theoretical results. Solvation effects are minimal on local coordination environments around the Fe(III), but conformational effects on the DFO-B were predicted due competition between inter- and intramolecular H-bonds. Energy minimizations of DFO-B complexes with Fe(III), Fe(II), and Al(III) revealed that the ionic radius ratios can be utilized to predict complexation strengths. Natural Bonding Orbital (NBO) analysis of the complexes indicated that shorter bonds did not necessarily translate into stronger complexation because covalent bonding must be considered. Partition functions predicted that the fractionations associated with the Fe-DFO-B complex were not as large as those for electron exchange between Fe(II) and Fe(III) in water. However, the predicted fractionations were close to the amount reported during siderophore-promoted dissolution of goethite; this is consistent with the idea that Fe is delivered to cells from minerals via Fe-siderophore complexes rather than smaller Fe-organic complexes.

2.1 Introduction

Iron is an essential nutrient for the majority of organisms, functioning in a range of cell reduction and enzymatic processes. Despite the natural abundance of iron (elemental iron comprises approximately 5% of the Earth's crust, making it the fifth most abundant element), availability to plants and microorganisms in most natural environments is limited. Iron limitations primarily arise from the insolubility and slow dissolution rates of Fe(III)-bearing minerals. Microorganisms require Fe concentrations on the order of micromoles, but at circum-neutral pH the steady-state concentration of Fe(III) (aq) is 10^{-18} M with respect to most Fe(III)-bearing minerals (JARZECKI et al., 2004; KISS and FARKAS, 1998). Because of the difference between the biological demand and availability of Fe, the production of bioavailable Fe is often a key step in its cycling in natural systems.

Siderophores, a class of organic acids with large complexation constants for Fe, are produced by several organisms in order to avoid iron deficiency (WIEDERHOLD et al., 2006). Due to their high affinity for Fe, siderophores complex Fe by extracting it from Fe(III)-bearing minerals or aqueous Fe(III) complexes. After complexation, siderophores return Fe to the organism for uptake through a variety of cellular recognition and transport mechanisms (ALBRECHT-GARY and CRUMBLISS, 1998; BOUKHALFA and CRUMBLISS, 2002). Release of Fe within the organism frees the siderophore to scavenge additional Fe. The use of siderophores greatly enhances the ability of organisms to acquire Fe in environments where Fe is a limiting nutrient.

Complexation of Fe(III) by naturally synthesized siderophores is efficient because of the remarkably large association constants of Fe(III)-siderophore complexes. Measured 1:1 association constants for Fe(III)-siderophore complexes range between 10^{23} to 10^{52} (ALBRECHT-GARY and CRUMBLISS, 1998; HERNLEM et al., 1996). Specificity for Fe(III) is achieved because the relative magnitude of siderophore association constants for other di- and tri-valent metals is significantly lower. For example, the stability constants for octahedral coordination of desferrioxamine B (DFO-B) (a natural siderophore synthesized by the soil actinomycete *Streptomyces pilosus*) with various transition metals are as follows: Fe(III) = 42.33, Ga(III) = 38.96, Al(III) 36.11, Ni(II) = 27.66, Cu(II) = 23.98, and Zn(II) = 20.40 (ANDEREGG et al., 1963; EVERS et al., 1989; HERNLEM et al., 1996; KURZAK et al., 1992).

Because much of the Fe acquired by organisms is derived from Fe(III)-bearing minerals, the interactions of siderophores with mineral surfaces are important. Siderophores complex Fe from Fe(III)-bearing minerals by promoting dissolution (proton- and/or ligand-promoted), but the mechanisms are not well understood (WIEDERHOLD et al., 2006). Experimental evidence (CHEAH et al., 2003) has shown that the dissolution of goethite in the presence of both oxalate and DFO-B is faster than if just one of the two ligands is present. (CHEAH et al., 2003) suggested the possibility that oxalate removes Fe from the mineral surface and DFO-B subsequently scavenges Fe in solution from the oxalate complex.

Recent work by Wiederhold et al. (2006) has shown that leaching of Fe(III) from goethite was associated with isotopic fractionation during oxalate-promoted dissolution, but not with proton-promoted dissolution. Wiederhold et al. (2006) reasoned that ligand-

promoted dissolution was initiated when bonds between an Fe atom and its surrounding O atoms were broken. On the other hand, proton-promoted dissolution was suggested to occur when bonds were broken between the surrounding O atoms with other Fe atoms in the mineral lattice. Previous work has also measured the fractionation of Fe isotopes during leaching of Fe from hornblende (BRANTLEY et al., 2001; 2004) in the presence of DFO-B. BRANTLEY et al. (2001) studied a variety of ligands and suggested that the amount of fractionation that occurred during dissolution was related to the Fe affinity of the ligand. In these isotope studies, a major challenge was quantifying the amount of fractionation caused by either equilibrium or kinetic effects.

Unfortunately, the process of separating ligand-bound Fe from Fe in solution can lead to isotopic fractionation (WIEDERHOLD et al., 2006). Thus, validation of these hypotheses would be greatly assisted by the development of models that accurately predict isotope equilibrium constants. As a starting point, methods need to be explored that can predict isotopic fractionation for large organic molecules such as the Fe-siderophore complexes. Fractionation factors have already been published for Fe(II)-$(H_2O)_6$ and Fe(III)-$(H_2O)_6$ (ANBAR et al., 2005; JARZECKI et al., 2004), as well as for Fe(II)-oxalate and Fe(III)-oxalate (Chapter 1). The calculation of fractionation factors for Fe-siderophore complexes should complete our theoretical understanding of equilibrium fractionations occurring in solution during these experiments.

The siderophore examined in this investigation was DFO-B, the most extensively studied siderophore with respect to mineral dissolution of the approximately 500 known siderophore structures (WIEDERHOLD et al., 2006). DFO-B is a linear trihydroxamic acid composed of 1,5-diaminopentane and succinic acid residues. Uncomplexed DFO-B has

four acidic protons (three hydroxamic acids and one terminal amine), is positively charged, and soluble in water and alcohols (BORGIAS et al., 1989). DFO-B coordinates Fe(III) through six oxygen donors forming three chelate rings in distorted octahedral symmetry. In principle, DFO-B is capable of forming a hexadentate complex with Fe(III) resulting in 16 possible geometrical and optical isomers, though they likely have small energy differences (BORGIAS et al., 1989; DHUNGANA et al., 2001; LEONG and RAYMOND, 1975). The complex has a 1:1 stoichiometry with the formula MLH (M=metal, L=ligand, H=proton) where the terminal non-coordinating amino group is protonated.

Previous investigations of hydroxamate complexes at the goethite-water interface have been conducted and proved insightful (HOLMEN and CASEY, 1996; HOLMEN et al., 1997). Holmen and coworkers (HOLMEN and CASEY, 1996; HOLMEN et al., 1997) used acetohydroxamic acid (aHa) as an analog for the high molecular weight hydroxamate siderophores and performed Hartree-Fock calculations to investigate various conformations of aHa. Edwards et al. (2005) used the B3LYP/6-311G(d) method to predict vibrational frequencies of Fe-complexed by aHa. To date, isotope fractionation factors have not been predicted for Fe-DFO-B directly.

The objective of this investigation was to examine the high chemical affinity of DFO-B for Fe(III) and to predict the equilibrium Fe isotope fractionations associated with the Fe-DFO-B complex in solution. First, we examined the effects basis set size had on predictions of Fe-O bond parameters in Fe(III)-DFO-B by comparing energy minimized structures to published single crystal X-ray diffraction data, and considered different methodologies to handle the effects of solvation. After method discrimination, energy-

minimization and NBO (Natural Bond Orbital Analysis, WEINHOLD and LANDIS, 2001) were performed for Fe(II)- , Fe(III)-, and Al(III)-DFO-B to investigate electronic and structural differences between the complexes. Frequency calculations were performed on geometry optimized Fe(III)-DFO-B and Fe(II)-DFO-B and compared to previously published experimental and theoretical results (EDWARDS et al., 2005). The frequency calculations enabled the prediction of the equilibrium isotope constants for Fe(III)-DFO-B and Fe(II)-DFO-B in solution, and the equilibrium constants for isotope exchange of Fe-DFO-B with Fe-$(H_2O)_6$ and Fe-$(oxalate)_3$ were established.

2.2 Computational Methods

Molecular orbital/density functional theory (MO/DFT) calculations were performed with Gaussian 03 (FRISCH et al., 2004). The unrestricted, hybrid MO/DFT method was employed using Becke's 3-parameter nonlocal-exchange functional (BECKE, 1997; STEPHENS et al., 1994) and the gradient-corrected correlation functional of Lee et al. (LEE et al., 1988) (UB3LYP). The UB3LYP method has been shown to accurately predict the molecular structures and vibrational frequencies of transition metal complexes (KOCH and HOLTHAUSEN, 2000). The local bonding environment of Fe(III)-DFO-B as predicted by the MO/DFT calculations was compared to previously published single-crystal X-ray diffraction data (DHUNGANA et al., 2001). Several basis sets were used to evaluate the quality of these local bonding environment predictions: 6-31G (BINNING and CURTISS, 1990; BLAUDEAU et al., 1997; DITCHFIELD et al., 1971; FRANCL et al., 1982; GORDON, 1980; HARIHARAN and POPLE, 1972; HARIHARAN and POPLE, 1973; HEHRE et

al., 1985; RASSOLOV et al., 1998; RASSOLOV et al., 2001), 6-31G(d) (FRISCH et al., 2004), 6-31+G(d) (REED and CLARK, 1988), and 6-311G(d) (HAY and WADT, 1985; KRISHNAN et al., 1980; MCLEAN and CHANDLER, 1980; WACHTERS, 1970), 6-311+G(d) (REED and CLARK, 1988). Energy minimizations were performed without application of symmetry or other geometrical constraints, preventing them from biasing the solution. Frequency calculations were subsequently performed to verify that a minimum was located (i.e., no imaginary frequencies), to obtain predicted IR frequencies comparable to experimental IR spectra collected by Edwards et al. (2005), and to calculate Fe isotope fractionation factors.

Gas phase IR frequencies for Fe(III)-DFO-B were calculated using the UB3LYP/6-311G(d) method. This method has been shown to accurately predict IR frequencies for Fe(III)-triscatechol and Fe(III)-trisoxalate, two complexes with octahedral coordination similar to Fe(III)-DFO-B (Chapter 1). Frequencies were scaled by a factor of 0.956 developed for similar systems (EDWARDS et al., 2005) in order to account for errors associated with the use of a harmonic oscillator approximation (HEHRE et al., 1985). Theoretical spectra were generated in Molden (SCHAFTENAAR and NOORDIK, 2000)) by applying Gaussian peaks with a half-width of 5 cm^{-1} to the scaled frequencies. The predicted frequencies were compared to previously measured vibrational frequencies of Fe(III)-DFO-B in solution (EDWARDS et al., 2005).

The Integral Equation Formalism Polarizable Continuum Model (IEFPCM, CANCES et al., 1997) was used to account for solvation implicitly. Unfortunately, the large size of the siderophore and corresponding complexity of the cavity caused difficulties with energy minimizations. These difficulties were alleviated by using a

smaller basis set (6-31G instead of 6-311G(d)), increasing the minimum value of the spheres to 0.5 Å, and reducing the number of added spheres (i.e., decreasing the overlap index to 0.8). Explicit solvation was also used to model the Fe(III)-DFO-B complex using 72 water molecules. Energy minimization for the explicit solvation model was performed using the UB3LYP exchange-correlation functional, CEP-121G (CUNDARI and STEVENS, 1993; STEVENS et al., 1984; STEVENS et al., 1992) basis set on Fe, and 3-21G(d,p) basis set (BINKLEY et al., 1980; DOBBS and HEHRE, 1986; DOBBS and HEHRE, 1987a; DOBBS and HEHRE, 1987b; GORDON et al., 1982; PIETRO et al., 1982) on all other atoms.

Under circum-neutral pH, Fe(III)-DFO-B has a net +1 charge arising from the terminal amine group. The +1 net charge is balanced by a counter anion. For the gas-phase calculations, the Fe-(III)-DFO-B structure had an overall neutral charge because the terminal amine group was not protonated (i.e., $–NH_2$ instead of $–NH_3^+$). This approach was adopted to avoid ion-dipole intramolecular interactions in the gas-phase. However, for calculations of Fe(III)-DFO-B in solution, the protonated DFO-B structure was modeled because solvation prevented the formation of intramolecular H-bonds (see Figure 2-1).

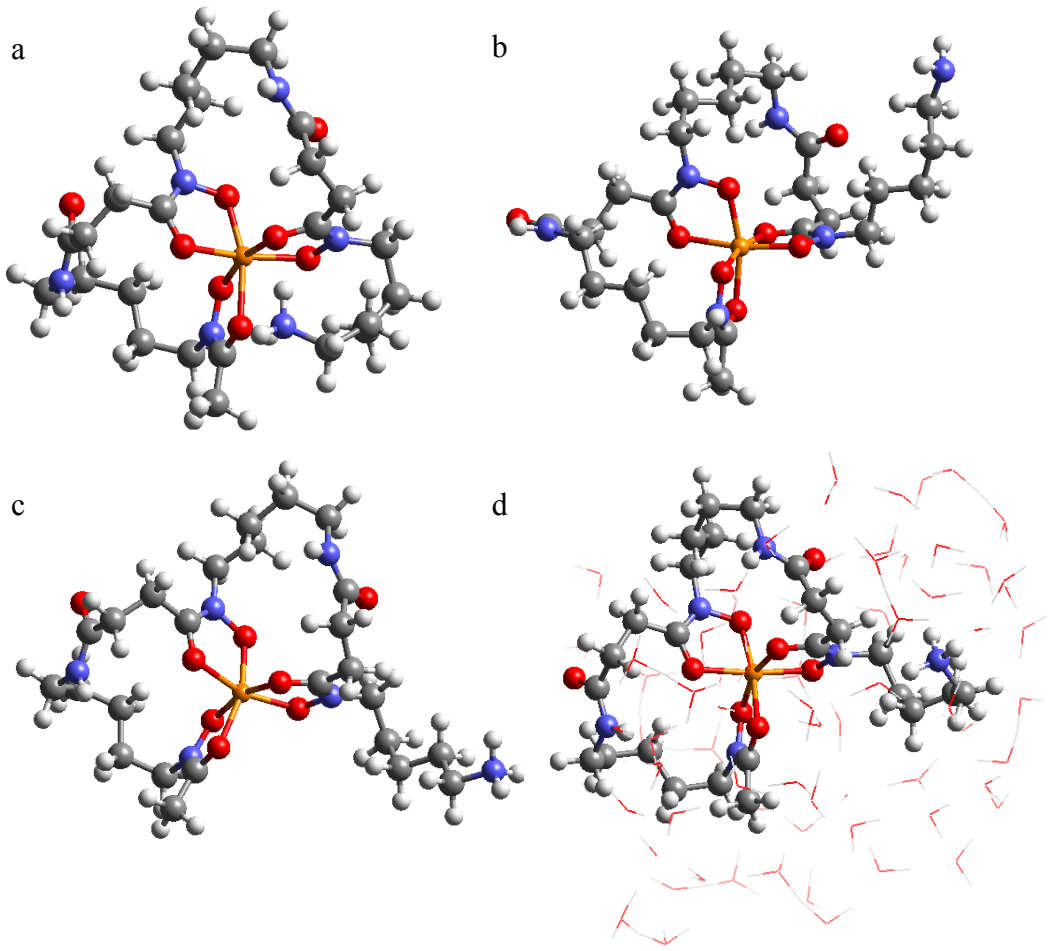

Figure 2-1: Optimized geometries for gas phase, protonated Fe-DFO-B (a); gas phase de-protonated Fe-DFO-B (b); protonated Fe-DFO-B in solution using IEFPCM (c); and Fe-DFO-B in solution using 72 explicit H_2O molecules (d).

To examine the contributions of covalent bonding to the high Fe affinity of DFO-B the orbital occupancies of Fe(II)-, Fe(III)-, and Al(III)-DFO-B were calculated using Natural Bond Orbital (NBO) analysis. NBO calculations were performed using the UB3LYP/6-311++G(d, p) method and the NBO 3.0 utility (CARPENTER and WEINHOLD, 1988; FOSTER and WEINHOLD, 1980; REED and CLARK, 1988; REED and WEINHOLD,

1983; REED et al., 1985) included with Gaussian 03. The orbitals were calculated at the same geometries used for frequency calculations.

Equilibrium fractionation factors were calculated from the predicted vibrational frequencies for the Fe-DFO-B complexes (^{56}Fe and ^{54}Fe) according to the equations of Urey (1947). First, the equilibrium constants for isotope exchange between a complex and its constituent atoms were calculated. This constant is represented by β and is given by the ratio of the partition function with isotope A (Q_A) to the partition function with isotope B (Q_B):

$$\beta = \frac{Q_A}{Q_B} = \prod_i \left(\frac{u_{Ai}}{u_{Bi}} \frac{e^{-u_{Ai}/2}}{1-e^{-u_{Ai}}} \frac{1-e^{-u_{Bi}}}{e^{-u_{Bi}/2}} \right), \quad (2.1)$$

where $u_{Ai} = h\nu_{Ai}/kT$, and the product is taken over the 3N-6 vibrational modes of the complex. In this study, fractionation was predicted for the two most common isotopes of Fe, ^{56}Fe and ^{54}Fe (A = 56 and B = 54). This form of Eq. 2.1 utilizes the ratio of vibrational frequencies (REDLICH, 1935) to convert β into a reduced partition function. As a result, the rotational partition functions do not have to be calculated explicitly and the effects of solution on the substituted masses do not have to be taken into account when using implicit solvation methods such as IEFPCM (Chapter 1). Once β was calculated, the equilibrium fractionation factor, α, was calculated from the ratio of β values for the two complexes. α (and by association, β) are useful in predicting equilibrium fractionations according to the equation:

$$\Delta^{56}Fe(X-Y) \approx 1000 \cdot \ln(\alpha_{X-Y}) = 1000 \cdot \left[\ln(\beta_X) - \ln(\beta_X)\right]. \quad (2.2)$$

2.3 Results and Discussion

2.3.1 Basis Set Effects: Local Bonding Structure

Gas-phase Fe(III)-DFO-B was energy-minimized and compared with experimental single crystal X-ray data for the local bonding environment of Fe (Table 2-1) (BORGIAS et al., 1989). We compared these two sets of data because these bonds are those most important to sequestration and isotopic fractionation of Fe, and because these parameters are the ones that will be least affected by solvation and crystallization of the complex.

Regardless of basis set size, Fe-O(C) bond lengths were overestimated by 0.06-0.08 Å suggesting that the B3LYP electron exchange/correlation functions systematically overestimate bond lengths, a trend that has been observed previously (BORGIAS et al., 1989). Each of the other bond length predictions were within 0.02 Å of experimentally measured values. Axial O-Fe-O bond angles were overestimated by < 1°, except for predictions from the 6-31G (+1.5°) and 6-311G(d) (+1.8°) basis sets. Agreement between 6-31G(d) and 6-31+G(d) results showed that addition of diffuse functions did not significantly impact the predictions. Likewise, the similarity between 6-31G(d) and 6-311G(d) results showed that triple versus double zeta basis sets had a modest effect on predicted structural predictions. In terms of agreement with experimental X-ray diffraction measurements, the most cost effective basis set size examined was 6-31G(d).

Table 2-1: Single-crystal X-ray diffraction (BORGIAS et al., 1989) and DFT (UB3LYP) predicted Fe(III)-DFO-B structural parameters for different basis sets. Experimental measurements are from published X-ray diffraction data (DHUNGANA et al., 2001). The parameters chosen reflect the interface between Fe and the siderophore. Fe-O(X) represents the bond between Fe and O atoms, where the O atom is bound to an atom of X. All numbers are average values for the given parameter.

Parameter	Exp.	6-31G	6-31G(d)	6-31+G(d)	6-311G(d)	6-311+G(d)
Fe-O(C) (Å)	2.037	2.101	2.099	2.112	2.109	2.123
Fe-O(N) (Å)	1.981	1.982	1.962	1.975	1.965	1.982
C-O (Å)	1.282	1.295	1.269	1.269	1.262	1.263
N-O (Å)	1.377	1.410	1.367	1.368	1.364	1.364
N-C (Å)	1.317	1.335	1.331	1.333	1.332	1.332
O-Fe-O (°)	78.7	77.6	77.8	77.3	77.3	76.8
Axial O-Fe-O (°)	164.2	165.7	164.9	164.9	166.0	164.7

2.3.2 Solvation Method Effects: Large-Scale Structure

The effects of solvation were also considered. Although solvation may not dramatically change the local bonding environment of the Fe, it may change the large-scale structure of the complex. For example, when modeling the protonated (i.e., $-NH_3^+$) complex in vacuo, the amine group formed H-bonds with oxygen atoms coordinated to Fe. Intramolecular H-bonding dramatically modified the structure of the complex (Figure 2-1), though the local bonding environment around Fe(III) was well reproduced (Table 2-2). To model the protonated structure found experimentally, solvation effects were considered to prevent the complex from forming intramolecular H-bonds. In one scenario, hydration was accounted for explicitly by surrounding the complex with 72 H_2O molecules. In a second scenario, the IEFPCM (CANCÈS et al., 1997) was used in a UB3LYP/6-31G calculation to implicitly account for hydration (Table 2-2). Differences in predicted bond length for these two methods were less than 0.03 Å for all bonds

involved in Fe complexation. Bond angles showed a 1.8° difference for O-Fe-O bonds and a 6.1° difference for O-Fe-O axial bonds. We consider these errors significant, but they should not dramatically affect the calculated vibrational frequencies, electronic structure or isotopic fractionation factors.

Table 2-2: Fe-DFO-B structure de-protonated in vacuo (DFO-B), protonated in vacuo (DFO-B+), protonated in solution using IEFPCM (PCM), and protonated in solution using 72 waters explicitly (72W). 'Amine N-Fe' distance is not a formal bond length, but represents the distance between the N in the amine tail of DFO-B and the Fe center of the complex. The short amine N-Fe distance in the DFO-B+ model (3.736 Å) is associated with intramolecular H-bonding that is an artifact of the model and highlights the need to take into account the effects of solution.

Parameter	DFO-B	DFO-B+	PCM	72W
Fe-O(C) (Å)	2.109	2.141	2.076	2.073
Fe-O(N) (Å)	1.965	1.956	1.989	1.966
C-O (Å) 1.262	1.314	1.305	1.311	
N-O (Å) 1.364	1.401	1.412	1.442	
N-C (Å) 1.332	1.327	1.332	1.324	
O-Fe-O (˚)	77.3	76.8	77.4	79.2
Axial O-Fe-O (˚)	166.0	163.7	162.0	168.1
Amine N-Fe Distance	8.772	3.736	8.894	7.480

Most importantly, major artificial changes to the Fe(III)-DFO-B complex resulting from intramolecular H-bonding were absent from these solvated models, as evidenced by the relatively constant value for the distance between the amine N and the central Fe. This distance changed by < 1.5 Å between the deprotonated in vacuo model, the implicitly solvated model, and the explicitly solvated model. Compare this to the ~4 Å change caused by protonation of Fe-DFO-B in vacuo. The agreement of the deprotonated in vacuo model with the solvated techniques implies that the short-range structure of Fe-DFO-B can be reasonably approximated by in vacuo models if intramolecular H-bonding is prevented through elimination of the H atoms that form the

model-created H bonds. We recommend IEFPCM methods for future studies in which protonation of the amine group is required, as these mehods reproduce Fe-O bond structure well, avoids artificial H-bonding, and is much less computationally demanding than the explicit methodology.

2.3.3 Discrimination of Fe(III) over Fe(II) and Al(III)

The calculation of geometries for these complexes allows for analysis of the affinity of DFO-B for different metal cations. Specifically, it allows for analysis of how the metal-ligand complexes change upon substitution of the coordinated metal. The local bonding parameters of uncomplexed DFO-B were compared with Fe(III)-, Fe(II)-, and Al(III)-DFO-B to evaluate potential structural differences that may be qualitatively related to the ligand-metal affinity (Table 2-3, Figure 2-2). Replacing Fe(III) with Fe(II) caused lengthening of all Fe-O bonds by more than 0.1 Å and caused O-Fe-O angles to decrease by 1-2.5°. Substitution with Al(III) led to a shortening of M-O bonds by 0.07-0.17 Å and an increase in O-M-O bond angles by 3-4°. These changes were much larger than differences arising from use of various basis sets or solvation. The relative length of the M-O bonds followed the order, Fe(II) > Fe(III) > Al(III), consistent with differences in the ionic radii of the metal cations (0.78 Å for Fe(II), 0.645 Å for Fe(III), and 0.535 Å for Al(III)), but the shorter length of the Al-DFO-B bonds is inconsistent with the preference of DFO-B for Fe(III) over Al(III). The ability of DFO-B to complex Fe(III) and not Al(III) when the two metals are co-present in soils and sediments is critical because Al(III) is harmful to organisms.

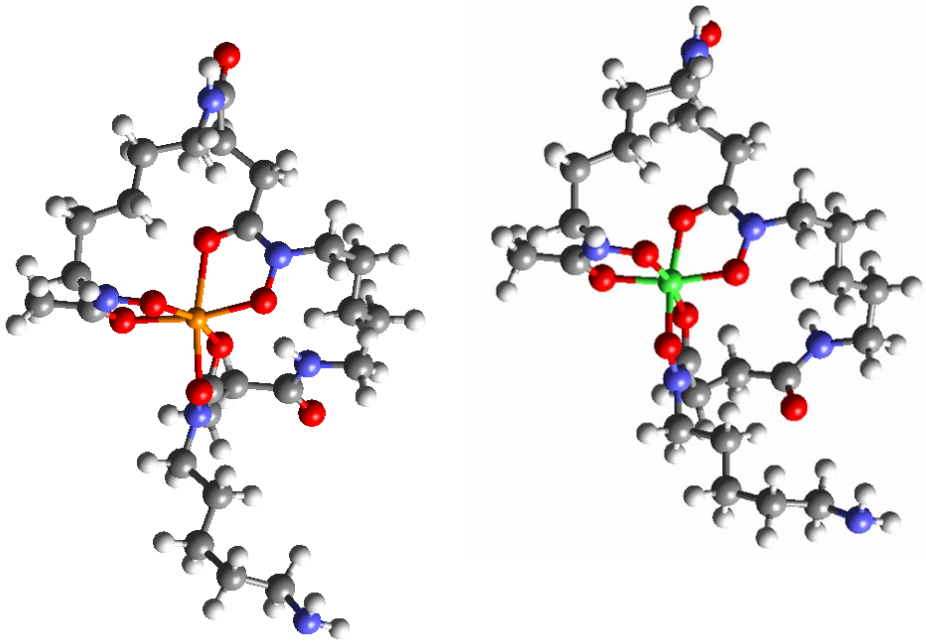

Figure 2-2: Structural effects of cation substitution. Fe(II)-DFO-B is shown on the left and Al(III)-DFO-B is shown on the right. Fe(III)-DFO-B is shown in Figure 2-1.

Table 2-3: Changes in DFO-B conformation without a metal center and bound to Fe(II), Fe(III), and Al(III). Analog values are from Edwards et al. (2001). Predicted values were averaged.

Parameter	Edwards*	DFO-B	Fe(II)	Fe(III)	Al(III)
M-O(C) (Å)	-	-	2.239 (0.030)	2.109 (0.019)	1.958 (0.013)
M-O(N) (Å)	-	-	2.067 (0.006)	1.965 (0.011)	1.894 (0.010)
C-O (Å)	1.243	1.230	1.259 (0.008)	1.262 (0.004)	1.273 (0.004)
N-O (Å)	1.411	1.405	1.360 (0.006)	1.364 (0.003)	1.367 (0.002)
N-C (Å)	1.364	1.363	1.334 (0.005)	1.332 (0.003)	1.323 (0.003)
O-M-O (°)	-	-	74.8 (0.6)	77.3 (0.5)	81.5 (0.5)
Axial O-M-O (°)	-	-	165.1 (4.3)	166.0 (1.2)	169.8 (1.1)

*Predictions of an analog of DFO

Uniqueness of the metal-oxygen bonds in Fe(III)-DFO-B is supported by NBO analysis (Table 2-4), which assigns molecular orbital density using a single electron projection of the full electron distribution, thus allowing the analysis of single electron molecular orbitals (WEINHOLD and LANDIS, 2001). In this study, NBO was used for quantification of the metal cation atomic charges, the occupancy of atomic orbitals, and the atomic orbital contributions to molecular orbitals. The occupancy of natural atomic orbitals agreed with the occupancy expected for the given nuclear charges and calculated electronic charges for the central cations. The natural electronic configurations determined by the NBO analysis were [core]$4s^{0.26}3d^{5.91}4p^{0.01}4d^{0.04}$ with a charge of +1.77 for Fe(III), [core]$4s^{0.21}3d^{6.26}4p^{0.01}4d^{0.02}$ with a charge of +1.49 for Fe(II), and [core]$3s^{0.36}3p^{0.72}3d^{0.02}4p^{0.01}$ with a charge of +1.88 for Al(III). The net charges agree with expectations that Al(III) and Fe(III) have greater positive charges than Fe(II), and with charge transfer in the Fe(III)-DFO-B complex, as measured by Edwards et al. {Edwards, 2005 #349}. Additionally, the proper valence orbitals are occupied in each metal (mostly 4s and 3d in Fe and 3s and 3p in Al).

Table 2-4: Natural Bond Orbital (NBO) analysis of DFO-B complexes with Fe(II), Fe(III), and Al(III). Calculations were performed at the UB3LYP/6-311++G(d,p) level of theory. Orbital occupancies are shown for the metal atoms and the 6 coordinating O atoms. Integers next to the O atoms are strictly for labeling purposes (see Figure 2-3). 2-center covalent bonds are labeled A-B, where A and B are the two atoms donating electrons to the bond. A-B* indicates an anti-bonding orbital between A and B. Lone pair valence electrons are labeled LP. LP* indicates an unoccupied lone pair. Contributions from individual atomic orbitals are also listed. Note the only complex for which the metal cation has electrons in covalent bonds is the Fe(III)-DFO-B complex. The other metals have all their valence electrons in unfilled lone pairs.

	Fe(II)			Fe(III)			Al(III)		
Atom	**Type**	**Occ.**	**Composition**	**Type**	**Occ.**	**Composition**	**Type**	**Occ.**	**Composition**
O 27	O-N	0.9931	49% $sp^{4.68}_{O}$, 51% $sp^{2.90}_{N}$	O-N	0.9917	51% $sp^{4.40}_{O}$, 49% $sp^{3.07}_{N}$	O-N	0.9938	51% $sp^{4.62}_{O}$, 49% $sp^{3.11}_{N}$
	LP	0.9842	59% s, 42% p	O-Fe	0.9813	87% $sp^{4.15}_{O}$, 13% $sd^{2.09}_{Fe}$	LP	0.9821	36% s, 64% p
	LP	0.9211	21% s, 79% p	O-Fe	0.953	89% p_{O}, 11% $sd^{30.34}_{Fe}$	LP	0.9397	100 % p
	LP	0.9128	3% s, 97% p	LP	0.9794	62% s, 38% p	LP	0.9094	46% s, 54% p
O 28	O-N	0.9931	49% $sp^{4.65}_{O}$, 51% $sp^{2.89}_{N}$	O-N	0.9918	51% $sp^{4.40}_{O}$, 49% $sp^{3.06}_{N}$	O-N	0.9938	51% $sp^{4.63}_{O}$, 49% $sp^{3.12}_{N}$
	LP	0.9832	61% s, 39% p	O-N	0.9429	65% p_{O}, 35% p_{N}	LP	0.9818	36% s, 64% p
	LP	0.9208	7% s, 93% p	O-N*	0.6967	35% p_{O}, 65% p_{N}	LP	0.9414	100% p
	LP	0.9134	15% s, 85% p	O-Fe	0.9817	87% $sp^{4.23}_{O}$, 13% $sd^{2.40}_{Fe}$	LP	0.91	46% s, 54% p
				LP	0.9794	63% s, 37% p			
O 57	O-N*	0.975	52% p_{O}, 48% p_{N}	O-C	0.9934	65% $sp^{1.72}_{O}$, 35% $sp^{2.23}_{C}$	O-C	0.9939	65% $sp^{1.63}_{O}$, 35% $sp^{2.31}_{C}$
	O-N	0.613	48% p_{O}, 52% p_{N}	O-Fe	0.964	91% $sp^{6.83}_{O}$, 9% $sd^{2.32}_{Fe}$	LP	0.9704	36% s, 64% p
	O-C	0.9947	64% $sp^{1.61}_{O}$, 36% $sp^{2.17}_{C}$	LP	0.9744	50% s, 50% p	LP	0.909	26% s, 74% p
	LP	0.9768	55% s, 45% p	LP	0.7985	100% p	LP	0.8352	100% p
	LP	0.9184	6% s, 94% p						
O 72	O-N	0.9935	49% $sp^{4.56}_{O}$, 51% $sp^{2.89}_{N}$	O-Fe	0.9512	87% p_{O}, 13% $sd^{25.64}_{Fe}$	O-N	0.9938	51% $sp^{4.52}_{O}$, 49% $sp^{3.20}_{N}$
	LP	0.9839	60% s, 40% p	O-N	0.9915	51% $sp^{4.14}_{O}$, 49% $sp^{3.15}_{N}$	LP	0.9819	36% s, 64% p
	LP	0.9245	13% s, 87% p	LP	0.9786	62% s, 38% p	LP	0.9399	100% p
	LP	0.9076	9% s, 91% p	LP	0.8623	18% s, 82% p	LP	0.9087	46% s, 54% p
Fe/Al	LP*	0.1241	100% d	Fe-O27	0.9813	87% $sp^{4.15}_{O}$, 13% $sd^{2.09}_{Fe}$	LP*	0.178	100% s
	LP*	0.1209	100% d	Fe-O27	0.9813	89% p_{O}, 11% $sd^{30.34}_{Fe}$	LP*	0.1232	100% p
	LP*	0.1011	98% s, 2% d	Fe-O28	0.9817	87% $sp^{4.23}_{O}$, 13% $sd^{2.40}_{Fe}$	LP*	0.1225	100% p
	LP*	0.0658	100% d	Fe-O57	0.964	91% $sp^{6.83}_{O}$, 9% $sd^{2.32}_{Fe}$	LP*	0.1166	100% p
	LP*	0.0569	100% d	Fe-O72	0.9512	87% p_{O}, 13% $sd^{25.64}_{Fe}$			
	LP	0.9726	100% d	LP	0.1577	100% d			

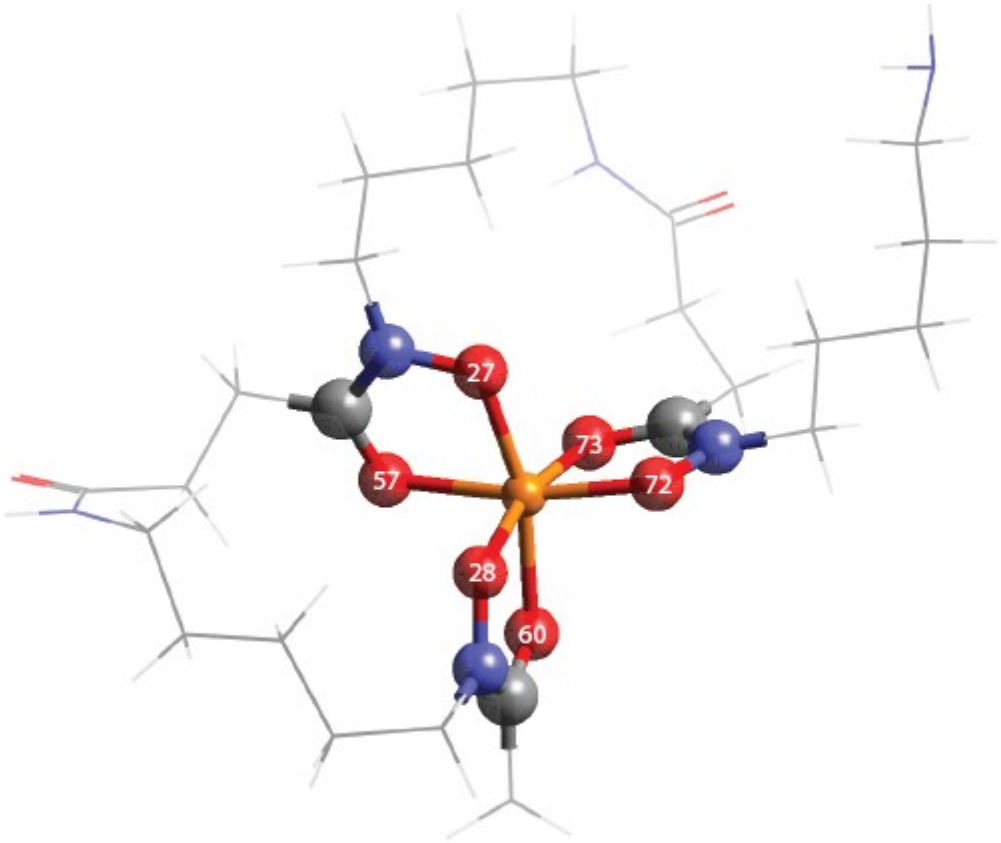

Figure 2-3: O atoms (in red) bound to central Fe atom are labeled with numbers consistent with those listed in Table 2-4. The numbering is consistent across different models – Fe(II), Fe(III), and Al(III).

The metal-oxygen bonds were completely ionic when DFO-B complexed Fe(II) and Al(III), but covalent when DFO-B complexed Fe(III). Table 2-4 also shows the occupancy of each NBO in Fe(II)-, Fe(III)- and Al(III)-DFO-B, as well as the contributions from individual atomic orbitals to the NBO. Fe(II)-DFO-B and Al(III)-DFO-B did not exhibit any covalent bonding between the central cation and DFO-B, but covalent Fe-O bonds were predicted for the Fe(III)-DFO-B complex. The average occupancy of these Fe-O bonds was 0.9829, 91% of which was contributed by electrons

from the O atom (86% from the valence *p* orbital of O). The Fe-O bonds of Fe(III)-DFO-B all had high occupancy and were composed primarily of electrons from the *p* orbitals of the O atom with minor contributions from the *s* orbital of O and a hybrid *sd* orbital of Fe. The presence of covalent bonding between the *sp* orbital of O and the *sd* orbital of Fe was the primary reason for the high affinity for Fe(III). DFO-B's next highest affinity is for Al(III), a cation for which no covalent bonds were predicted in our analysis, but which has a smaller ionic radius than the other cation without covalent bonds, Fe(II). In Fe(II), the extra electron charge that would otherwise occupy covalent Fe-O bonds were unevenly distributed amongst the O atoms.

2.3.4 IR Frequencies

Accurate predictions of IR vibrational frequencies can be used to further validate the predicted geometries and to predict equilibrium isotope effects between different Fe complexes. The predicted IR vibrational frequencies for the de-protonated Fe(III)-DFO-B in vacuo and protonated Fe(III)-DFO-B in solution (modeled implicitly using the IEFPCM method) reproduced the experimentally measured IR frequencies with reasonable accuracy, particularly for the solvated model (Table 2-5 and Figure 2-4). The mean difference between the predicted gas-phase IR frequencies and experimental IR frequencies was 19 cm^{-1}, an average relative error of 1.31%, and the root-mean-squared difference (RMSD) was 26 cm^{-1}. The mean difference between the IEFPCM predicted IR frequencies and experimental IR frequencies was 15 cm^{-1}, an average error of 1.22%, and the RMSD was 18 cm^{-1}. The accuracy of the IR frequency predictions are slightly better

than a previous theoretical study performed on an analog of DFO-B (Table 2-5, EDWARDS et al., 2005), which exhibited an average error 23 cm^{-1}, 1.53% average relative error, and RMSD of 32 cm^{-1}.

Table 2-5: Comparison of observed and calculated IR vibrational frequencies (scaled). Frequencies are listed in cm^{-1}. Intensities are listed in cm^{-2}/mol/L, converted from km/mol using a factor of 100 (KUBICKI et al., 1993). The calculations from Edwards et al. (2005) were for an uncomplexed model, and those from this study are for the full Fe(III)-DFO-B complex. The listed assignments are from IR measurements published in the Edwards et al. (2005) paper.

	Edwards et al. (2005)		**This Study**			
Exp.	**Theoretical**	**Assignment**	**In Vacuum**	**Inten.**	**IEFPCM**	**Inten.**
1049	1036	νC-C (29)	1046	2205	1031	2010
		νC-N (8)				
1184	1188	δC-H twist (54)	1196	4045	1170	7672
		δC-H wag (12)				
1209	- -	-	-	1236	6425	
1355	1351	δC-H wag (58)	1324	5078	1347	3933
		δC-H twist (8)				
1374	1375	νC-N (oxime) (18)	1380	2806	1390	20273
		δC-H wag (17)				
		δC-H rock (terminal N) (16)				
		δC-H twist (8)				
1421	1427	δCCN bend (80)	1418	4221	1428	4969
		δCCC bend (15)				
1453	1486	δNOH bend (oxime) (55)	1449	5642	1477	7276
		νC-N rock (oxime) (19)				
		νC-N rock (adj. to oxime) (14)				
1577	1621	νC=O (oxime) (76)	1543	23114	1582	32335
1627	1705	νC=O (amide) (76)	1688	45111	1599	10789
		νC-N (oxime) (8)				

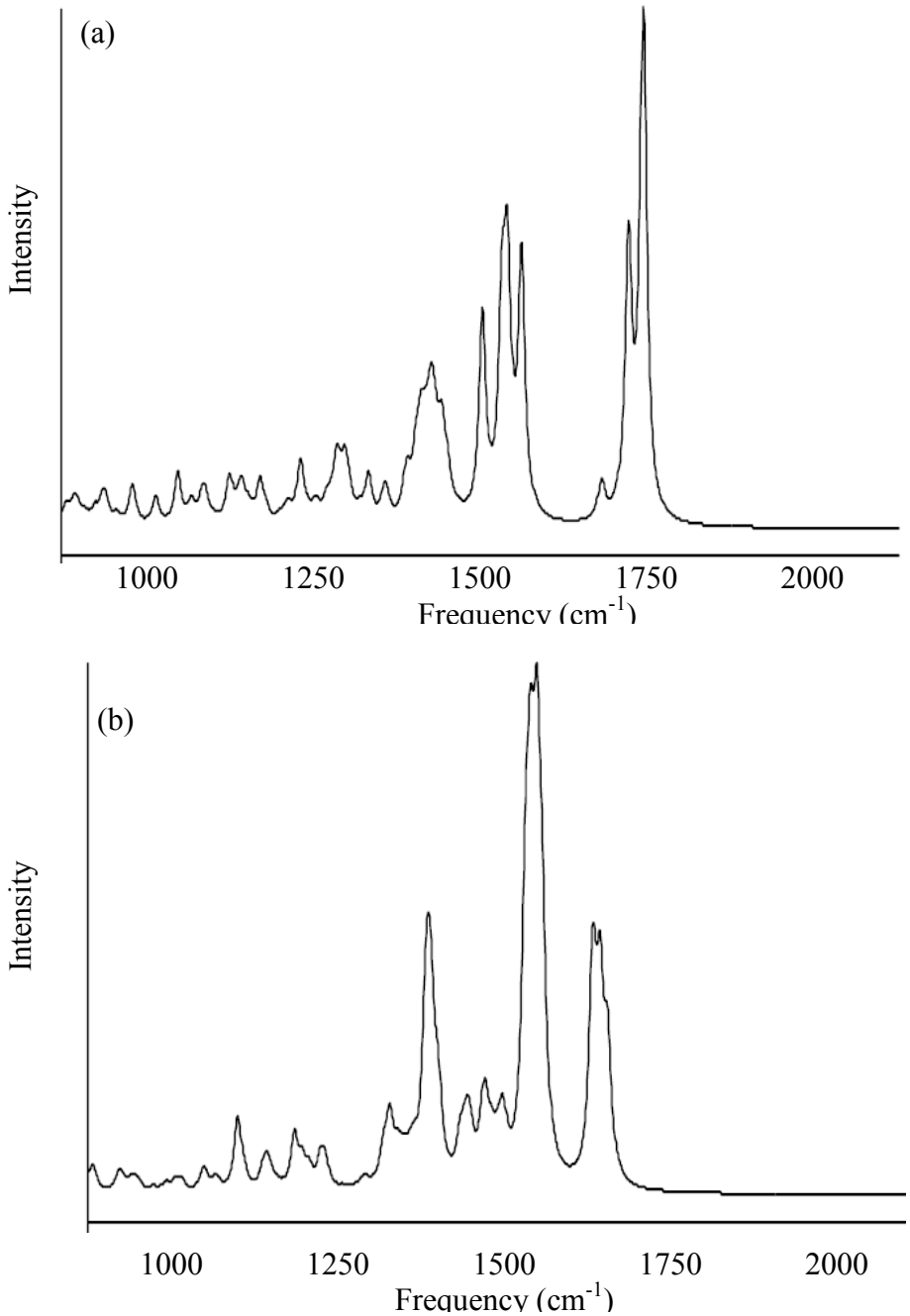

Figure 2-4: Predicted IR spectra for gas phase Fe(III)-DFO-B (a) and the IEFPCM method (b). The predicted IR spectra were produced using the program Molden. The peaks shown are Gaussian functions with linewidths of 5 cm^{-1}.

The advantages of incorporating solvation effects and the full DFO-B structure were more apparent when considering the whole set of frequency predictions. If the model predictions exactly reproduced the experimental measurements, then all model frequencies would fall on the line y=x when plotted as a function of experimental frequencies. The best fit line for the gas phase calculations was y = 1.0287x – 38.97, with an r^2 value of 0.98. The best fit line for the solvated model was y = 1.0019x – 1.513, with an r^2 value 0.99. Most of the decrease in error associated with implicit solvation methods resulted from a reduced overestimation of the C=O stretching modes. The IEFPCM calculation of the 1577 cm^{-1} and 1626 cm^{-1} vibrational modes were in error by 5 cm^{-1} and 28 cm^{-1}, respectively, compared to errors of 34 cm^{-1} and 61 cm^{-1} for DFO-B in vacuo calculations, and 44 cm^{-1} and 78 cm^{-1} respectively, for calculations of a DFO-B analog in vacuo (Edwards et al., 2005). This overestimation caused a greater slope than unity and more negative y-intercept expressed by the in vacuo model. The improved accuracy of the solvated full DFO-B model is important for calculating equilibrium isotope constants as they exponentially depend on the predicted frequencies.

The average error in the predicted IR frequencies was 0.51% of the reported experimental IR frequencies. The average error in the predicted frequencies for various Fe-organic complexes (Chapter 1) using the UB3LYP/6-311G(d) method was ~3.34%. Because of the lack of vibrational modes lower than 1000 cm^{-1} in the Edwards et al. (2005) spectra, we use the latter percentage when evaluating the accuracy of the Fe isotope fractionation factors.

Because the errors of predicted IR frequencies could be quantified, the errors of the equilibrium isotope fractionation predictions could be estimated. The upper bound of

the error on the Fe isotope fractionation factors can be estimated by recalculating $1000 \cdot \ln(\beta)$ values according to Eq. 2.1, where all frequencies were increased by 3.34%. Likewise, the lower bound of the error can be estimated by decreasing all frequencies by 3.34% before calculating $1000 \cdot \ln(\beta)$. This likely overestimates the error present in these calculations as it assumes that all of the IR frequencies contain a systematic over-prediction or under-prediction; if the errors in the predicted IR frequencies were distributed randomly the errors in the $1000 \cdot \ln(\beta)$ predictions would be smaller. This, these estimated can be considered conservative treatment of the errors due to inaccurate vibrational frequency predictions. Errors in predictions of $1000 \cdot \ln(\alpha)$ can be estimated by propogating the errors in the $1000 \cdot \ln(\beta)$ values for both species involved in the equilibrium reaction.

2.3.5 Isotopic Equilibrium in Solution

The accuracy of the energy minimized structures and the IR vibrational frequencies for the Fe-DFO-B complexes make the calculation of equilibrium isotope fractionations a reasonable endeavor. $1000 \cdot \ln(\beta)$ values have been predicted for both Fe(II) and Fe(III) coordinated with H_2O (ANBAR et al., 2005; JARZECKI et al., 2004), complexed by oxalate (Chapter 1), and now complexed by DFO-B (Figure 2-5). Equilibrium Fe isotope fractionations can be predicted for the different Fe species in solution (Eq. 2.2).

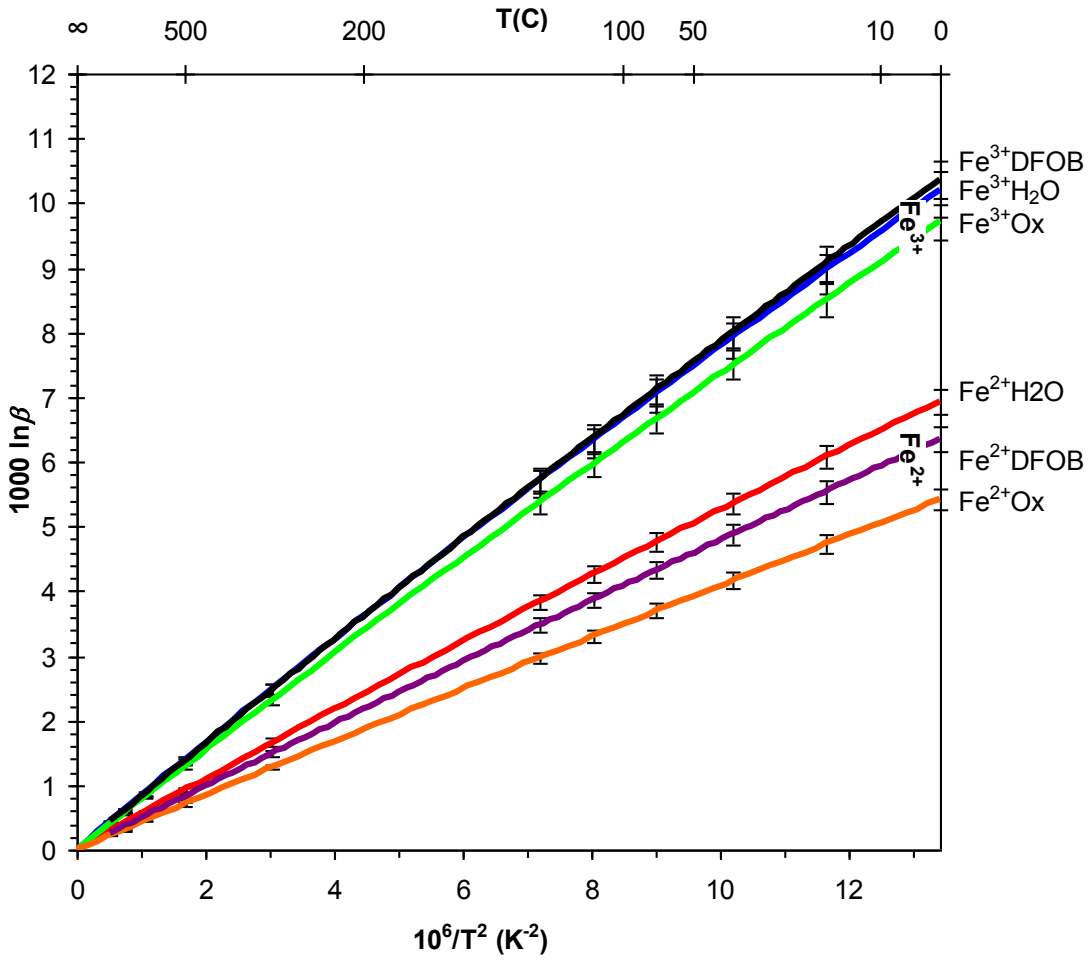

Figure 2-5: 1000·ln(β) values plotted against $1/T^2$ (10^6K^{-2}). Note the separation between Fe^{3+} and Fe^{2+} phases, which indicates the importance of redox reactions in the isotope reactions. Values for Fe-$(H_2O)_6$ and Fe-$(oxalate)_3$ are from Chapter 1. Error bars were calculated by increasing and then decreasing all predicted frequencies by 3.34%.

The predicted equilibrium fractionations for the H_2O-oxalate-DFO-B systems at 25ºC (Table 2-6) are dominated by redox reactions. Fractionations of ~3‰ between Fe(III) and Fe(II) in water have been reported experimentally and predicted during equilibrium with methods similar to those used in this study (Chapter 1, ANBAR et al., 2005). However, not all of the phases will be present in significant quantities

simultaneously. Under normal, oxidizing surface conditions most of the Fe in solution will be complexed with organic molecules and equilibrium will be established between Fe-DFO-B and Fe-Oxalate, as most of the Fe in solution will be either bound by organics or oxidized and precipitated.

Table 2-6: Predicted $1000 \cdot \ln(\alpha)$ values for equilibrium fractionation between Fe complexed with H_2O, oxalate (Ox), and desferrioxamine B (DFO-B) for both Fe(II) and Fe(III). Values were calculated by subtracting the $1000 \cdot \ln(\beta)$ of the column from the $1000 \cdot \ln(\beta)$ of the row. Therefore, positive values are indicative of the row label having a higher demand for ^{56}Fe. $1000 \cdot \ln(\beta)$ values for Fe-H_2O and Fe-$(Ox)_3$ are from Chapter 1. Equilibrium reactions involving only Fe(III) are shown in the first table and those involving only Fe(II) are shown in the second table. Redox reactions involving both Fe(III) and Fe(II) are shown in the third table. Note the larger numbers in the third table, indicating the importance of redox reactions and the fractionations predicted between Fe-DFO-B and Fe-oxalate, which are comparable to fractionations measured in the laboratory (BRANTLEY et al., 2001) between cells and solution during dissolution of hornblende. Errors were assumed to be the sum of errors in the prediction of the $1000 \cdot \ln(\beta)$ value for both species in the reaction.

Ligand	**Fe(III)-H_2O**	**Fe(III)-Ox_3**	**Fe(III)-DFO-B**
Fe(III)- H_2O	-	0.46 +0.50/-0.51	-0.11 ±0.52
Fe(III)-Ox_3	-0.46 +0.50/-0.51	-	-0.58 ±0.52
Fe(III)-DFO-B	0.11 ±0.52	**0.58 ±0.52**	-

Ligand	**Fe(II)- H_2O**	**Fe(II)-Ox_3**	**Fe(II)-DFO-B**
Fe(II)- H_2O	-	1.35 ±0.32	0.53 ±0.35
Fe(II)-$(Ox)_3$	-1.35 ±0.32	-	-0.82 +0.31/-0.32
Fe(II)-DFO-B	-0.53 ±0.35	**0.82 +0.31/-0.32**	-

Redox	**Fe(II)- H_2O**	**Fe(II)-Ox_3**	**Fe(II)-DFO-B**
Fe(III)- H_2O	2.89 ±0.43	4.23 +0.39/-0.40	3.42 ±0.42
Fe(III)-$(Ox)_3$	2.43 ±0.43	3.77 +0.39/-0.40	2.95 ±0.42
Fe(III)-DFO-B	3.00 +0.44/-0.45	4.35 ±0.41	3.53 ±0.44

At equilibrium, Fe(III)-DFO-B was predicted to be 0.58 ± 0.52‰ heavier than Fe(III)-$(Oxalate)_3$ and 0.11 ± 0.52‰ heavier than Fe(III)-$(H_2O)_6$; Fe(II)-DFOB was predicted to be 0.82 ± 0.32‰ heavier than Fe(II)-$(Oxalate)_3$ and 0.53 ± 0.35‰ lighter than Fe(II)-$(H_2O)_6$. The predicted equilibrium fractionation between Fe-DFO-B and Fe-$(oxalate)_3$ (~0.56 – 0.80‰) was similar to the difference between the isotopic

composition of Fe in cells and Fe remaining in solution during hornblende dissolution, measured to be 0.72 ± 20‰ (BRANTLEY et al., 2001). Agreement between these predictions is consistent with equilibrium between Fe-$(oxalate)_3$ and Fe-DFO-B, with the Fe in Fe-DFOB being moved to cells without fractionation during release of Fe. None of the other fractionations calculated in this study can explain the fractionation measured in the laboratory. While other fractionations may exist in the system, including reactions inside cells and during transfer of Fe from siderophores to the cell, the fractionation reported by Brantley et al. (2001) between cells and solution during uptake of Fe can be explained entirely by the predicted equilibrium fractionations between Fe complexed to small organic ligands and Fe complexed to siderophores.

Despite the high affinity DFO-B has for Fe, experiments have shown that the rate at which Fe is leached from mineral surfaces increases when DFO-B can act in the presence of oxalate (CHEAH et al., 2003). This implies that Fe sequestration occurs through a multi-step process, with leaching of Fe by small organic ligands followed by complexation in solution by siderophores, and ending with delivery of Fe to cells via Fe-siderophore complexes. Our results support this model, as the agreement of our predicted equilibrium Fe isotope fractionation between Fe-DFO-B and Fe-oxalate with experimental differences between cells and solution during hornblende dissolution is consistent with delivery of Fe to cells exclusively via Fe-DFO-B complexes. Kinetic and equilibrium fractionations have also been shown to exist during dissolution of minerals (BRANTLEY et al., 2001; BRANTLEY et al., 2004; WIEDERHOLD et al., 2006) and during precipitation of Fe(III) phases (WELCH et al., 2003). Thus, there seem to be at least three sources of fractionation during biological uptake of Fe: dissolution of the initial mineral

phase by small organic ligands, equilibrium between various Fe-ligand complexes in solution, and precipitation of inorganic mineral phases.

While formal quantification of the speciation of organic Fe complexes delivering Fe has not yet taken place, siderophores have a much higher Fe affinity and as a result complex most of the Fe in solution. The results of NBO analysis suggest the high affinity of DFO-B for Fe(III) is the presence of six covalent Fe-O bonds in octahedral coordination around the Fe atom that are absent in Al(III)-DFO-B and Fe(II)-DFO-B. In Fe(III)-DFO-B, the Fe(III)-O bonding orbitals are fully populated – it is these orbitals that make siderophores so efficient at sequestering Fe from the environment and removing Fe from oxalate. If these orbitals were unpopulated, the longer bond lengths of Fe(III)-DFO-B (compared to Al(III)-DFO-B) predicted by ionic radii would lead to lower Fe-O bond strength.

2.4 Conclusions

This article explores different methodologies for modeling Fe-siderophore complexes, examines the cause of the high Fe affinity expressed by siderophores, and predicts the equilibrium fractionations caused by Fe-siderophore complexes in solution. Our results lay the foundation for investigations into modeling kinetic reactions at the mineral surface during dissolution of Fe and experimental work on the distribution of Fe into different organic phases during uptake of Fe.

We have shown that UB3LYP is effective at predicting the geometries and frequencies of Fe-siderophore complexes in solution, and based on our analysis of

different basis sets, we recommend that as research progresses to larger siderophores and MO/DFT examinations of siderophore-mineral interactions, use of the 6-31G(d) basis set is adopted. This basis set provides reasonable geometries at moderate computational cost. We further recommend the use of implicit solvation techniques. Without any solvation technique, deprotonation of the structure may by necessary to avoid the formation of H-bonds that do not exist in solution. On the other hand, implicit methods seem to produce geometries comparable to those predicted through significantly more expensive explicit methods. As such, attempts should be made to utilize IEFPCM and similar methods to prevent the formation of intra-molecular hydrogen bonds without large increases in computational cost. We are not suggesting implicit solvation techniques such as IEFPCM as a panacea, but rather as a reasonable method to employ when problems with artificial intramolecular H-bonds arise.

CHAPTER 3

Organic Haze, Glaciations and Multiple Sulfur Isotopes in the Mid-Archean Era

Abstract:

Sulfur isotope signatures within ancient sediments have been used to interpret the evolution of the atmosphere over the first half of Earth's history. It is widely accepted that the presence of an anomalous multiple sulfur isotope signature indicates that atmospheric O_2 concentrations were low prior to ~2.45 billion years ago (Ga) and that the sudden disappearance of the signature indicates that O_2 concentrations rose at that time. This rise of atmospheric oxygen coincides with glacial deposits, which plausibly resulted from the oxidation of the atmosphere and corresponding decreases in atmospheric CH_4 concentrations. Similar glacial and sulfur isotope patterns have recently been found in Archean rocks deposited between ~2.7 Ga and ~3.2 Ga, suggesting that these signatures were causally linked at a time when atmospheric O_2 concentrations are thought to have been low. Thus, a different connection between the two data sets may be required. Here, we present new multiple sulfur isotope data for the Archean, along with a new model to explain them. We suggest that, prior to the rise of oxygen, excursions in the sulfur isotope record were modulated by the presence or absence of an organic haze that altered the tropospheric UV fluxes responsible for the anomalous sulfur photochemistry. Changes in atmospheric CH_4 and CO_2 concentrations could also have altered the vertical distribution of SO_2 in ways that would have affected sulfur isotope fractionation. Our model can

explain the glacial and sulfur isotope data without violating other geological and geochemical constraints on the oxidation state of the Archean atmosphere.

3.1 Introduction

Detailed knowledge of the Earth's early atmosphere is important for constraining geochemical, geophysical, and biological evolution. Gaining a better understanding of the evolution of the atmosphere over the first 2 Gyr (billion years) of Earth's history will help us better understand the relationships between the atmosphere, climate, and biota, while improving our ability to search for sustainable biospheres dissimilar from that found on the modern Earth. One tool that has proven useful in tracking photochemical processes on the early Earth has been the measurement of multiple sulfur isotopes in sedimentary rocks. In particular, such studies have helped to better define the transition from an O_2-poor to an O_2-rich atmosphere. This major event in the evolution of the atmosphere occurred at ~2.4 Ga (billion years ago) (CLOUD, 1972; HOLLAND, 1994; WALKER et al., 1983), and is marked by a decrease in the range of $\Delta^{33}S$ (where $\Delta^{33}S = \delta^{33}S - 1000\cdot[(1+\delta^{34}S/1000)^{0.515}-1]$, $\delta^{3i}S = 1000\cdot({}^{3i}R/{}^{3i}R_{V\text{-}CDT} - 1)$, and ${}^{3i}R=({}^{3i}S/{}^{32}S)$ from greater than 10‰ to less than 0.3‰ (BEKKER et al., 2004, for a dissenting view; FARQUHAR et al., 2000; FARQUHAR et al., 2001; OHMOTO et al., 2005; PAVLOV and KASTING, 2002). To date, the only tenable explanation for high $\Delta^{33}S$ values in sediments is the absence of appreciable atmospheric O_2 and O_3. Atmospheric O_2/O_3, if present, would have shielded the troposphere from the UV photons required to produce the $\Delta^{33}S$ via photolysis of S-bearing gases (FARQUHAR et al., 2000; FARQUHAR et al., 2001;

FARQUHAR and WING, 2003). Furthermore, trace amounts of atmospheric O_2 would have caused all atmospheric sulfur species to be oxidized, eliminating the ability for a tropospheric $\Delta^{33}S$ signal to be preserved in sediments (PAVLOV and KASTING, 2002). Based on these relationships, all of these studies used the decrease in $\Delta^{33}S$ at ~2.45 Ga to date a rise in global atmospheric O_2 concentrations.

Prior to the oxygenation event, the atmosphere probably contained appreciable concentrations (~1000 ppmv) of both H_2 and CH_4 (CANFIELD, 2005; CATLING et al., 2001; KASTING et al., 1983; KHARECHA et al., 2005; PAVLOV et al., 2001a; WALKER, 1977). Photochemical models have demonstrated that CH_4 should have been present in these abundances in an anoxic atmosphere, given a modern CH_4 flux. Coupled ecosystem-atmosphere models of the Archean biosphere show that such a CH_4 flux should have been reached soon after methanogenesis evolved (KHARECHA et al., 2005). Empirical support for the presence of methanogenesis in the Archean is provided by the recent discovery of low-^{13}C methane in fluid inclusions in 3.4 Ga sediments (UENO et al., 2006). High CH_4 concentrations, along with enhanced CO_2 levels, could have produced enough greenhouse warming to counter low solar luminosity and keep the Archean Earth warm (PAVLOV et al., 2000). Destruction of the methane greenhouse by rising O_2 can explain why low-latitude Paleoproterozoic glaciations occurred at ~2.45 Ga (BEKKER et al., 2005; PAVLOV et al., 2000; ROSCOE, 1969), consistent with the hypothesis that changes in atmospheric composition can have a dramatic effect on climate.

Both climate and $\Delta^{33}S$ production may have varied before the rise of oxygen. Diamictites have been identified in the ~2.9 Ga Pongola and Witwatersrand Supergroups of South Africa (CROWELL, 1999; YOUNG et al., 1998) and in the contemporaneous

Belingwe greenstone belt in Zimbabwe (NISBET et al., 1993). Diamictites by themselves cannot always be interpreted as glacial tillites, as they can also form by other processes (*e.g.*, underwater landslides or terrestrial mudflows). However, the Pongola rocks also contain striated and faceted clasts interpreted as dropstones (YOUNG et al., 1998), so it is likely that these sediments were glacial.

Intriguingly, $\Delta^{33}S$ values exhibit a distinct minimum at around this same time (Figure 3-1). One possible explanation is the so-called "yo-yo atmosphere" model, in which atmospheric O_2 concentrations are suggested to have increased at ~3.2 Ga, decreased at ~2.7 Ga, and then increased permanently at ~2.45 Ga (OHMOTO et al., 2006). However, such a model may be inconsistent with the presence of reduced detrital minerals in the Witwatersrand gold deposits that formed at about this time (KASTING and HOWARD, 2006), which implies that atmospheric O_2 concentrations must have remained below ~10^{-2} PAL (times the Present Atmospheric Level) (HOLLAND, 1984). Here, we suggest that both the smaller range of mid-Archean $\Delta^{33}S$ and the 2.9-Ga glaciations were caused by an entirely different mechanism, namely, the appearance of an optically thick organic haze, as previously proposed by Sagan and Chyba (SAGAN and CHYBA, 1997) and Pavlov et al. (PAVLOV et al., 2001a). An organic haze could have shielded SO_2 from the photolysis reactions thought to be responsible for the formation of large $\Delta^{33}S$. At the same time, it could have cooled the Earth's surface by creating an anti-greenhouse effect (MCKAY et al., 1991). Thinning of this haze at ~2.7 Ga may have restored warm conditions and set the stage for large $\Delta^{33}S$ values in the Late Archean.

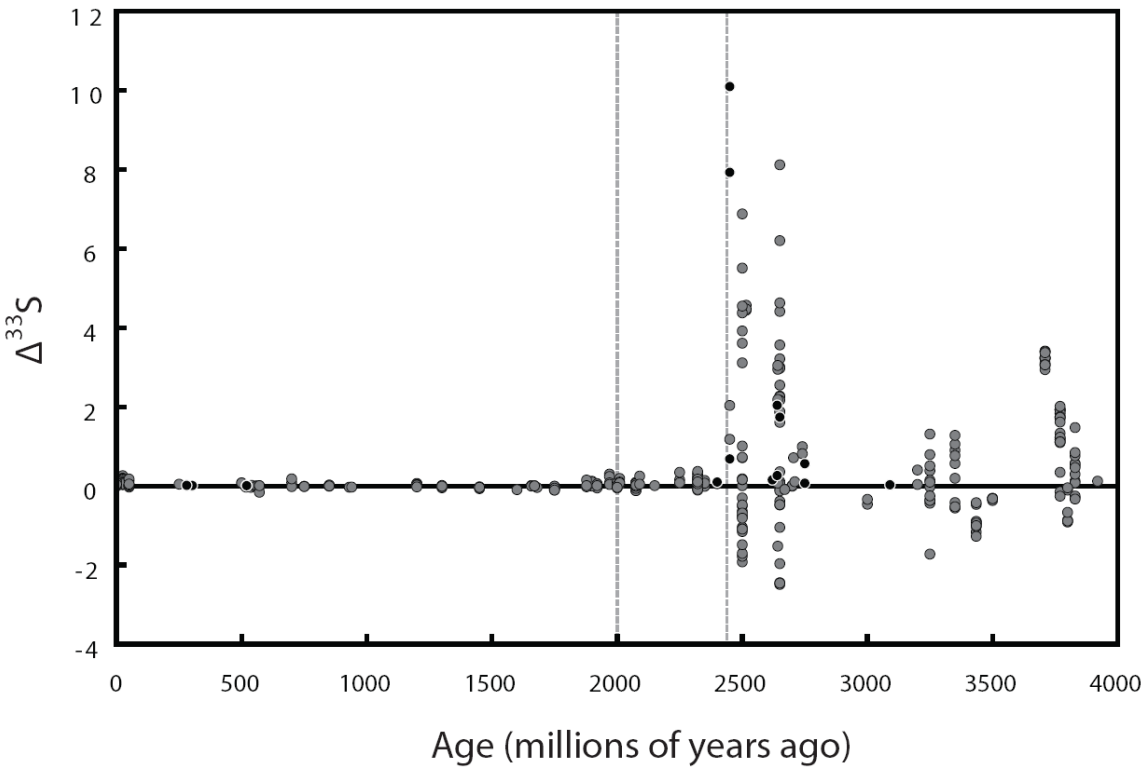

Figure 3-1: A compilation of new (see Table 3-1) and published (FARQUHAR et al., 2002; HU et al., 2003; MOJZSIS et al., 2003; PAPINEAU et al., 2005; WHITEHOUSE et al., 2005) sulfur isotope data. a) Here, sulfur isotope data ($\Delta^{33}S$) are plotted against age. New data are represented by black-filled circles, and previously published data are plotted in grey-filled circles. The two gray bands at 2.71 Ga and 3.0 Ga show the timing of data from the Kameeldoorns Formation and Witwatersrand Basin, which express $\Delta^{33}S$ between -0.46 and +0.57 ‰ (PETERS et al., 2006). The plot shows wide variations in $\Delta^{33}S$ for late Archean samples (ranging from –2.45 to +10.10 ‰), and a reduced range of $\Delta^{33}S$ between ~3.2 and 2.7 Ga. It also illustrates the significant number of mass dependent samples reported that have an age between 2.7 and 2.45 Ga.

3.2 New Multiple Sulfur Isotope Data

Our study is based partly on new multiple sulfur isotope data. Here, we briefly describe how those data were obtained. PPRG samples (Table 3-1) were graciously

provided by W. J. Schopf; the remaining samples are from Claypool et al. (CLAYPOOL et al., 1980). All carbonate sulfur was extracted from crushed carbonate samples that were leached with sodium hypochlorite solution following the methods in (BURDETT et al., 1989). After leaching, samples were dissolved in 3N HCl and filtered. The resulting solution was evaporated at 80˚C in a HEPA-filtered box. Samples were then reduced to Ag_2S using the method described by Forrest and Newman (FORREST and NEWMAN, 1977). Ag_2S samples were fluorinated under a 10X F_2 atmosphere, producing SF_6, which was cleaned via cryogenic and chromatographic techniques. Isotope analyses were performed using a Thermofinnigan MAT 253 isotope ratio mass spectrometer (dual inlet) at *m/e* of 127-129. Uncertainties are based on long-term reproducibility of international standards, and are 0.008 and 0.14 permil for $\Delta^{33}S$ and $\delta^{34}S$ respectively. Because the abundances of extracted sulfur were low, the sulfur extracted from these samples may be mixture of primary sulfate and sulfate derived from pyrite; it is nevertheless indigenous to the samples that we have studied.

Temporal trends in $\Delta^{33}S$ prior to the well-documented decrease at ~2.4 Ga have begun to emerge, and are reinforced by the data presented here (Figure 3-1). Prior to ~3.2 Ga, rocks with $\Delta^{33}S$ values as high as 3.2 ‰ (WHITEHOUSE et al., 2005) and as low as -1.8 % (MOJZSIS et al., 2003) have been reported. The spread in $\Delta^{33}S$ values is attenuated between ~2.7 and ~3.2 Ga, with data ranging from -0.51‰ to 0.57 ‰. More specifically, data from the 2.76-Ga Hardey Fm. and the 2.92-Ga Mosquito Creek Fm. range between -0.51 and +0.25 ‰ (OHMOTO et al., 2006); data from the ~2.9-Ga Pongola Supergroup fall between -0.49 and +0.37 ‰ (ONO et al., 2006a); and data from the 2.71-Ga

Kameeldoorns Formation and the ~3.0-Ga Witswatersrand basin yield values between -0.46 and +0.57 ‰ (PETERS et al., 2006). Assuming the current data are robust, the period of attenuated $\Delta^{33}S$ lasts for at least ~200 Myr (2.71-2.92 Ga), and given the lack of well dated, analyzed samples between 2.92 and 3.2 Ga, it could have lasted for as long as ~500 Myr (~2.7-3.2 Ga). Following this minimum and up until 2.4 Ga (from 2.4-2.7 Ga), a much larger range of $\Delta^{33}S$ values is observed, with reported values over 10 ‰ ((WHITEHOUSE and KAMBER, 2006), this study) and down to -2 ‰ (ONO et al., 2003). The range of $\Delta^{33}S$ values diminishes at ~2.4 Ga (BEKKER et al., 2004; FARQUHAR et al., 2000; PAPINEAU et al., 2005); (PAPINEAU et al., 2007). The data presented here extend the ranges observed for the 2.4-2.7 Ga time domain and further reinforce pre-existing trends throughout the remainder of the $\Delta^{33}S$ record.

Table 3-1: Source information, age, $\delta^{34}S$, and $\Delta^{33}S$ for new $\Delta^{33}S$ measurements presented in this study

Geologic Unit	Tectonic Unit	Geographic Source	PPRG	AGE	$\delta^{34}S_{(V\text{-}CDT)}$	$\Delta^{33}S_{(V\text{-}CDT)}$	Lithology
upper Motskaya suite, lower Lower Cambrian			29094-7	520	33.46	0.014	Evaporate
upper Motskaya suite, lower Lower Cambrian			29094-15	520	31.76	0.014	Evaporate
upper Motskaya suite, lower Lower Cambrian			29094-19	520	32.34	0.008	Evaporate
pennsylvanian (lower moscovian), Spritzbergen			28836-2	303	15.33	0.012	Evaporate
lower permian (artinskian), Spitsbergen			28834-3	280	13.19	0.015	Evaporate
Manjeri Fm	Belingwe GS Belt	Zimbabwe	PPRG 226	2620	3.39	0.155	Dolomitic black chert
Bulawayan Gp	Bulawayan GS Belt	Zimbabwe	PPRG 251	2640	4.60	2.038	Grey stromatolitic carbonate
Ventersdorp S.Gp	Ventersdorp Basin	Central South Africa	PPRG 291	2640	26.41	0.263	Stromatolitic Limestone
Malmani S. Gp	Transvaal	Central South Africa	PPRG 297	2500	28.00	0.685	Stromatolitic Limestone
Jeerinah Formation	Hamersley Basin	W Australia	PPRG 1970	2650	1.79	1.740	gray carbonate
Gamohaan Farmation	Kaapvaal Craton	Transvaal, S. Africa	PPRG 2512	2500	13.01	10.098	Stromatolitic carbonate
Gamohaan Farmation	Kaapvaal Craton	Transvaal, S. Africa	PPRG 2513	2500	16.84	7.929	Stromatolitic carbonate
Meentheena Carbonate Member	Hamersley Basin	W. Australia	PPRG 2650	2750	2.54	0.566	chert from carbonate member
Meentheena Carbonate Member	Hamersley Basin	W. Australia	PPRG 2652	2750	8.75	0.071	fine grained carbonate
Matinenda Farmation	Penokean Fold Belt	S. Ontario, CA	PPRG1869	2400	4.24	0.099	Siltstone
Insuzi Gp	Wit Mfolozi Inlier	E. South Africa	PPRG- 263	3090	7.97	0.031	Oncolitic dolomite

3.3 Photochemical Model Description

In order to track the photochemical reactions that lead to mass-independent fractionation (MIF) of sulfur, we used a one-dimensional, horizontally-averaged, photochemical model developed by Pavlov et al. (PAVLOV et al., 2001a). The model contains 72 chemical species that are divided into long-lived, short-lived, and well-mixed groups and are inter-connected by 337 chemical reactions. Transport was neglected for short-lived species, and the mixing ratios of extremely long-lived species (*e.g.*, N_2) were held constant. In addition to the 72 chemical species, 3 types of particles were included: sulfate, elemental sulfur, and hydrocarbon aerosols. The equations governing mass continuity and transport were solved over a 100-km vertical grid, divided into 1-km layers. Within each layer, mass balance was maintained, and both eddy and molecular diffusion were included in simulating transport between layers. A modern eddy diffusion profile was assumed (MASSIE and HUNTEN, 1981). The resulting equations were cast in finite difference form, and boundary conditions were applied to each species at the top and bottom of the grid. The reverse Euler method was used to integrate the resulting set of ordinary differential equations to steady state. Fixed mixing ratio boundary conditions for CH_4 and CO_2 were used to generate the different model simulations listed in supplemental info with model results. More details on the photochemical code are given in reference (PAVLOV et al., 2001a).

Previous work shows that S speciation is highly dependent on SO_2 outgassing rate, and that the relative amount of SO_2 and H_2S deposition decreases in favor of S_8

deposition as the SO_2 outgassing rate increases (ONO et al., 2003). We used a SO_2 outgassing rate of $3.5 \cdot 10^8$ molecules $cm^{-2} \cdot s^{-1}$, slightly below estimates of the modern SO_2 flux, $\sim 1 \cdot 10^9$ molecules $cm^{-2} \cdot s^{-1}$ (ARTHUR, 2000; BERRESHEIM and JAESCHKE, 1983; BLUTH et al., 1993; WALKER and BRIMBLECOMBE, 1985). This outgassing rate was chosen because it expressed the greatest degree of $\Delta^{33}S$ preservation in the previous modeling study (ONO et al., 2003).

3.4 Model Results

Previous studies have indicated that the rate of organic haze formation is a function of the atmospheric CH_4/CO_2 ratio (KHARECHA et al., 2005; PAVLOV et al., 2001a; TRAINER et al., 2006). This ratio could have varied during the Archean for a variety of reasons. In the model, the optical depth of the organic haze, which affects the efficiency and rate of SO_2 photolysis, becomes significant at CH_4/CO_2 ratios > ~0.1. Laboratory experiments yield similar results, with measureable aerosol formation for C/O ratios as low as 0.6, or CH_4/CO_2 ratios of 0.2 (TRAINER et al., 2006). We investigated this phenomenon quantitatively by independently varying CH_4 and CO_2 concentrations in a model Archean atmosphere (Figure 3-2). In one set of calculations (panels 'abcd'), the CO_2 concentration was held constant at 1,000 ppmv, while the CH_4 concentration was varied from 10 to 1,000 ppmv. In the other set (panels 'efgh'), CH_4 concentration was held constant at 300 ppmv while CO_2 was varied from 300 to 300,000 ppmv. Both sets of calculations included some simulations in which the effects of haze absorption were neglected. The goal of these calculations was to determine how the production of sulfur

MIF signal varies with atmospheric CH_4/CO_2 ratio. Hence, we also tracked the effect of this ratio on atmospheric sulfur species (panels 'bcfg') and on SO_2 photolysis rates (panels 'dh').

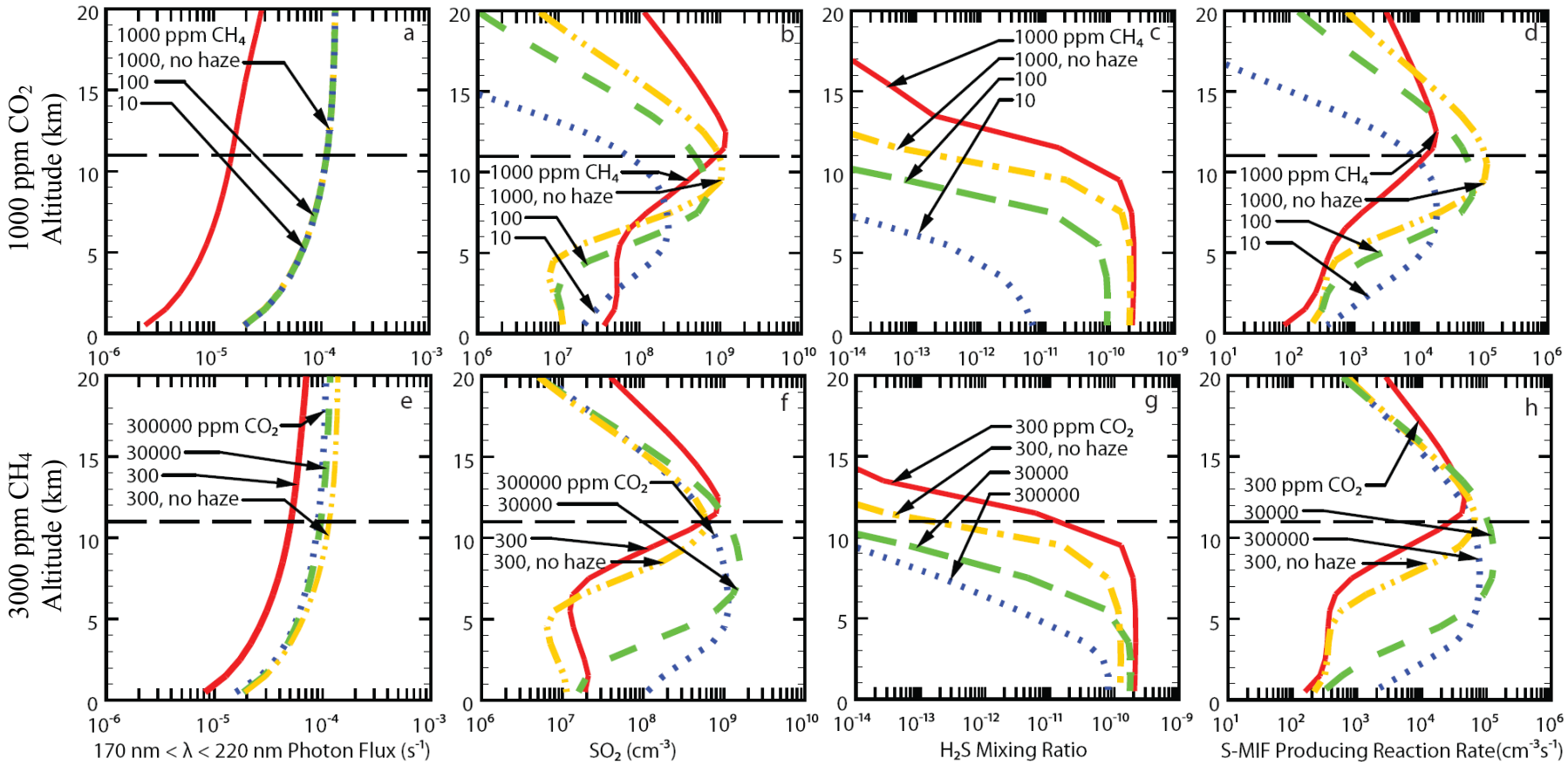

Figure 3-2: Predicted altitude profiles of the flux of photons with 170 nm < λ < 220nm ('a' and 'e'), SO_2 mixing ratio ('b' and 'f'), H_2S mixing ratio ('c' and 'g'), and reaction rate ('d' and 'h') for the photolysis reaction $SO_2 + h\nu$ (λ<220nm) → SO from 1-D photochemical model runs. Panels 'a,' 'b,' 'c,' and 'd' are for models with a constant 1000 ppm CO_2, and panels 'e,' 'f,' 'g,' and 'h' are for models with a constant 300 ppm CH_4. All model simulations assumed 80% of modern day solar insolation, appropriate for the time period around 2.8 Ga. Simulations with 1000 ppm CO_2 had CH_4 concentrations of 1000 ppm (solid line), 100 ppm (dashed line), and 10 ppm (dotted line), while simulations with 300 ppm CH_4 had CO_2 concentrations of 300 ppm (solid line), 30,000 ppm (dashed line), and 300,000 ppm (dotted line).

The effects of varying CH_4/CO_2 on the sulfur chemistry are complex. For CH_4/CO_2 ratios > 0.1, the main effect is to create organic haze, which in turn shields SO_2 from photolysis. This effect is shown explicitly in Figure 3-3a, which shows 0-11 km, column-integrated SO_2 photolysis rates at 175-220 nm as a function of CH_4/CO_2 ratio for the 1000-ppm fixed-CO_2 simulation. We restrict our analysis to photolysis that occurs within the troposphere (below 11 km) because mass-independently fractionated sulfur formed above the tropopause is less likely to make it down to the lower atmosphere where it can be rained out and eventually incorporated into sediments (PAVLOV and KASTING, 2002). Also shown in Figure 3-3a is the 220 nm extinction optical depth of the haze (τ_{220}). It can be seen from the figure that the column-integrated SO_2 photolysis rate begins to decrease just as the haze starts to form and the optical depth increases, at CH_4/CO_2 ratios above ~0.1.

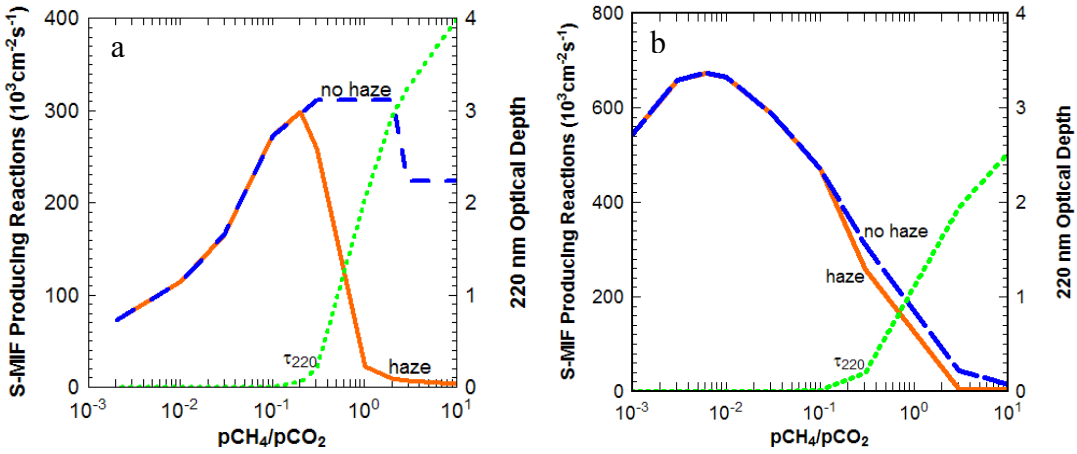

Figure 3-3: Integrated S-MIF reaction rates (dashed line and left y-axis), and 220 nm optical depth (solid line and right y-axis), calculated from SO_2 photolysis rates at wavelengths <220 nm, and plotted against CH_4/CO_2 ratio. In panel 'a', pCO_2 is held constant at 1000 ppm and pCO_2 is varied; in panel 'b', pCH4 is held constant at 300 ppm and pCH_4 is varied. Note the different size on the left y-axis in the two plots.

At lower CH_4/CO_2 ratios (and fixed atmospheric CO_2), column-integrated SO_2 photolysis *increases* with increasing CH_4/CO_2 (Figure 3-3a). The cause of this variation is more subtle. Although sulfur is injected into our model atmosphere entirely as volcanic SO_2, the dominant sulfur species near the surface at most CH_4 levels is H_2S. This H_2S is formed from SO_2 through atmospheric photochemistry and higher surface concentrations of H_2S are predicted for greater CH_4 abundances. Paradoxically, though, higher H_2S concentrations at the surface (Figure 3-2c) lead to higher concentrations of SO_2 in the upper troposphere (Figure 3-2b), and thus to higher rates of tropospheric SO_2 photolysis (Figure 3-2d). The reason for this counterintuitive behavior is that H_2S is much less soluble in rainwater (and ocean water) than is SO_2. (At 25^{o}C, the Henry's Law coefficient for H_2S is 0.141, compared to a value of 2.95 for SO_2.) Sulfur gases are removed from the model atmosphere by rainout and by surface deposition in the oceans, both of which depend on species solubility. So, when H_2S is dominant near the surface, the lifetime of sulfur gases increases, making them more abundant in the atmosphere. In the upper troposphere, H_2S photolyzes to form SO_2, and this is why the integrated SO_2 photolysis rate increases – the higher S-bearing gas abundance leads to a greater amount of SO_2 available for photolysis.

In the fixed CH_4 calculations (Figure 3-3b), the SO_2 photolysis rate *increases* with decreasing CH_4/CO_2 ratio, except at very high CO_2 concentrations (or low CH_4/CO_2). Again, the reason is *not* primarily related to the haze; rather, it is a consequence of feedbacks on the sulfur photochemistry. As CO_2 is increased, *i.e.*, as one moves to the left in Figure 3-3b, H_2S is converted to SO_2 by photochemistry. This causes

the integrated SO_2 photolysis rate to peak at high pCO_2, or low CH_4/CO_2. Unlike the fixed-CO_2 case (Figure 3-3a), the total abundance of H_2S near the surface does not vary greatly in these simulations because the concentration of CH_4 is not varying. Hence, the solubility feedback described above is less important.

The results of this complex interplay of methane and sulfur photochemistry are best shown as a plot in 2-dimensional CO_2-CH_4 space. In Figure 3-4, we have plotted the rate of S-MIF-producing reactions, *i.e.*, integrated tropospheric SO_2 photolysis, as contours in $\log(pCH_4)$ and $\log(pCO_2)$. The highest SO_2 photolysis rates, shown in hot colors in Figure 3-4, are predicted at $pCH_4 \sim 0.001$ bar and $pCO_2 \sim 0.1$ bar, corresponding to a CH_4/CO_2 ratio of ~0.01. At lower CH_4/CO_2 ratios (found by moving down and to the right from the maximum), the SO_2 available for photolysis decreases, whereas at higher ratios (found by moving up and to the left from the maximum) shielding of solar UV by organic haze becomes important. Runaway glaciations may by triggered when $CH_4 \geq CO_2$ (PAVLOV et al., 2001a). In Figure 3-4, this region is represented by a diagonally striped triangle and may be considered physically inaccessible. Fortunately, the transitions we predict here can explain variations in the S-MIF record without entering into areas of the graph associated with catastrophic anti-greenhouse effects.

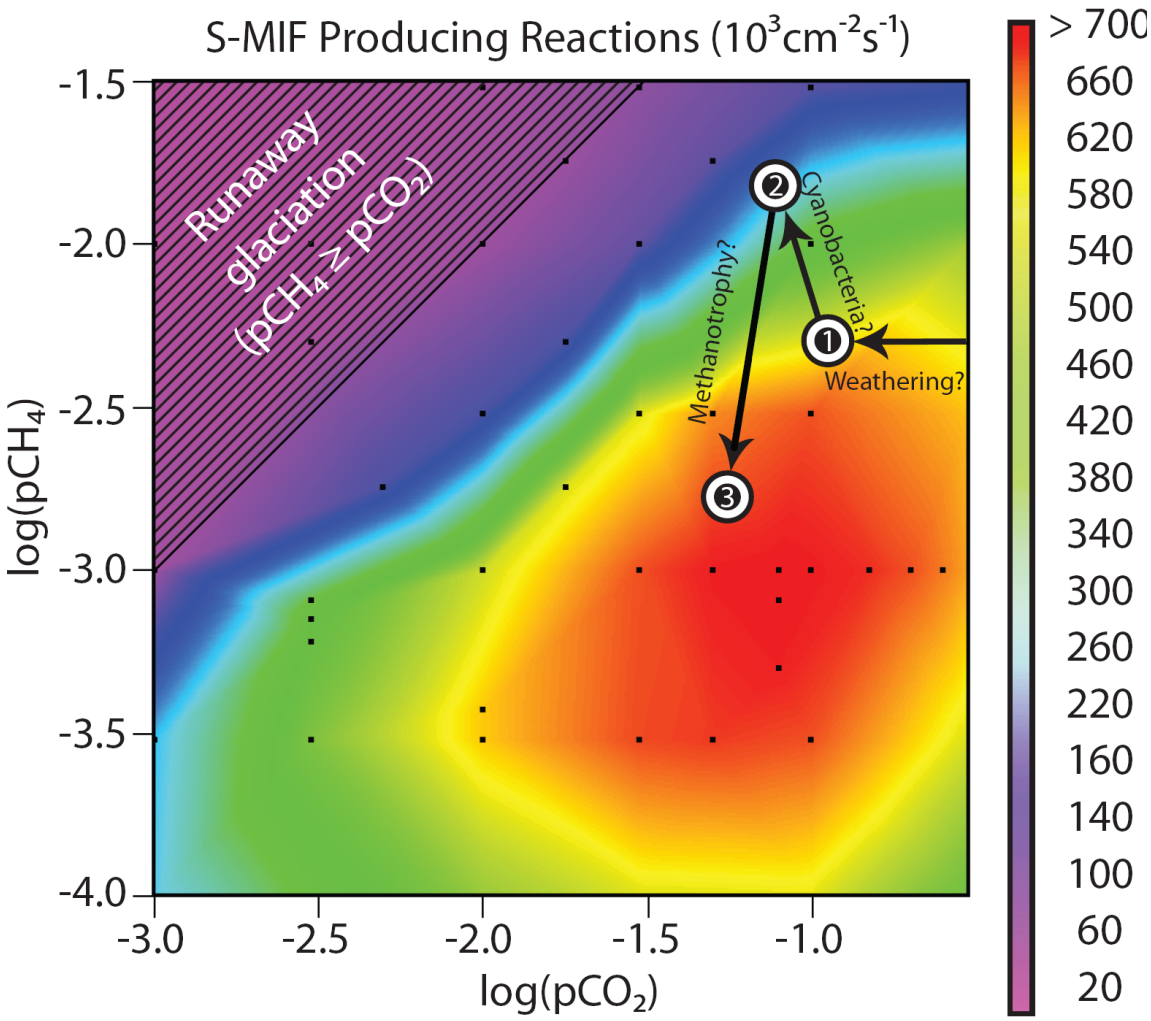

Figure 3-4: Contour plot showing tropospheric S-MIF production as a function of log(pCO_2) and log(pCH_4) (both in bars). Individual model simulations are shown as black squares. Hot colors indicate high tropospheric SO_2 photolysis rates at wavelengths in the range 175-220 nm; this is an estimate of the rate of S-MIF production. The region with diagonal lines is an area of the graph where $CH_4 \geq CO_2$, a condition for which a strong anti-greenhouse effect will likely result from the formation of a thick organic haze. Thus, this region of the figure should lead to unstable climate and the presence of snowball Earth conditions. Numbered bull's-eyes on this plot indicate the CH_4 and CO_2 concentrations at various points in the Archean according to the atmospheric evolution proposed in Section 5.3, with (1) indicating prior to ~3.2 Ga, (2) indicating ~3.2 - ~2.7 Ga, and (3) indicating ~2.7 - ~2.45 Ga. The arrows between these circles represent changes to the atmospheric composition, driven by the process written next to/under each arrow.

3.5 Discussion

3.5.1 Proposed timeline for the evolution of Archean climate, atmospheric chemistry, and biology

The synthesis of the model predictions (Figure 3-4) and the sulfur isotope record (Figure 3-1), suggests a complex evolutionary sequence for atmospheric composition and climate during the first half of the Earth's history. We offer the following speculative sequence of events, recognizing that it may not provide a unique explanation for the data. Prior to ~3.5 Ga, CH_4 concentrations were relatively low ($pCH_4 << pCO_2$), and CO_2 was the main greenhouse gas countering low solar luminosity. These conditions allowed for the production of a significant nonzero $\Delta^{33}S$ and $\Delta^{36}S$ signal. At some point during this period, methanogens evolved, and atmospheric CH_4 started to increase. The early evolution of methanogens is consistent both with recent geologic evidence (UENO et al., 2006), the predictions of molecular clocks (BATTISTUZZI et al., 2004), and with at least some models of the origin of the genetic code (XUE et al., 2003). The additional warming produced by CH_4, combined with rapid continental growth during this time (TAYLOR and MCLENNAN, 1995), should have resulted in increased weathering, causing atmospheric CO_2 concentrations to decline. This gradual change in CO_2 is represented in Figure 3-4 by the arrow pointing directly to the left.

This haze-free atmosphere would have been significantly altered by the advent of oxygenic photosynthesis. Evidence for the appearance of oxygenic photosynthesis by ~2.78 Ga is provided by the presence of 2-α methyl hopanes (from cyanobacterial cell wall lipids) (BROCKS et al., 1999) and sterols (from O_2-requiring eukaryotes) (SUMMONS

et al., 1999) in sediments dated at 2.78 Ga old (BROCKS et al., 2003). Once oxygenic photosynthesis arose, extra organic material would have been made available to fermentation and methanogenesis, and the CH_4 flux to the atmosphere should have increased (CATLING et al., 2001) driving CH_4/CO_2 levels high enough to form a thick haze. This transition is indicated by an arrow pointing upwards and slightly to the left in Figure 3-4.

The presence of the haze would have caused the sulfur $\Delta^{33}S$ signal to become small and could have led directly to glaciation, by creating a strong anti-greenhouse effect. But the climate system should have been stabilized by the development of a negative feedback cycle. Further increases in CH_4 would have thickened the haze, resulting in cooler temperatures and more severe glaciations that would have limited biological productivity. Because the source of the CH_4 was primarily biological, this decrease in productivity should have led to decreased CH_4 fluxes to the atmosphere, thereby reducing the optical depth of the haze.

The negative feedback loop described above can be described graphically by a diagram similar to that employed in Lovelock's Daisyworld hypothesis (WATSON and LOVELOCK, 1983). (We are indebted to W. Moore for pointing this out some time ago following a seminar at UCLA.) In Daisyworld, white (or black) daisies exhibit parabolic growth curves with respect to surface temperature, while surface temperature responds negatively (or positively) to increases in white (or black) daisy cover. Our system behaves in much the same way, although the axes of the plot are reversed (Figure 3-5). In our model, surface temperature, T_s, exhibits a roughly parabolic response to atmospheric CH_4/CO_2 ratio, R. At low ratios, T_s increases with R because of the greenhouse effect of

CH_4. At high ratios, T_s decreases with R because haze begins to form, and this creates an anti-greenhouse effect.

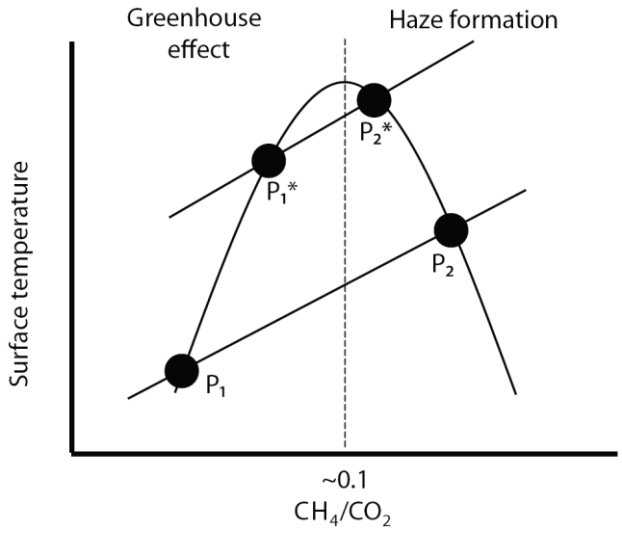

Figure 3-5: Diagram of proposed stable feedbacks for the Archean. The curved line illustrates the effect CH_4/CO_2 has on surface temperature, and the straight lines illustrate the effects of temperature on CH_4/CO_2 before (P_1-P_2) and after (P_1*-P_2*) the rise of methanotrophy. In both cases, increases in temperature should have caused increased biological productivity and higher CH_4 fluxes. At CH_4/CO_2 > ~0.1, the anti-greenhouse effect is stronger than the greenhouse effect and increases in the CH_4 flux should have caused cooling. Thus, P_2 and P_2* are stable and the system would have settled into a state with an organic haze. The difference between the two stable points is that increased methanotrophy at ~2.7 Ga would have lowered the net biological CH_4 flux, leading to a stable equilibrium point (P_2*) associated with lower CH_4/CO_2 and higher T.

The other half of the feedback loop is the dependence of CH_4 production on surface temperature. For the pre-2.7-Ga world described above, CH_4 would have been produced either directly from methanogens utilizing CO_2 and H_2, or indirectly from photosynthesis followed by fermentation and methanogenesis {Kharecha, 2005 #289}. In either case, CH_4 production should have increased with increasing T_s, particularly at surface temperatures near the freezing point of seawater (because the photosynthetic

biota would have died if the oceans had frozen over). The resulting system is described by Figure 3-5. The stable equilibrium point in this system, where the slopes of the two curves are opposite, is at point P_2. (Point P_1 is unstable because the two curves both have positive slopes.) This implies that the system should have stabilized in the region where a thick organic haze was present. In our model, this corresponds to the time period prior to 2.7 Ga, when the sulfur MIF signal was small, or nearly absent. We suggest that the glaciations at 2.9 Ga occurred at the time of the highest atmospheric CH_4/CO_2 ratio and the thickest organic haze. Indeed, as we do not know the time scale for the duration of the glaciations, they might not represent a stable situation at all, but merely a transient overshoot in haze thickness caused by the advent of oxygenic photosynthesis.

If the above hypothesis is correct, the end of this glacial, low $\Delta^{33}S$ period at ~2.7 Ga, should have been caused by a decrease in atmospheric CH_4/CO_2 ratio and an accompanying decrease in haze thickness. Several different factors could have contributed to such a decrease. The most straightforward of these is that atmospheric CO_2 concentrations should have increased when the climate got cold, because weathering would have slowed. Perhaps a stable equilibrium was only achieved after this rebound occurred. Alternatively, the decrease in CH_4/CO_2 ratio could have been a consequence of an increase in methanotrophy, either aerobic or anaerobic. The evolution of methanotrophs at this time is consistent with the abundant, extremely ^{13}C-depleted kerogens in sediments from several different localities around the world dated at between 2.6 and 2.8 Ga old (SCHIDLOWSKI et al., 1983). These kerogens suggest that organic carbon was being doubly fractionated, either by aerobic methanotrophs (HAYES, 1983; HAYES, 1994) or by anaerobic methane oxidizers that live in consortia with sulfate-

reducing bacteria (HINRICHS, 2001). In either case, the fact that some CH_4 was being lost by reaction with O_2 or sulfate within the water column could have led to a reduction in the methane flux to the atmosphere (PAVLOV et al., 2003).

If this reasoning is correct, the feedback loop described for the pre-2.7 Ga biosphere would have remained in operation, but the equilibrium point would have shifted towards lower CH_4 concentrations and a thinner organic haze (point P_2* in Figure 3-5). In our model, this corresponds to the high-MIF region of Figure 3-1 between 2.45 and 2.7 Ga. An atmosphere with fCH_4 ~0.03, and fCO_2 ~ 0.05 would be consistent with low S-MIF production (Figure 3-4) and a surface temperature high enough to avoid glaciations (T_s ~ 294, HAQQ-MISRA et al., submitted).

3.5.2 Uncertainties in the Calculations

The major sources of error in determining the composition of the atmosphere and the resulting flux of UV photons to the stratosphere have been discussed previously (PAVLOV et al., 2001a). These include limiting the tholin chemistry to molecules shorter than C_6 compounds, a monodisperse size distribution for haze particles (one size at each altitude), the use of an eddy diffusion constant derived for a more vigorously mixed, haze-free atmosphere, and the assumption that hydrogen escape was diffusion-limited (TIAN et al., 2005). While variations in any of these assumptions might well change the precise numerical predictions of our model, they should not alter our fundamental hypothesis, which is that changes in atmospheric chemistry, as reflected in the sulfur MIF record, also affected Archean climate.

As mentioned earlier, in order to preserve a sulfur MIF signal, it is also necessary that sulfur gases exit the atmosphere in different chemical forms, so that species with different MIF signals will be preserved in different sedimentary environments (PAVLOV and KASTING, 2002; ZAHNLE et al., 2006). To see whether that requirement is satisfied in our model, we plotted column-integrated SO_2 photolysis (our specified MIF indicator) and sulfur speciation near the surface against atmospheric CH_4/CO_2 (Figure 3-6). Fortunately, the two MIF indicators are in reasonable agreement. The S-MIF production rate tends to be highest at CH_4/CO_2 values for which the distribution of the sulfur species is not dominated by a single species, regardless of whether CH_4 or CO_2 is varied to change the haze optical depth. Hence, the large S-MIF signal that is created in the atmosphere when an optically thin haze is present should stand a good chance of being incorporated into sediments; production and preservation of S-MIF appear to follow similar trends. That said, our sulfur gas speciation is different from the distribution found by Zahnle et al. (2006). Those authors suggested that the important competition was between oxidized sulfur species (SO_2 and H_2SO_4) and S_8. In our model, S_8 is never highly abundant, probably because of the modest sulfur outgassing rate that was assumed, and the competition is between SO_2, H_2SO_4, and H_2S. However, preservation of our signal should not be an issue, as the same outgassing rates were shown by Pavlov et al. (ONO et al., 2003) to lead to a high degree of S-MIF preservation.

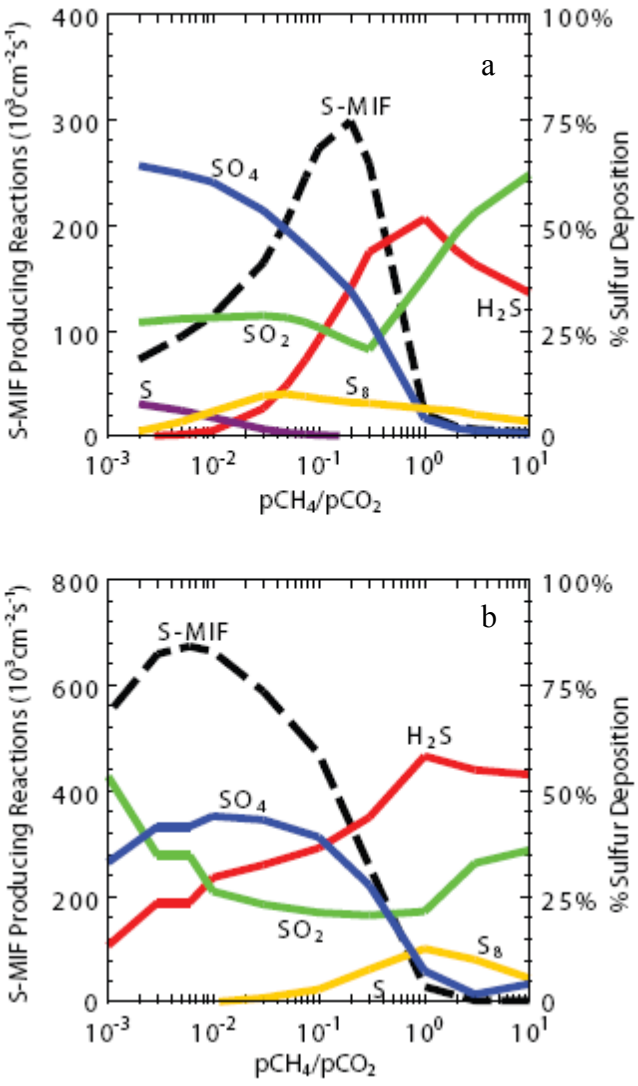

Figure 3-6: Model predictions of tropospheric SO_2 photolysis rates for wavelengths shorter than 220 nm (dashed line), and deposition rates of various sulfur species (solid lines) as a function of CH_4/CO_2 ratio. In panel 'a', pCO_2 is held constant at 1000 ppm and pCH_4 is varied; in panel 'b', pCH_4 is held constant at 300 ppm and pCO_2 is varied. Note the different size on the left y-axis in the two plots.

3.5.3 Uncertainties in the pattern of Mid-Archean sulfur isotope excursions

Our hypothesis for the correlation between sulfur-MIF signal and climate during the Archean is based on the assumption that the observed temporal changes in $\Delta^{33}S$ are real, and are not strongly biased by sampling statistics. Particularly important is the question of whether the low-MIF values observed during the Mid-Archean (2.7-3.2 Ga) are representative of low-MIF values globally throughout this time period. To this point, five stratigraphic intervals located in South Africa and western Australia have been sampled in this interval (data from (FARQUHAR et al., 2000; OHMOTO et al., 2006; ONO et al., 2006a; PETERS et al., 2006), and the range of observed $\Delta^{33}S$ values is 1.08‰. While we believe that this range will expand with further research, we also interpret the attenuation of the $\Delta^{33}S$ signal as a real effect. Additional work is planned to collect data and to evaluate whether there are systematic changes in the correlations between the $\delta^{34}S$, $\Delta^{33}S$, and $\Delta^{36}S$. Thus, our organic haze hypothesis could change in the future as additional data analyses are performed. For the moment, the organic haze hypothesis appears to be the best way to interpret the existing data.

3.5.4 Uncertainties in the pattern of Mid-Archean sulfur isotope excursions

Three alternative explanations for the low S-MIF values observed during the Mid-Archean have been recently offered by Ohmoto et al. (2006). The first two of these presume that atmospheric O_2 concentrations were high throughout the Archean, as they are today. In one hypothesis, all large $\Delta^{33}S$ values are attributed to explosive volcanic

events that injected sulfur-bearing gases high into the atmosphere where mass-independent photochemical reactions would be produced. Reasons for discounting this idea have been discussed previously by (FARQUHAR et al., 2001). Explosive volcanism is not restricted to the Archean, nor is it the primary way that volcanogenic sulfur-bearing gases are introduced to the atmosphere (c.f., (BLUTH et al., 1993; GRAF et al., 1997). In the second hypothesis, thermochemical reduction reactions involving amino acids are invoked to produce the observed $\Delta^{33}S$ values (WATANABE et al., 2006). While this mechanism may be capable of producing nonzero $\Delta^{33}S$ values, it has not been demonstrated that this process can reproduce the observed $\Delta^{36}S/\Delta^{33}S$ (c.f, FARQUHAR and WING, 2003), the large range of $\Delta^{33}S$ values observed in the Archean record, or the volume of sulfur observed with MIF. Furthermore, neither of these first two mechanisms can be reconciled with the drastic decrease in $\Delta^{33}S$ values at ~ 2.4 Ga.

The third hypothesis offered by Ohmoto et al. (2006) is the "yo-yo atmosphere," mentioned in Section 1. In this model, atmospheric O_2 concentrations increased for the first time at 3.2 Ga, then decreased at ~2.7 Ga, and then increased once again at ~2.4 Ga. This model could thus account for both the attenuation of the $\Delta^{33}S$ signal and the glaciation at ~2.9 Ga (through destruction of a methane greenhouse). However, this scenario may be in conflict with other geological constraints. Most notably, the Witwatersrand basin (~2.9 Ga) contains abundant detrital pyrite and uraninite (HOLLAND, 1984), which are taken by most workers as evidence for low atmospheric O_2. (See Phillips et al. (2001) for a different opinion.) When combined with additional evidence from paleosols, the uraninite data suggest an upper limit of $\sim 10^{-2}$ atm, or 0.05 PAL, for

pO_2 at this time (HOLLAND, 1984). This is substantially higher than the minimum amount of O_2 needed to affect $\Delta^{33}S$ preservation (~10^{-5} PAL (PAVLOV and KASTING, 2002)). Hence, atmospheric O_2 concentrations in the range between 10^{-5} to $10^{-1.3}$ PAL could, in principle, explain the attenuated $\Delta^{33}S$ values between 2.7 and 3.2 Ga. Furthermore, the nonlinear chemical interactions between O_2 and CH_4 (CLAIRE et al., 2006; GOLDBLATT et al., 2006; ZAHNLE et al., 2006) provide a mechanism for causing atmospheric O_2 to fluctuate between low and high concentrations, as they would have needed to do if this hypothesis is correct (KASTING, 2006).

When one examines the yo-yo hypothesis in more detail, however, it is difficult to make it work. First, the quoted upper limit on pO_2 based on uraninite survival is just that – an upper limit. It assumes that pCO_2 was < 10 PAL and that the kinetics of uraninite dissolution are maximally slow. For a more plausible pCO_2 value of 100 PAL (near the upper limit quoted by Rye et al. (1995) yet strong enough to prevent glaciation according to HAQQ-MISRA et al., submitted), and less conservative assumptions about the kinetics of uraninite dissolution, the upper limit on pO_2 drops to $10^{-3.5}$ atm, or ~10^{-3} PAL (HOLLAND, 1984). This value is below the stable "high-O_2" levels predicted by photochemical models (GOLDBLATT et al., 2006; ZAHNLE et al., 2006). In other words, when O_2 jumps to its stable upper state, its predicted concentration may exceed the value that is consistent with uraninite survival. One can, as just pointed out, still make the mechanism work by making favorable assumptions about atmospheric CO_2 levels and uraninite stability, but under more plausible assumptions the mechanism would fail.

The yo-yo model must also explain why atmospheric O_2 concentrations decreased again at ~2.7 Ga and stayed low until 2.4 Ga, as indicated by the very large range of $\Delta^{33}S$ values observed in Late Archean sediments. Small increases in reductant input could conceivably do this (GOLDBLATT et al., 2006), but why would such an increase be sustained for hundreds of millions of years when the secular trend in reductant input was presumably in the opposite direction? It seems more likely that the yo-yo model applies to a much shorter time period spanning the transition from low O_2 to high O_2. It might, for example, explain why three separate pulses of glaciation are seen in the Huronian sequence, around 2.2-2.45 Ga (Roscoe, 1973). Perhaps O_2 and CH_4 were both oscillating during this time period. But the sulfur MIF pattern over the Mid- to Late-Archean is better explained by the organic haze model proposed here.

One final problem with the yo-yo explanation is that it treats the structure of the Archean $\Delta^{33}S$ record as tracking the "on," or "off" switch of MIF chemistry and preservation, whereas the data suggest that it may be more appropriate to interpret the record as emblematic of a $\Delta^{33}S$ production "dial." Using $\Delta^{33}S$ alone to determine the presence/absence of MIF does not take into account important information about the production of the observed $\Delta^{33}S$ effect that is captured in $\delta^{34}S$ (and also $\Delta^{36}S$). The general consistency between $\delta^{34}S$ and $\Delta^{33}S$ of Archean sulfides (Figure 3-7) suggests that variation in the absolute magnitude of $\Delta^{33}S$ may be the result of changes to the amount of $\Delta^{33}S$ being produced, not a binary control on the presence/absence of a MIF signal (*i.e.* simple mixing of a MIF and mass-dependently fractionated pool). We see that data from the 2.7-3.2 Ga period fit more closely with the MIF array produced by other Archean

data, regardless of their smaller $\Delta^{33}S$ values. Furthermore, the mid-Archean $\delta^{34}S$ are dissimilar to that observed at 2.4 Ga. Samples deposited after the rise of oxygen exhibit a significant range of $\delta^{34}S$ values (BEKKER et al., 2004; JOHNSTON et al., 2005); this spread has been attributed to microbial sulfate reduction in marine environments with seawater sulfate concentrations greater than 200 micromolar (HABICHT et al., 2002). If atmospheric oxygen were to have risen between 2.7 and 3.2 (as is called upon in the yo-yo hypothesis), a $\delta^{34}S$ fractionation increase should also be observed, which it is not. Similar to the information that can be gained by interpreting $\Delta^{33}S$ in the context of the $\delta^{34}S$, we can also incorporate information from $\Delta^{36}S$. Most recently, arguments based on the relationship between $\Delta^{33}S$ and $\Delta^{36}S$ have been presented for the presence of active MIF chemistry and preservation at 2.9 Ga (ONO et al., 2006b). Our results raise the possibility that the persistence of low atmospheric O_2 concentrations throughout the mid-Archean, coupled with a changing role for organic haze, may have led to small-scale changes in the specific photochemical reactions that are responsible for the production of the MIF signature. If true, this study points to the importance of both more detailed characterization of the Archean sulfur isotope record and further photochemical experiments.

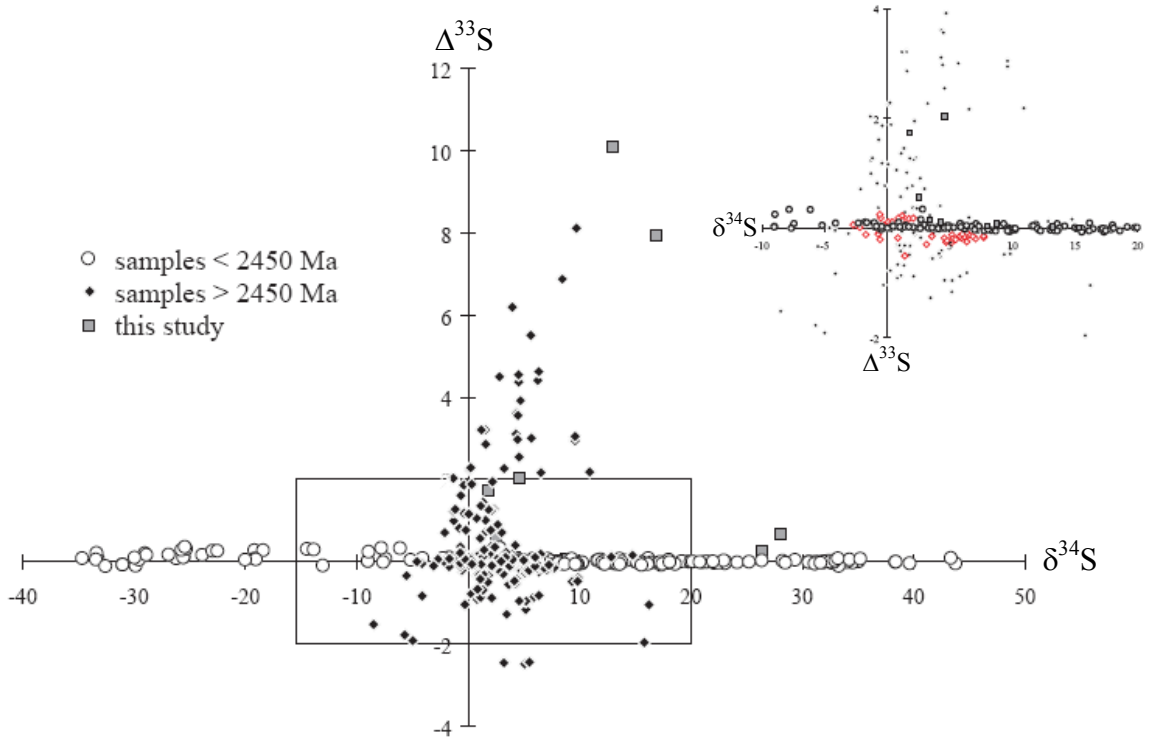

Figure 3-7: A triple isotope plot of $\delta^{34}S$ versus $\Delta^{33}S$, highlighting the variability between 2700 Ma and 3100 Ma. Samples younger than 2.45 Ga are shown by unfilled circles. Samples from this study (all of which are older than 2.45 Ga) are shown with solid squares. The other samples with ages greater than 2.45 Ga are shown by filled diamonds. The inset zooms in on the area between -15 and +20 $\delta^{33}S$ and between -2 and +2‰ $\Delta^{33}S$, with samples from between 2700-3100 Ma shown by unfilled diamonds.

3.5 Conclusions

Temporal variations in the concentrations of atmospheric CH_4 and CO_2 during the Archean could have significantly affected the thickness of organic haze, in turn triggering a rearrangement of climate and photochemistry. The importance of biology to global CH_4 and CO_2 fluxes is already well established, as is the importance of climate for the stability of surface life. If our model is correct, atmospheric composition, haze thickness, and

climate during were strongly modulated by life the Archean/early Paleoproterozoic Eons. Because biology would have been a critical component in the negative feedback cycles proposed here, one can think of this as a "Gaian" control system (LOVELOCK, 1988), supporting the hypothesis that life is capable of unconsciously tailoring and influencing its environment on all scales (from local to global). Strong coupling between atmospheric sulfur chemistry and CH_4/CO_2 ratios occurred because biogenic methane was a major Archean greenhouse gas, comparable in importance to CO_2 and H_2O. In our view, CH_4 was also a key player in Archean biogeochemical cycles and in the atmospheric redox budget. Further studies of both S and C isotopes, coupled with tighter correlations with other geologic evidence, are needed to test whether the hypothesis proposed here is correct. In particular, an improved understanding of the wavelength dependence of $\Delta^{33}S$ and $\Delta^{36}S$ production will allow for more detailed models of Archean S-MIF production, while finer scale temporal analyses of Archean $\Delta^{33}S$ and $\Delta^{36}S$ will help clarify the trends upon which much of our hypothesis is based.

CHAPTER 4

Climatic Implications of Archean Hydrocarbon Chemistry

Abstract:

Previous models of anoxic Archean-like atmospheres demonstrate how increased concentrations of methane (CH_4) and carbon dioxide (CO_2) could have kept the Earth's oceans from freezing over despite the presence of a fainter Sun at the time. Internal calculations show these previous models are inaccurate, as they overestimate the greenhouse forcing of CH_4. When the system is modeled properly, it is difficult to explain the climatic history of the Earth based solely on the direct climatic forcings of CH_4, CO_2, and H_2O. Fortunately, increased CH_4 concentrations could have led to increased concentrations of three extremely efficient greenhouse gases - ethylene (C_2H_4), ethane (C_2H_6), and propane (C_3H_8). The warming imparted by increased hydrocarbon gases in the atmosphere was likely limited by the anti-greenhouse effects of hydrocarbon particles that also increase as CH_4 increases. This leads to a critical question: what is the net climatic forcing from hydrocarbons expected for an anoxic atmosphere? This chapter contains the results of a 1-D photochemical model I employed to predict C_2H_4, C_2H_6, C_3H_8, and haze optical depths in an anoxic atmosphere. These predictions can be used as inputs for Archean climate calculations. The implications of this project are threefold: 1.) the Archean climate would have required greenhouse gases other than H_2O, CO_2, and CH_4 to keep liquid water stable at the Earth's surface; 2.) the presence of C_2H_6 could have allowed the climate to stabilize above the freezing point; and 3.) the climate may

have been stable over a narrow range of CH_4 concentrations and created Gaian-like feedback loops.

4.1 Introduction

Increasing our knowledge of the evolution of Earth's atmosphere and climate will augment the information we have on the early evolution of life on Earth and diversify the types of biospheres that we can search for on extrasolar planets. Much of the research on the Earth's early climate has focused on offsetting expected changes to solar luminosity. Because main sequence stars like the Sun brighten predictably as they age, researchers have been able to extrapolate backwards in time to estimate the history of Earth's incoming radiation budget (NEWMAN and ROOD, 1977). As a result of these efforts, we know that for much of Earth's history water would not have been stable at the Earth's surface if its atmosphere had the same composition that it does today (KASTING, 1993). Contrary to this expectation, geochemists have found evidence for liquid oceans as early as 4.3 billion years ago (Ga) (MOJZSIS et al., 2001). Furthermore, the lack of glacial deposits prior to 2.9 Ga is consistent with warm global temperatures, although this may be due to a lack of adequate number of Archean samples. The Earth's O isotope record is commonly interpreted as being consistent with global average temperatures over 50ºC prior to 3.0 Ga (KNAUTH and LOWE, 2003), although the O isotope interpretation is disputed (KASTING and HOWARD, 2006; KASTING et al., 2006)). We can conclude that for at least half of Earth's history a significant positive climatic forcing must have countered the lower solar luminosity at the time.

Most solutions to this "faint young sun paradox" involve an increase in various greenhouse gases, all of which have proven to be inadequate. Past models proposed the faint young sun paradox can be solved if there were increased concentrations of carbon dioxide (CO_2) (OHMOTO et al., 2004; WALKER et al., 1981), ammonia (NH_3) (SAGAN and CHYBA, 1997), or methane (CH_4) (PAVLOV et al., 2001a). Limits to the amount of warming possible from increased CO_2 concentrations come from paleosol data (RYE et al., 1995; SHELDON, 2006). The warming potential of NH_3 would have been severely limited by the increased photolysis that would have occurred given the lack of a global ozone layer (PAVLOV et al., 2001a); O_3 concentrations are heavily dependent on O_2 concentrations and there is abundant evidence indicating that the Earth's atmosphere was anoxic prior to ~2.45 Ga (HOLLAND, 1984). Conversely, the low O_2 concentrations would have led to higher CH_4 levels because the greatest sink of CH_4 in the modern atmosphere, oxidation, would have been much smaller in an anoxic atmosphere. Following this line of thought, the work of Pavlov et al. (2000) showed that the Earth could have been sufficiently warmed by increased CH_4 and CO_2. Later work (PAVLOV et al., 2001a) demonstrated the limitation on warming from CH_4 is the anti-greenhouse effect created by a tholin haze. As the CH_4/CO_2 ratio in the atmosphere increases, so does the abundance of particulate organic material that absorbs and re-radiates incoming solar radiation, thereby causing an anti-greenhouse effect (MCKAY et al., 1991). Unfortunately, internal calculations (J. Haqq-Misra, pers. comm.) show that these models incorrectly treat CH_4 absorption, leading to significant overestimations of surface temperature. Given the limitations on CH_4/CO_2 ratio from tholin haze chemistry, the limits on CO_2 from paleosol data, and the limits on NH_3 from photolysis rates, present models cannot keep

explain the warm temperatures thought to be present during the Archean without additional forcings.

Here we propose three previously unconsidered greenhouse gases - C_2H_2, C_2H_6, and C_3H_8 - as part of the solution to the faint young sun paradox. These gaseous hydrocarbon species should increase in concentration as CH_4 increases, amplifying the effects CH_4 has on climate. On the other hand, hydrocarbon particles will increase in concentration as CH_4 increases, creating an anti-greenhouse effect that mitigates the effects CH_4 has on climate. In order to discover the CH_4 concentrations for which hydrocarbons enhance the climatic effects of CH_4, I used a 1-D photochemical model of an anoxic atmosphere to predict the concentration of C_2H2, C_2H_6, and C_3H_8, and the contributions of organic haze particles to the optical depth of the atmosphere.

4.2 Methods

We used a one-dimensional, horizontally-averaged, photochemical model developed by Pavlov et al. (2001a) to model atmospheric hydrocarbon chemistry in the Archean. Mass continuity and transport equations were solved over a 100-km vertical grid, divided into 1-km layers. The model contains 72 chemical species, inter-connected by 337 chemical reactions and divided into long-lived, short-lived, and well-mixed groups. Transport was neglected for short-lived species, and the mixing ratios of well-mixed species (e.g., N_2) were held constant. C_2H_4, C_2H_6, and C_3H_8 were all treated as long-lived species. Mass balance was maintained within each layer and transport between layers was calculated from both molecular and eddy diffusion, employing a modern eddy

diffusion profile (MASSIE and HUNTEN, 1981). Boundary conditions were applied to each species at the top and bottom of the grid and the reverse Euler method was used to integrate the resulting set of ordinary differential equations to steady state. We used fixed mixing ratio as the lower boundary condition for CH_4 and CO_2, varying these values between runs to predict the dependence of hydrocarbon chemistry on these two species. More details on the photochemical code are provided in a technical paper by Pavlov et al. (2001a).

Three types of aerosols were also included: sulfate, elemental sulfur, and hydrocarbon. Aerosol droplets were assigned a single size for each grid layer (i.e., a monodisperse size distribution). The particle radius in a given layer was calculated by comparing coagulation and removal lifetimes and allowing particles to grow if the former was greater than the latter. The result of this treatment is growth of particles during freefall through the denser layers of the atmosphere.

Hydrocarbon aerosols formed via immediate, irreversible condensation of C_4H_2 and C_5H_4. This may overestimate the rate of particle formation because it is thought that longer carbon chains are the precursors to particle formation and because we ignore any back reactions that may impede particle growth. Because haze leads to cooling of the surface, an overestimation of its formation rate should be considered a conservative approach to our hypothesis that hydrocarbons species could have contributed to the warm paleotemperatures prior to 3.0 Ga.

4.3 Results

4.3.1 Hydrocarbon Concentrations

We ran the photochemical code for a variety of CH_4 and CO_2 concentrations; the resulting predictions of C_2H_4, C_2H_6, and C_3H_8 concentrations are depicted in Figure 4-1. The logarithm of the surface mixing ratios of C_2H_4, C_2H_6, and C_3H_8 are plotted as a function of log(pCH_4) and log(pCO_2) in Figure **4-1**, and the same general patterns are expressed by the three gases. The concentrations of the hydrocarbons increase by several orders of magnitude as CH_4 rises. Trends in hydrocarbon mixing ratio for changes in CO_2 mixing ratio are significant but smaller in size and less consistent than those caused by variations of CH_4. This makes sense from a chemical standpoint: photolysis of CH_4 is the main source of organics in the atmosphere, so changes to CH_4 concentration should have a large impact on atmospheric organic chemistry. Secondary changes may also arise from changes to CO_2, but the relationship can be positive or negative depending on whether the addition of carbon or oxidants is more important for a particular atmospheric composition.

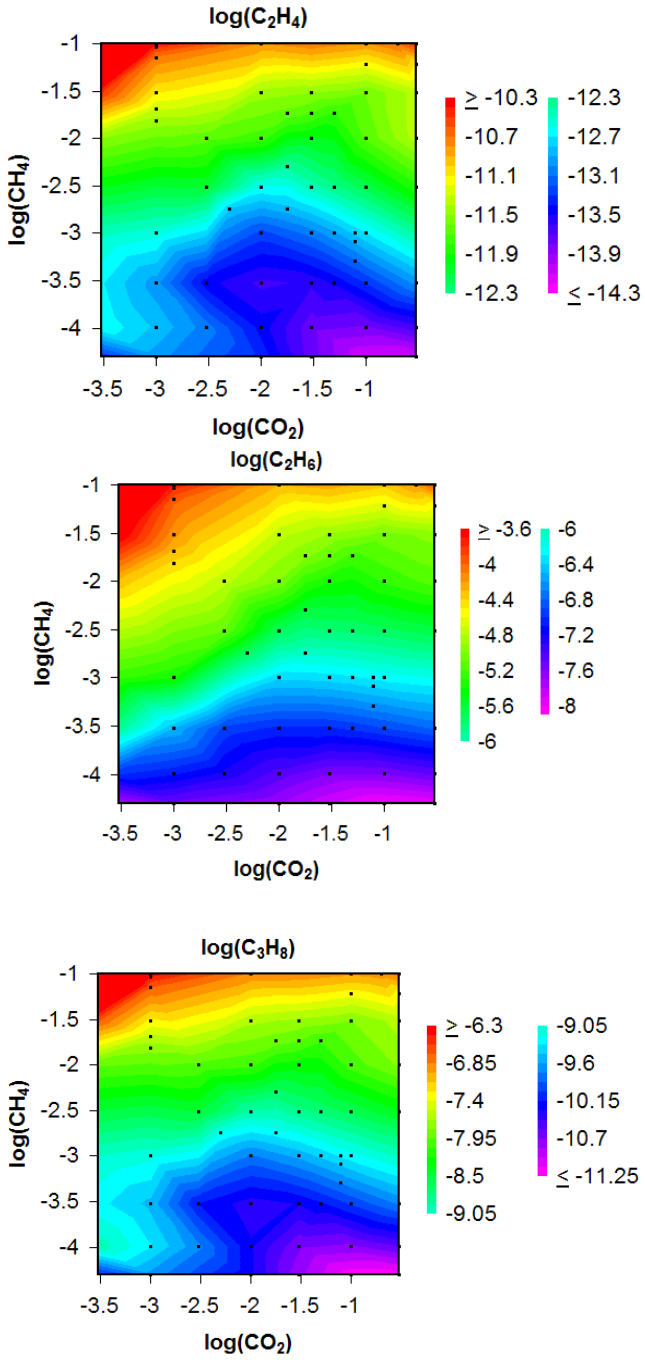

Figure 4-1: Contours of log(pC_2H_4) (top left), log(pC_2H_6) (top right), and log(pC_3H_8) (bottom) plotted as a function of log(pCO_2) (x-axis) and log(pCH_4) (y-axis). Values are those predicted for the surface layer of model atmospheres. Black dots indicate individual model runs.

C_2H_4, which is not well-mixed in these models, has the lowest concentrations of the three species studied and shows the smallest variations in abundance. The lowest pC_2H_4, 10^{-14}, is predicted for $pCO_2 > 10^{-1}$ and $pCH4 < 10^{-4}$. The highest concentrations, nearing 10^{-10}, are predicted for $pCH_4 > 10^{-1.5}$ and $pCO_2 < 10^{-3}$. A local minimum in pC_2H_4 is found for $pCH_4 \sim 10^{-3.5}$ and $pCO_2 = 10^{-2}$, but this may be an artifact of low grid density, as it is based on a single datum point. At high CH_4 concentrations, there is a slight increase in pC_2H_4 as CO_2 decreases. None of these trends are as significant as the positive relationship between pCH_4 and pC_2H_4, which accounts for almost all the variation seen in the parameter space explored.

The variations in pC_3H_8 are greater that those in pC_2H_4, and higher concentrations of pC_3H_8 are predicted, but otherwise general trends in predictions of pC_3H_8 mirror those for pC_2H_4. Mixing ratios vary from $pC_3H_8 \sim 10^{-11}$ for $pCO_2 = 10^{-1}$ and $pCH_4 \sim 10^{-4.3}$ to $pC_3H_8 \sim 10^{-6}$ for $pCO_2 = 10^{-3.5}$ and $pCH_4 = 10^{-1}$. The local minimum at $pCH_4 \sim 10^{-3.5}$ and $pCO_2 = 10^{-2}$, the small dependence on CO_2, and the dominating influence of CH_4 expressed in predictions of pC_2H_4 all manifest themselves in model predictions of pC_3H_8.

In our model atmosphere C_2H_6 is present in significantly higher concentrations than either C_2H_4 or C_3H_8. pC_2H_6 values range from $\sim 10^{-8}$ to $\sim 10^{-3.6}$, and all values are orders of magnitude greater than the other hydrocarbon mixing ratios at the same pCO_2 and pCH_4. CO_2 concentrations have almost no effect on pC_2H_6 when $pCO_2 > 10^{-2}$, but have a moderate negative relationship when $pCO_2 > 10^{-2}$. In this region of the graph changes are similar to those in predicted for the 555nm haze optical depth (τ_{555}), suggesting either a common chemical control on pC_2H_6 and organic haze production or shielding of pC_2H_6 from UV photolysis by the haze.

4.3.2 Hydrocarbon Profiles

In order to look at the hydrocarbon chemistry in more detail, we plotted vertical profiles of H_2, CO, CH_4, C_2H_2, C_2H_4, C_2H_6, and C_3H_8 for two sets of conditions: pCO_2 = 10^{-2}, pCH_4 = 10^{-3}; and pCO_2 10^{-3}, pCH_4 = 10^{-3} (Figure **4-2**). The contours in Figure 4-1 indicate that hydrocarbon concentrations are lower for the pCO_2 = 10^{-2} run, and the differences in the profile plots offer an explanation. Hydrocarbon concentrations peak at 60-65 km, the same height range at which CH_4 concentrations decrease. This relationship is consistent with photolysis of CH_4 being the main source of longer chain hydrocarbons: below this altitude low photon fluxes limit hydrocarbon production; above this altitude low CH_4 concentrations limit hydrocarbon production. However, there are some important differences between the two sets of profiles. The most obvious difference is the suppressed hydrocarbon concentrations for the model with pCO_2 = 10^{-2}, in particular for C_2H_6, which consistently decreases with altitude in the pCO_2 = 10^{-2} model but expresses a peak at 65km in the model with pCO_2 = 10^{-3}. The reason for the differences in the hydrocarbon profiles can be explained by differences in the CO mixing ratio profiles. When pCO_2 = 10^{-3} the CO profile follows the H_2 mixing profile closely, but when pCO_2 = 10^{-2}, the CO profile extends to higher concentrations at the same altitudes at which CH_4 concentrations decrease. The increase in CO is approximately the same size as the decrease in CH_4, indicating that the end primary end product of CH_4 photolysis in this run is CO. This increase in CO comes at the expense of hydrocarbons, which can no longer form as their main atmospheric source is now being used for CO production. This ultimate cause of this shift in chemistry is the increased presence of CO_2, which increases

the oxidation state of the atmosphere with respect to CH_4. This relationship is less important than the availability of CH_4 for photolysis, but is still important enough to have a significant effect on hydrocarbon chemistry.

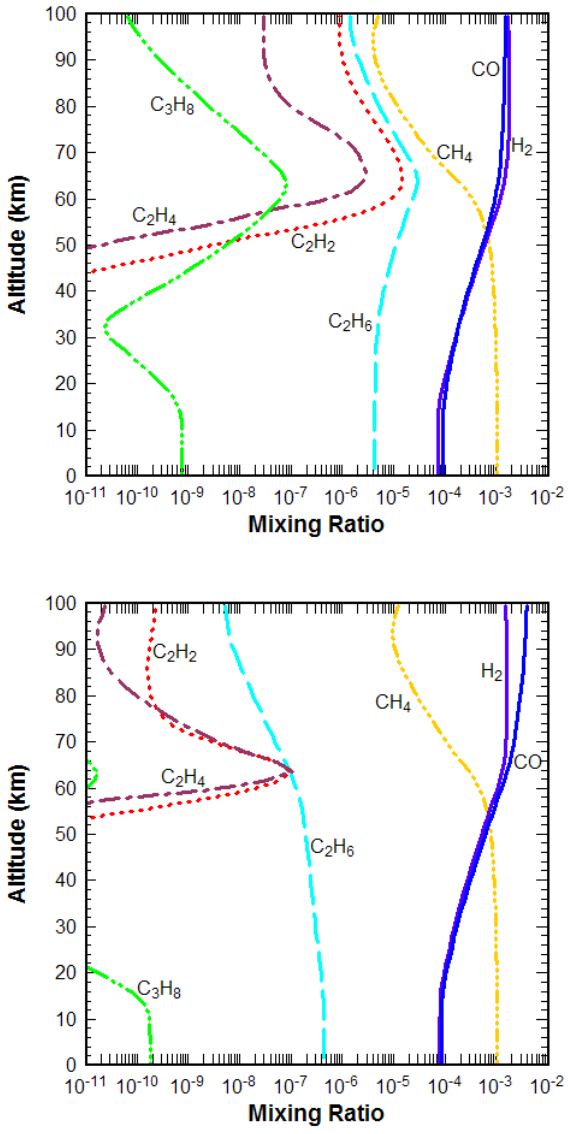

Figure 4-2: Model predictions of vertical profiles of CO, H_2, CH_4, C_2H_2, C_2H_4, C_2H_6, and C_3H_8 at $pCO_2 = 10^{-3}$ (top) and $pCO_2 = 10^{-2}$ (bottom). Both plots are for $pCH_4 = 10^{-3}$. The top set of profiles exhibit higher hydrocarbon concentrations, and the lower set shows CO enrichment at the altitudes for which CH_4 photolysis rates peak.

4.3.3 Haze Optical Depth

The oxidation effects of CO_2 discussed above are a primary control on the abundance of organic haze particles. The contribution of organic haze to optical depth at 555nm (τ_{555}) is plotted as a function of log(pCH_4) and log(pCO_2) in Figure 4-3, which shows the most important control on τ_{555} is the CH_4/CO_2 ratio of the atmosphere. This result is consistent with previous atmospheric models of organic haze (PAVLOV et al., 2001a; ZAHNLE, 1986) and laboratory experiments that demonstrate hydrocarbon aerosol production for C/O ≥ 0.6 (TRAINER et al., 2004) rapid aerosol growth for $CH_4 \geq CO_2$ (SCHLESINGER and MILLER, 1983). Those results suggest a linear relationship that appears in our results, albeit in a slightly altered fashion. In our model, there is a rapid increase in haze optical depth within a nearly linear band that lies between pCH_4 ~10^{-4} and pCH_4 ~$10^{-3.5}$ at pCO_2 ~ $10^{-3.5}$ and between $pCH4$ ~10^{-2} and $pCH4$ ~$10^{-1.5}$ at pCO_2 ~ $10^{-0.5}$. Thus, in our model the haze optical depth increases dramatically when log(pCH_4) > ~0.7·log·(pCO_2) – 1.7, which is to say when $pCH_4 > 0.2\cdot(pCO_2)^{0.7}$. This equation is equivalent to $pCH_4 > pCO_2$ when $pCO_2 \sim 5\cdot10^{-4}$, close to the values used in the experimental studies. This equation approximates the region shown in black on Figure 4-3, which is associated with visible optical depths greater than unity and can be considered inaccessible during times when glaciers were absent and the climate was warm.

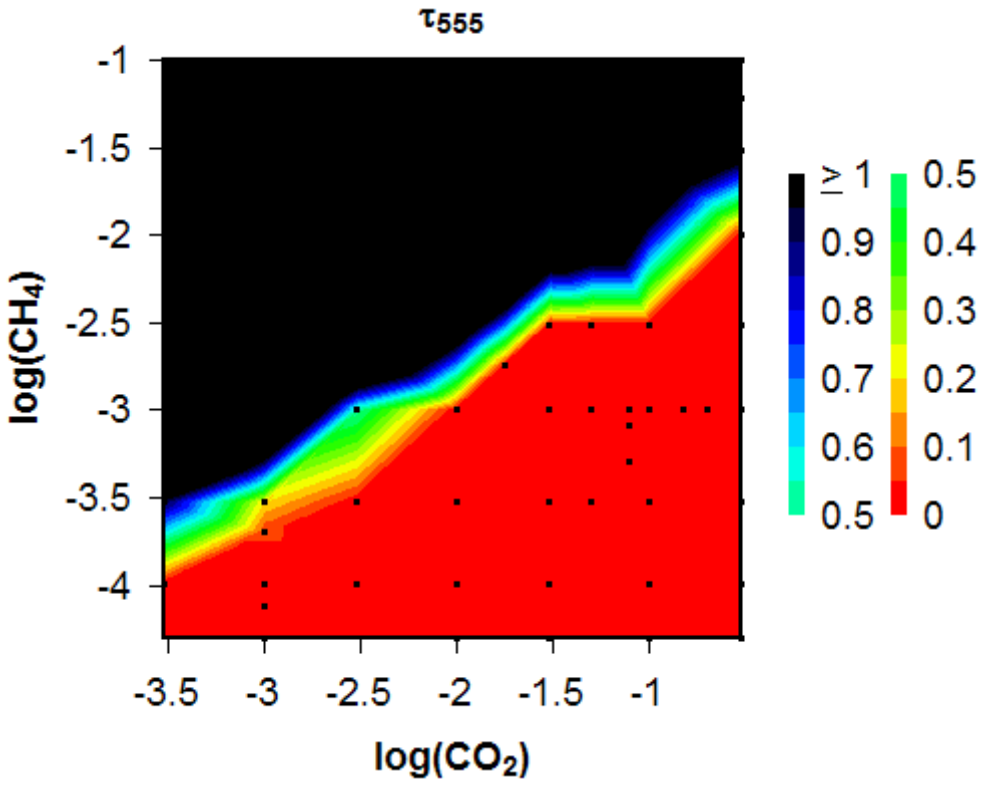

Figure 4-3: Model predictions of 555 nm optical depth (τ_{555}) for various CO_2 and CH_4 mixing ratios. Contours of τ_{555} are plotted vs. log(pCO_2) and log(pCH_4). Values greater than 1 are colored black because these optical depths should cause development of a thick tholin haze that causes glaciations currently thought to be absent prior to 3.0 Ga.

4.4 Discussion

4.4.1 Uncertainties in the Calculations

The errors in determining the atmospheric hydrocarbon gas and aerosol chemistry were discussed in the original publication of the photochemical model (PAVLOV et al., 2001a). The main sources of inaccuracy are: the use of a monodisperse particle size

distribution; the assumption of immediate, irreversible condensation of haze aerosols from C_4H_2 and C_5H_4; the use of a modern eddy diffusion constant despite the possibility that haze could have reduced the degree to which the atmosphere was mixed; and the assumption that hydrogen escape was diffusion-limited regardless of H_2 concentration. These uncertainties may cause specific numerical predictions to be incorrect but the general conclusions should not be changed by any of these potential sources of error, except for errors arising from the treatment of H_2 escape. If H_2 escape was thermally limited, the chemistry of the atmosphere would have been dramatically different and hydrocarbon concentrations would have been significantly higher (TIAN et al., 2005).

4.4.2 Implications for Climate

In order to understand the climatic implications of hydrocarbon chemistry, we must simultaneously consider the influences of gaseous and aerosol species. For $\tau_{555} > 1$, the anti-greenhouse effects of the haze are large and should lead to runaway glaciation. Given the lack of glacial deposits prior to 3.0 Ga, we can assume that $\tau_{555} \leq 1$. The contours in Figure 4-1 are re-plotted in Figure 4-4 with the areas associated with $\tau_{555} > 1$ blacked out. This eliminates the highest concentration regions of all three hydrocarbon plots. The highest concentrations in the accessible regions are found for high CO_2 ($pCO_2 > 10^{-1.5}$) and moderate CH_4 ($10^{-3.5} < pCH_4 < 10^{-2}$). If the paleosol limits on CO_2 are accepted, pCO_2 must have been smaller than ~$10^{-2.5}$-$10^{-3.5}$ (dependent on surface T) and much of this region would be ruled out as well. In that case, gaseous hydrocarbon species will increase as a function of CH_4/CO_2 and act in a manner similar to hydrocarbon

aerosols. This creates the potential for surface temperatures to have both a positive and negative relationship with CH_4/CO_2. When $CH_4/CO_2 < \sim 0.1$, haze thickness will be negligible and increasing this parameter will lead to increased greenhouse forcing from hydrocarbon gases. When $CH_4/CO_2 > \sim 0.1$, the increased anti-greenhouse effects will be significant and increasing this parameter will lead to cooling of the surface.

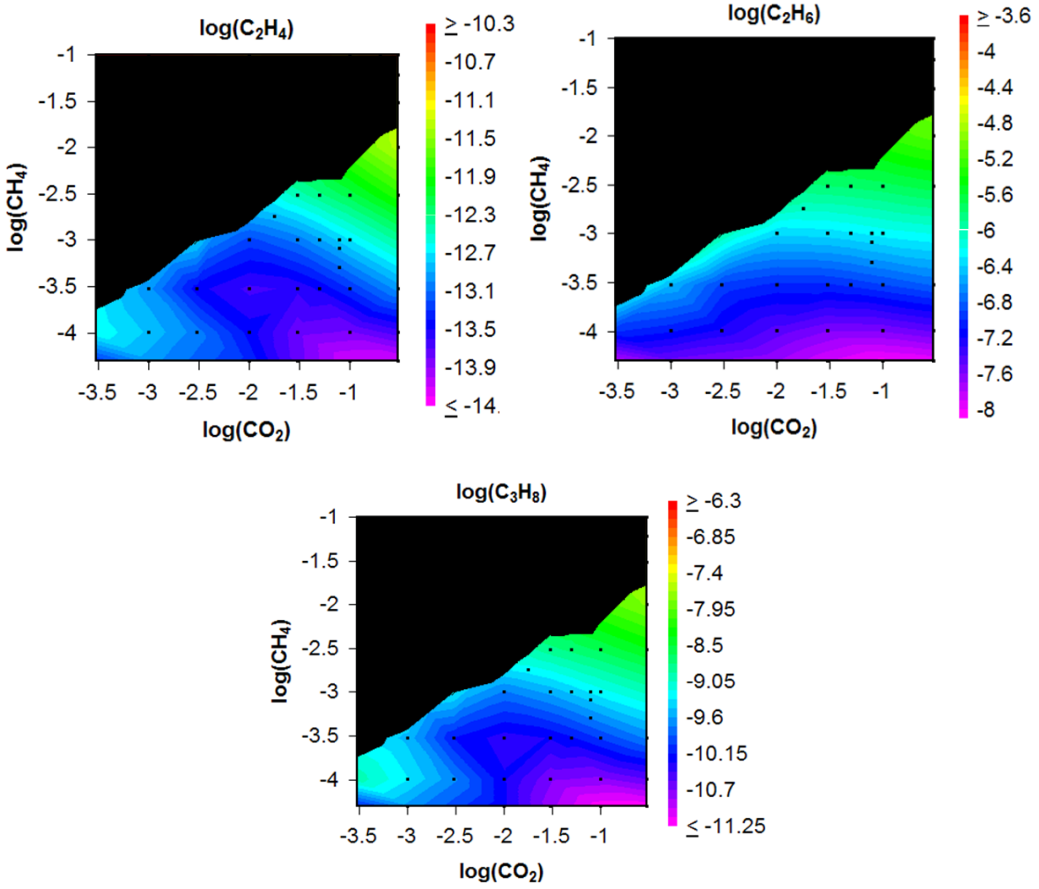

Figure 4-4: Contours of log(pC_2H_4) (top left), log(pC_2H_6) (top right), and log(pC_3H_8) (bottom) plotted as a function of log(pCO_2) (x-axis) and log(pCH_4) (y-axis), as in Figure 4-1. Black regions are considered to be inaccessible due to optical depths greater than unity, as in Figure 4-3. Black dots indicate individual model runs.

4.4.3 Gaian Feedbacks in the Archean

The effects of haze on temperature may have resulted in Gaian feedbacks that would have stabilized climate from the rise of methanogenesis until the rise of atmospheric O_2 (Figure 4-5). After the rise of methanogenesis, increases in surface

temperature should have led to increases in CH_4 flux to the atmosphere, as methanogen production would have increased at higher temperatures. If $CH_4/CO_2 > 0.1$, these increases in CH_4 flux would have caused a larger anti-greenhouse effect and corresponding decreases in surface temperature, thereby offsetting the original temperature rise. This constitutes a negative feedback loop where biological activity is a main component of the system and as such may be considered Gaian (LOVELOCK, 1988). This system would have remained in place until the rise of oxygenic photosynthesis, at which point the influence of surface temperature on CH_4 flux to the atmosphere would have shifted.

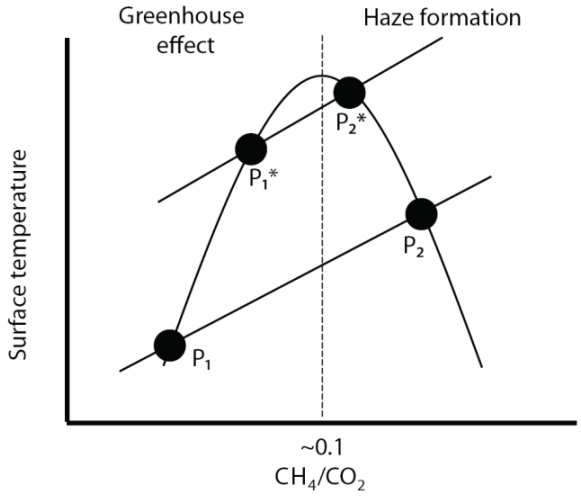

Figure 4-5: (Same as Figure 3-5) Diagram of proposed stable feedbacks for the Archean. The curved line illustrates the effect CH_4/CO_2 has on surface temperature, and the straight lines illustrate the effects of temperature on CH_4/CO_2 before (P_1-P_2) and after (P_1*-P_2*) the rise of methanotrophy. In both cases, increases in temperature should have caused increased biological productivity and higher CH_4 fluxes. At $CH_4/CO_2 > \sim 0.1$, the anti-greenhouse effect is stronger than the greenhouse effect and increases in the CH_4 flux should have caused cooling. Thus, P_2 and P_2* are stable and the system would have settled into a state with an organic haze. The difference between the two stable points is that increased methanotrophy at ~2.7 Ga would have lowered the net biological CH_4 flux, leading to a stable equilibrium point (P_2*) associated with lower CH_4/CO_2 and higher T.

The introduction of oxygenic photosynthesis may have increased the net biological CH_4 flux at a given temperature. After the advent of oxygenic photosynthesis, there would have been more organic material produced in the photic zone, leading to more food for fermentation, acetogenesis, and methanogenesis. Thus, for a given temperature, the net production of CH_4 would increase, pushing the straight line and stable point in Figure 4-5 to the right. This feedback loop would have operated the same way as the pre-oxygenic loop, but would stabilize at higher CH_4 concentrations and lower temperatures.

A forcing may have been acting on this system that eventually led to the rise of atmospheric O_2. After oxygenic photosynthesis was in place, the SO_4^- concentrations in the oceans should have gradually risen. This would have led to a corresponding increase in the activity of SO_4^--reducing methanogens, which combine CH_4 and SO_4^- for energy. As oceanic SO_4^- increased, the CH_4 flux at a given temperature would be brought back down, and the net biological CH_4 flux would be lowered by methanotrophy. This would have pushed the straight line and stable point in Figure 4-5 back to the left. This system would have remained stable until CH_4 dropped below ~ 0.1 times the atmospheric CO_2 concentrations. At that point, the greenhouse effects of CH_4 would be more important than the anti-greenhouse effects of the haze, and further decreases in CH_4 would have caused decreases in temperature, causing further decreases in the biological production of CH_4. Thus, once the system crossed over the hump in Figure 4-5, runaway feedbacks should have severely decreased CH_4 concentrations and average surface temperatures. Claire et al. (2006) argue that the rise of atmospheric O_2 would have only been possible at low CH_4 concentrations. If that were the case, the runaway conditions described above

may have set the stage for the rise of atmospheric O_2 and would have led to the coincidence of that event with global glaciations.

4.4.4 Consistency with Geological Data

While not the sole explanation for the data from this period of geological history, the evolutionary sequence described above is consistent with geochemical and sedimentary records. At 3.4 Ga, tentative evidence for methanogenesis is found in C isotope ratios in fluid inclusions (UENO et al., 2006). The origin of methanogenesis would have initiated the first feedback loop discussed in the last section. The origin of oxygenic photosynthesis would have driven CH_4 production higher due to the greater amount of organic material available for methanogenesis. This would have led to high CH_4 concentrations (PAVLOV et al., 2000) and $CH_4/CO_2 > 0.1$. This implies a haze would have been in place, a phenomenon that can explain an excursion towards low S-MIF between 3.1 and 2.7 Ga (Chapter 3). The stabilization at $CH_4/CO_2 > 0.1$ suggests a cool climate would have been in place, and there is geological evidence for the coincidence of the onset of a cool climate with the presence of oxygenic photosynthesis. The earliest reported glaciations are dated at 2.89 Ga, around the same time the oldest known sterols (whose production may require O_2) and 2-α methyl hopanes (which are only found in the cell walls of cyanobacteria) were deposited (BROCKS et al., 2003; BROCKS et al., 1999; SUMMONS et al., 1999).

The new flux of oxidants to the system would have slowly oxidized the continents, releasing SO_4^- into the oceans. This would have shifted the system's

equilibrium point in the other direction. CH_4/CO_2 values for the new equilibrium point would have been lower, and the organic haze would have thinned. There is a coincidence of events at ~2.8 Ga that can described by this shift in CH_4 chemistry. The low S-MIF excursions and glacial deposits are gone by ~2.7 Ga, Therefore, it is possible that increased methanotrophy caused the changes described in section 4.3, resulting in a thinning of the organic haze, a return of high S-MIF values, and a cessation of anti-greenhouse induced glaciations. The new equilibrium point would have been disrupted by a second set of glaciations associated with an irreversible oxidation of the Earth's atmosphere at ~2.4 Ga that lowered CH_4 concentrations that was possibly triggered when the system was forced into a positive feedback loop (Figure 4-4).

4.5 Conclusions

CH_4 and CO_2 may have significantly impacted climate in indirect ways before the rise of O_2. Both gases act as controls on the concentration of various short-chain volatile hydrocarbons that have absorption features in or near the 8-12 μm window through which most of the Earth's IR energy escapes. These absorption features cause the hydrocarbons to be efficient greenhouse gases so that small concentrations can have large effects on climate. These models predict CH_4 is the main control on the abundance of these species, but CO_2 may be important at low CH_4 concentrations.

CO_2 has a larger influence on organic haze production. Because the primary control on haze production is CH_4/CO_2, changes to the concentration of either gas can influence the thickness of the haze. The haze can absorb and re-radiate incoming solar

radiation and as a result may have a strong cooling effect on the surface. Thus, independent variations of CH_4 and CO_2 may cause decreases in surface temperature when the organic haze is present.

Gaian feedbacks may have stabilized Archean climate on more than one occasion. The negative link between haze thickness and temperature, coupled with the positive link between temperature and CH_4 production, could have stabilized climate between the advent of methanogenesis and the evolution of oxygenic photosynthesis. After this important biological innovation, the climate may have been stabilized by the negative link between temperature and CH_4 flux and the positive relationship between CH_4 concentration and the greenhouse effect. Both these sets of feedbacks are Gaian in nature, as biota would have been taking part in negative feedback cycles that stabilized climate. Analysis of the positioning of stable points in the feedback systems allows for speculation on the co-evolution of Archean climate, biology, and atmospheric chemistry; it is possible that these feedbacks are the explanation for a variety of geochemical phenomena, including the apparent delay in the rise of atmospheric O_2 for ~500 Myr after the rise of oxygenic photosynthesis.

CHAPTER 5

Conclusions and Future Work: Constraining the Archean Biosphere and Climate Using Stable Isotope Measurements

5.1 Introduction

While there are still many mysteries to be worked out regarding the Archean Earth, many of the current data sets can be explained by a single evolutionary history. In Chapters 1-3 of this dissertation, models were presented that describe Fe and S isotope fractionation processes that may have been active in the Archean. Chapter 4 of this thesis used a photochemical code to predict the abundance of climatically important species in parameter space relevant to the Archean. These models, in conjunction with previously reported variations of isotopes in the rock record, can be used to describe the co-evolution of Archean climate, biology, and geochemistry. This Chapter proposes one such evolution sequence, which may not uniquely describe any of these trends but which can account for all of them.

5.2 Stable Isotopes in the Archean Rock Record

5.2.1 δ^{56}Fe record

The Fe isotope composition of shales can be grouped into three distinct stages (ROUXEL et al., 2005): Stage I, prior to 2.3 Ga, contains shales with δ^{56}Fe between -3.5 and +1.0‰; Stage II, from ~2.3 – ~1.8 Ga, contains shales with δ^{56}Fe between -0.3 and

+1.2‰; and Stage III, after 1.5 Ga, contains shales with $\delta^{56}Fe$ between -1.0 and 0‰ (Figure 5-1).

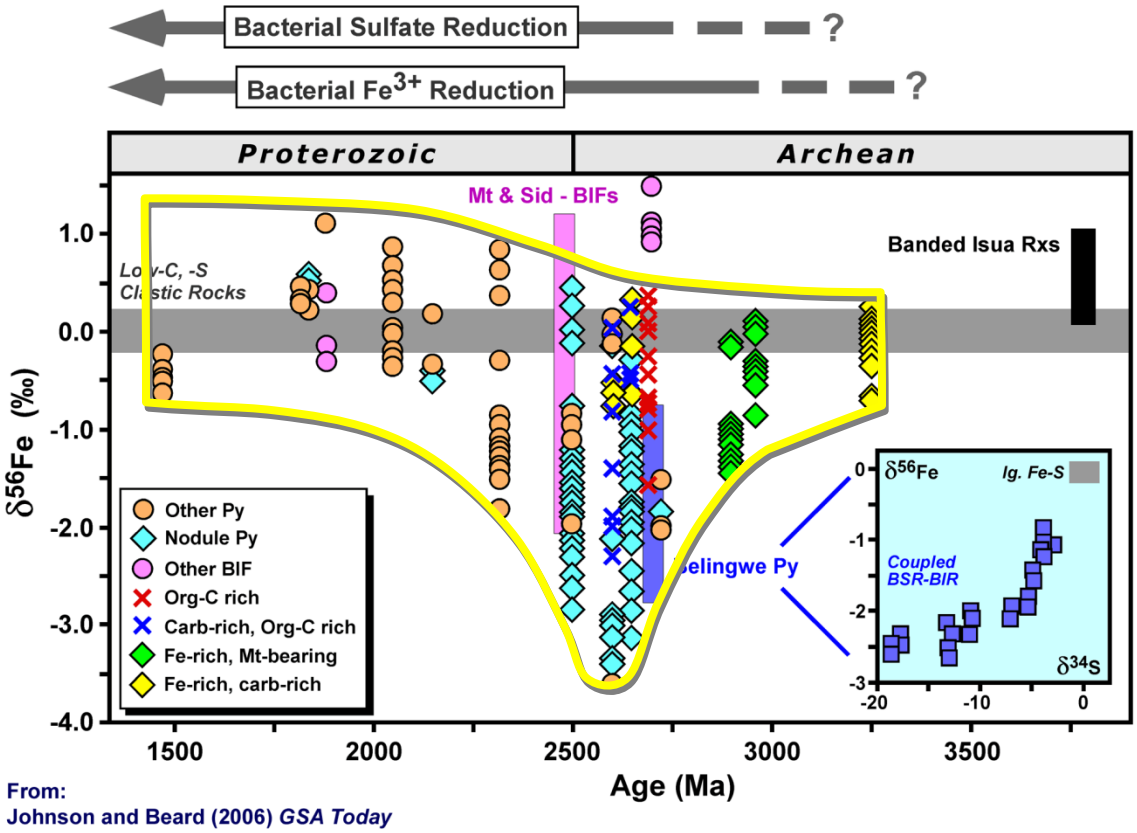

Figure 5-1: Plot of $\delta^{56}Fe$ (‰) of sedimentary rocks plotted against age (Ga), from Johnson and Beard (2006). Fe- and carbonate-rich pyrites are shown with yellow diamonds, Fe-rich pyrites with magnetite are shown with green diamonds, pyrite nodules are shown with blue diamonds, other pyrites are shown with orange circles, organic C- and carbonate-rich whole sediment analyses are respectively shown with red and blue X's, and Fe oxides from banded iron formations are shown with pink circles. The black rectangle at ~3.8 Ga represents analysis of putative BIFs from Isua, and the pink rectangle at ~2.5 Ga represents measurements of reduced Fe in BIFs. The grey rectangle represents the range of basaltic Fe, thought to represent the flux of Fe from the Earth's interior. The yellow outline encapsulates the range of $\delta^{56}Fe$ values in pyrites, for use in Figure 5-5.

The lack of fractionation recorded in shales during Stage III is a result of the quantitative precipitation of Fe(II) in Fe sulfide minerals as Fe enters the oceans at mid-ocean ridges and reacts with H_2S from microbial sulfate reduction. The complete

precipitation of Fe eliminates the possibility for any fractionation to be recorded in the sedimentary record. However, if the oceans had significantly less sulfate, the H_2S flux at mid-ocean ridges would be significantly smaller, and Fe would not be quantitatively precipitated at the ridges. This was likely the case during Stage II, when the oceans were anoxic yet sulfate concentrations were still much lower than today. Incomplete precipitation of Fe in sulfides at hydrothermal vents would have allowed Fe(II) to exhibit fractionation during precipitation. The mobility of Fe could have been further enhanced by anoxic oceans, which would have led to greater amounts of soluble Fe(II), and in turn more potential for Fe isotope fractionation. The positive Fe isotope reservoir during Stage I was Fe-oxides deposited in banded iron formations (BIFs), which have δ^{56}Fe as large as ~1.2‰, significantly greater than the δ^{56}Fe composition of Fe(II) released from modern hydrothermal systems, measured to be -0.30‰ (SHARMA et al., 2001).

Rouxel et al. (2005) attribute the large fractionation between Stage I Fe-oxides and Fe-sulfides to partial oxidation of the oceanic reservoir of Fe(II), precipitation of ^{56}Fe-enriched Fe(III)-oxides, and incorporation of the remaining ^{56}Fe-depleted Fe(II) into Fe-sulfides. The oxidation would result from one of three processes: (1) anoxygenic photosynthesis; (2) reaction with dissolved O_2; or (3) UV-induced photo-oxidation. Laboratory measurements show that anoxygenic photosynthesis causes fractionation of ~1.5‰, similar to the difference between modern hydrothermal Fe and the most ^{56}Fe-enriched Stage I Fe-oxides. Similar experiments on precipitation via reactions of aqueous Fe(II) with O_2 show that fractionations of ~0.8‰ can result; this process is capable of explaining the composition of most of the banded iron formations, particularly if variables such as temperature and precipitation rate are allowed to vary. Regardless of the

pathway for Fe-oxide formation, this model proposes that the Fe-oxides remove ^{56}Fe from the oceanic reservoir, resulting in highly $\delta^{56}Fe$-depleted Stage I pyrites.

Alternatively, the Stage I fractionations could be the result of fractionations during reduction of Fe(III)-oxides by Fe-reducing bacteria (BEARD et al., 2003; YAMAGUCHI et al., 2005). Under this model, Fe(III)-oxide precipitates would form (again, through one of the three aforementioned pathways) and then be depleted of ^{54}Fe by Fe-reducing microbes that use Fe(III) as an electron acceptor in the absence of dissolved O_2. Dissimilatory Fe reduction (Fe reduction for the purposes of energy and not nutrient acquisition) has been measured to result in a kinetic fractionation of $\Delta^{56}Fe_{FeII\text{-}Fe(III)\text{-}oxides}$ of -1.3‰ to -2.6‰ (BEARD et al., 1999; BEARD et al., 2003; JOHNSON et al., 2005). Although this fractionation is not large enough to account for the differences between the most ^{56}Fe-enriched Fe-oxides and the most ^{56}Fe-depleted pyrites, they can explain the differences between the most ^{56}Fe-enriched Fe-oxides and the most ^{56}Fe-enriched pyrites as well as between the most ^{56}Fe-depleted Fe-oxides and the most ^{56}Fe-depleted pyrites, as both reservoirs exhibit a large spread of $\delta^{56}Fe$ values. The wide range of $\delta^{56}Fe$ values in Fe-oxides may be the result of a constant ~1.5‰ fractionation imposed by photosynthesis in waters that are continually depleted in ^{56}Fe as they move away from the source of hydrothermal Fe. This would lead to the wide spread in $\delta^{56}Fe$ found in pyrites, as they could have had values as low as 2.6‰ less than the oxides through which their Fe was cycled.

Both of these models depend on Fe(III) species having a higher $\delta^{56}Fe$ composition than Fe(II) species, and invoke fractionation during formation of Fe-oxides from aqueous

Fe(II), consistent with the models published in Chapters 1 and 2, which show that redox reactions have a greater potential for fractionation than complexation reactions. The fractionation for equilibrium between $Fe(II)_{aq}$ and $Fe(III)_{aq}$ has been measured (WELCH et al., 2003) and predicted (Chapter 1) to be ~3.0‰ at ~20˚C; this fractionation is larger than those required by either model described above. Given that kinetic fractionations can accentuate equilibrium fractionations, at this point both models must be considered feasible.

In order to discriminate between the two theories on Stage I Fe cycling, new work must be done in modeling and measuring Fe isotope fractionations. Given recent advances in Fe isotope measurement, accurate determination of mass-dependent fractionation lines (linear relationships between $\delta^{56}Fe$ and $\delta^{57}Fe$) has become possible. The slopes of these fractionation lines are dependent on the fractionation mechanism, so reactions may be traceable by multiple Fe isotope measurements of natural samples. This may help differentiate between different oxidation pathways in the formation of Stage I Fe-oxides, and may help identify the presence of dissimilatory Fe reduction. This type of analysis is already being developed for the S isotope system, which may provide a useful model for the development of multiple Fe isotope analyses and is a system that has already been used to draw inferences about the rise of atmospheric O_2.

5.2.2 $\Delta^{33}S$ Record

The $\Delta^{33}S$ record has also been divided into three separate stages (FARQUHAR and WING, 2003): Stage I lasts from 3.8 to 2.45 Ga and is characterized by a large spread in

$\Delta^{33}S$ values (up to 10‰); Stage II lasts from 2.45 Ga to 2.0 Ga and is characterized by a small but significant spread in $\Delta^{33}S$ values (magnitudes < 0.5‰); and Stage III runs from 2.0 Ga until the present, and is characterized by insignificant fluctuations in $\Delta^{33}S$ smaller than measurement errors (usually ~0.2‰). These variations in $\Delta^{33}S$ have been attributed to the oxidation of the Earth's atmosphere. $\Delta^{33}S$ has been recreated by photolysis of SO_2 at wavelengths that O_2 and O_3 shield the atmosphere from in the modern environment. Preservation of a $\Delta^{33}S$ signal requires atmospheric S deposition through multiple pathways, and models by Pavlov and Kasting (2002) show that this is only possible when O_2 concentrations are less than 10^{-5} times the present atmospheric level (PAL). More recent work by Zahnle et al. (2006) places an additional constraint on $\Delta^{33}S$ preservation with a time dependent model that only records S_8 deposition when $fCH_4 > 8$ ppm. This places two constraints on the Stage I atmosphere: it must have had at least 8 ppm CH_4 and no more than ~1 ppm O_2. The lower amount of $\Delta^{33}S$ in Stage II sediments is often attributed to dissolution and re-deposition of S deposited during Stage I, with dilution of the strong Stage I $\Delta^{33}S$ signal in the process.

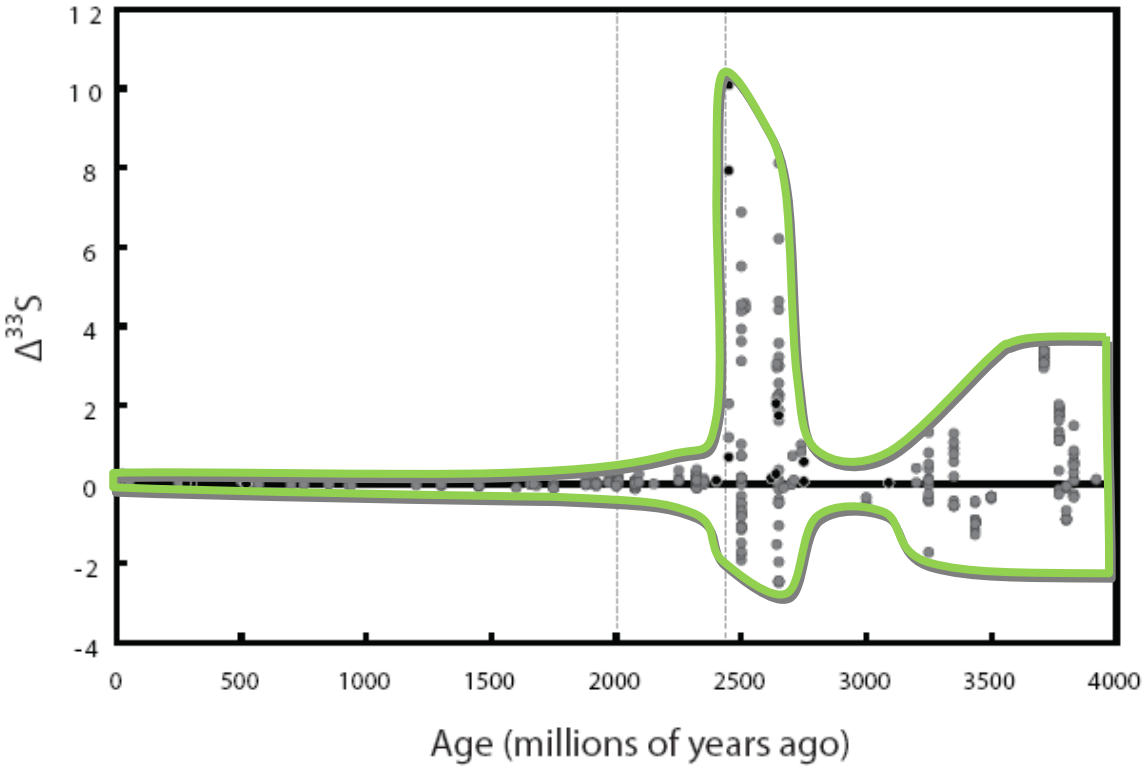

Figure 5-2: A compilation of new (see Table 3-1) and published (FARQUHAR et al., 2002; HU et al., 2003; MOJZSIS et al., 2003; PAPINEAU et al., 2005; WHITEHOUSE et al., 2005) sulfur isotope data. Here, sulfur isotope data ($\Delta^{33}S$) are plotted against age. New data are represented by black-filled circles, and previously published data are plotted in grey-filled circles. The two gray bands at 2.71 Ga and 3.0 Ga show the timing of data from the Kameeldoorns Formation and Witwatersrand Basin, which express $\Delta^{33}S$ between -0.46 and +0.57 ‰ (PETERS et al., 2006). The plot shows wide variations in $\Delta^{33}S$ for late Archean samples (ranging from –2.45 to +10.10 ‰), and a reduced range of $\Delta^{33}S$ between ~3.2 and 2.7 Ga. It also illustrates the significant number of mass dependent samples reported that have an age between 2.7 and 2.45 Ga. The green outline spans $\Delta^{33}S$ values for comparisons to other trends in Figure 5-5.

In Chapter 3, we proposed further subdivision of Stage I into three sub-stages (Section 3.2, Figure 5-2): Stage IA, which runs from ~3.8 Ga to ~3.3 Ga with $-1.8 < \Delta^{33}S < 3.2$; Stage IB, which runs from ~3.2 Ga to ~2.8 with $-0.5 < \Delta^{33}S < 0.5$; and Stage IC, which runs from ~2.7 Ga to 2.45 Ga with $-2 < \Delta^{33}S < 10.1$‰. The large variations seen between stages is largely attributed to the ability of the atmosphere to preserve a S-MIF

signal, but the variations between sub-stages is perhaps best attributed to fluctuations in the ability of the atmosphere to *create* MIF.

Changes to the SO_2 distribution in the atmosphere and the photon flux to the troposphere have the ability to control S-MIF production; these controls are in turn functions of the atmospheric CO_2 and CH_4 concentrations (amongst other factors). For a SO_2 outgassing rate of $3.5 \cdot 10^8$ molecules$\cdot$cm$^{-2}\cdot$s^{-1}, peak S-MIF production is predicted for fCH$_4$ ~ 10^{-3} and fCO$_2$ ~ 10^{-1}. It is not unreasonable to correlate these conditions to the peak S-MIF signal during Stage IC. To explain the lower S-MIF rates during Stage IB, one can change either CO_2 or CH_4 in either direction. Higher CH_4 fluxes may have been present during Stage IB if the division between IB and IC was related to an increase in methanotrophy that occurred around ~2.7 Ga. This is precisely what time-dependent models call for after the rise of oxygenic photosynthesis (CATLING et al., 2007), as the gradual oxidation of the atmosphere would have made increasing amounts of SO_4 available to methanotrophs. Thus, going backwards in time we would expect to see an increase in CH_4 that would have thickened the organic haze and decreased S-MIF production.

If this gradual oxidation was the result of oxygenic photosynthesis, the advent of that metabolism would explain the difference in S-MIF between Stage IB and Stage IA. If methanogenesis was in place when oxygenic photosynthesis evolved – something there is evidence for in the low δ^{13}C values in graphite inclusions (UENO et al., 2006) – the addition of oxygenic photosynthesis should have increased the total productivity of the biosphere (KHARECHA et al., 2005), and the net CH_4 flux to the atmosphere should have risen due to the increased availability of organic carbon for fermentation and acetogen-

consuming methanotrophs (CLAIRE et al., 2006). This would place Stage IA at lower CH_4 concentrations than Stage IB, which also corresponds to higher S-MIF production values.

This analysis of $\Delta^{33}S$ trends gives us a potential evolution of the atmosphere driven by changes to the metabolisms active at the surface. Methanogenesis would have evolved early, by 3.8 Ga, leading to a significant CH_4 flux to the atmosphere. A decrease in CH_4 values would have occurred sometime between 3.3 and 2.9 Ga (a lack of $\Delta^{33}S$ data between these dates prevents better resolution on this event), caused by the evolution of oxygenic photosynthesis. This would have led to a decrease in $\Delta^{33}S$ due to the relatively thick haze caused by higher CH_4/CO_2. Then, as the surface became gradually oxidated, the SO_4 flux to the surface would have increased accordingly. This would have caused corresponding increases in methanogenesis and decreases in the net CH_4 flux from the biosphere. The ultimate result of this was the transition between Stage IB and Stage IC at ~2.7 Ga, when the CH_4 concentrations drop enough to allow for greater SO_2 photolysis. The dramatic climb in $\Delta^{33}S$ could have been a result of the rapid changes to the tropospheric photon flux for small changes to CH_4 levels (Figure 4-3).

5.2.3 $\delta^{34}S$ Record

The sequence of events described in the preceding section is also consistent with other geochemical data. The $\delta^{34}S$ recorded in sediments expands slightly between 3.0 and 2.5 Ga, and expands further between 2.5 and 2.4 Ga (Figure 5-3). The spread of $\delta^{34}S$ values in the Precambrian has been used as a proxy for SO_4^- concentrations, as sulfate reducing bacteria are known to fractionate S to greater levels in the presence of increased

SO_4^- concentrations. The first expansion is consistent with the small, gradual increase in SO_4^-, proposed above as a driver for increased methanotrophy during this time. Thus, high-resolution determination of this trend should correlate it to the division between Stage IB and Stage IC. The second, greater expansion in $\delta^{34}S$ concentrations would then result from the rise of atmospheric O_2 at 2.45 Ga, made possible by the reduced CH_4 concentrations allowed by the increased SO_4^- to methanotrophs (CATLING et al., 2007).

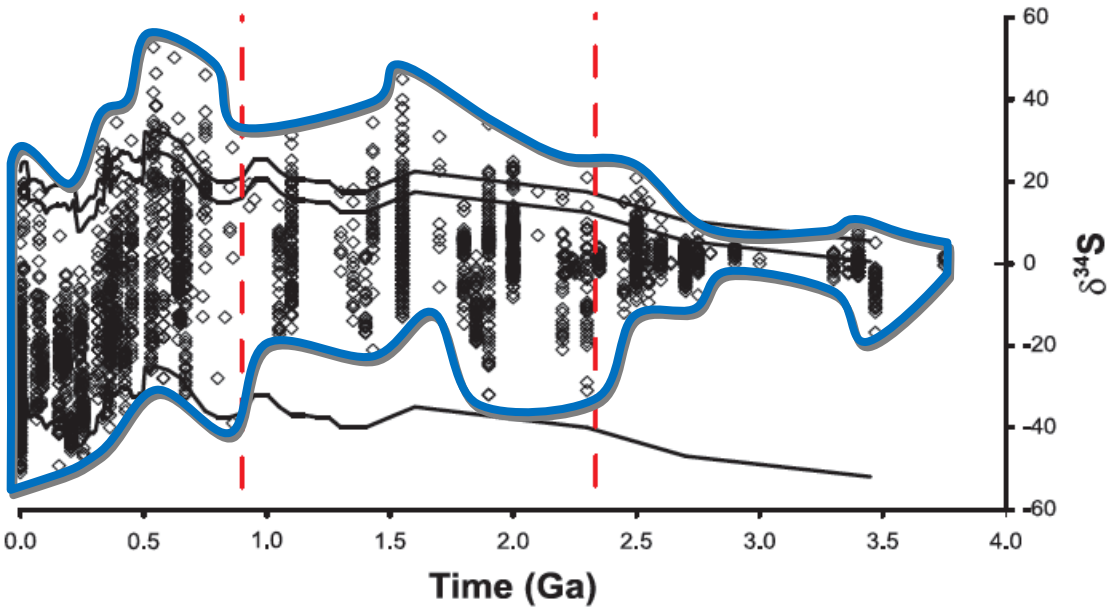

Figure 5-3: Plot of δ34S (‰) of sedimentary sulfides versus age (Ga), from Canfield (2001). The upper lines represent a model for the development of seawater sulfate isotopic compositions. The lower line is offset from the seawater sulfate line by -55‰. The blue outline spans the data for the purposes of inclusion in Figure 5-5.

5.2.4 $\delta^{13}C$ Record

The record of $\delta^{13}C$ values in organic matter is also consistent with an increase in methanotrophy between 2.8 and 2.6 Ga. Indeed, this was the original explanation for the Fortescue excursion (HAYES, 1983; HAYES, 1994), dated at ~2.7 Ga, during which $\delta^{13}C$ values in some organic matter drops to below -50‰ (Figure 5-4), despite relative constant $\delta^{13}C$ in inorganic material. This implies a greater amount of fractionation between the inorganic and organic carbon cycles. These extreme $\delta^{13}C$ values are consistent with C cycled through methanogenesis, which fractionates C by -40‰ with respect to inorganic C, followed by consumption of the ^{13}C-depleted carbon by methanotrophs that cause further isotopic fractionation. Although there are other methods of producing these low $\delta^{13}C$ values, most begin with biologically-produced CH_4. The uncertainty is how the ~-40‰ C in biologically-produced CH_4 is incorporated into insoluble organic material with further ^{13}C depletion. This can be done through two separate pathways: (i) formation of organic haze particles that are then deposited into the oceans as proposed by Pavlov et al. (2001b), or (ii) methanotrophy, as described above and proposed by Hayes (1983; 1994). The latter is supported by the relatively small amounts of methanotroph biomarkers found with respect to abundant cyanobacterial biomarkers found in kerogens contemporaneous with the $\delta^{13}C$ excursion; the former is supported by the $\Delta^{33}S$ and glacial records, which suggest haze thickness peaks before the excursion. Further research is warranted to discriminate between these two pathways for secondary fractionation and deposition. Specifically, experiments should be undertaken to measure ^{13}C-depletion during haze formation. This would then allow atmospheric

models to predict the degree to which atmospheric reactions would eliminate the signature in haze before deposition, and predict the $\delta^{13}C$ of sediments deposited under biospheres with different amounts of methanogenesis and methanotrophy.

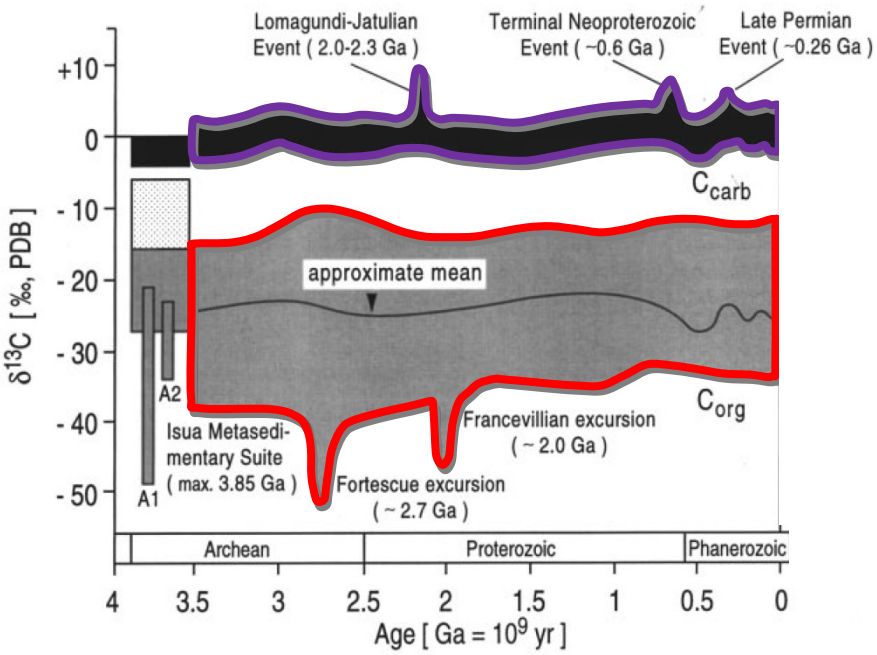

Figure 5-4: Plot of $\delta^{13}C$ (‰) of inorganic carbon (purple, top) and organic carbon (red, bottom) plotted against age (Ga), from Schidlowski (2001). The grey box at ~3.8 Ga represents $\delta^{13}C$ measurements of inclusions in putative banded iron formations. Of particular note is the Fortescue excursion, at ~2.7 Ga, which may have been the result of a consortium of methanogenic, acetogenic, and methanotrophic bacteria. The shaded ranges are outlined in red (C_{org}) and purple (C_{carb}) for comparison with other isotope systems in Figure 5-5.

5.3 Proposed Evolution of the Archean Atmosphere, Biosphere, and Climate

The synthesis of isotopic data and model predictions is shown in Figure 5-5. The right side of the figure, at ~3.8 Ga, corresponds to the earliest sedimentary rocks on Earth. Mojzsis et al. (1996) claim they evidence for life at this time in the form of low-

$\delta^{13}C$ kerogens in graphite inclusions from purported sedimentary rocks on Akilia Island. There is additional evidence for the presence of methanogens by 3.4 Ga, also from $\delta^{13}C$ measurements of rock inclusions (UENO et al., 2006). For the purposes of this discussion, it is assumed that methanogenesis, thought to be evolutionarily ancient (WOESE, 1987), was in place by ~3.8 Ga.

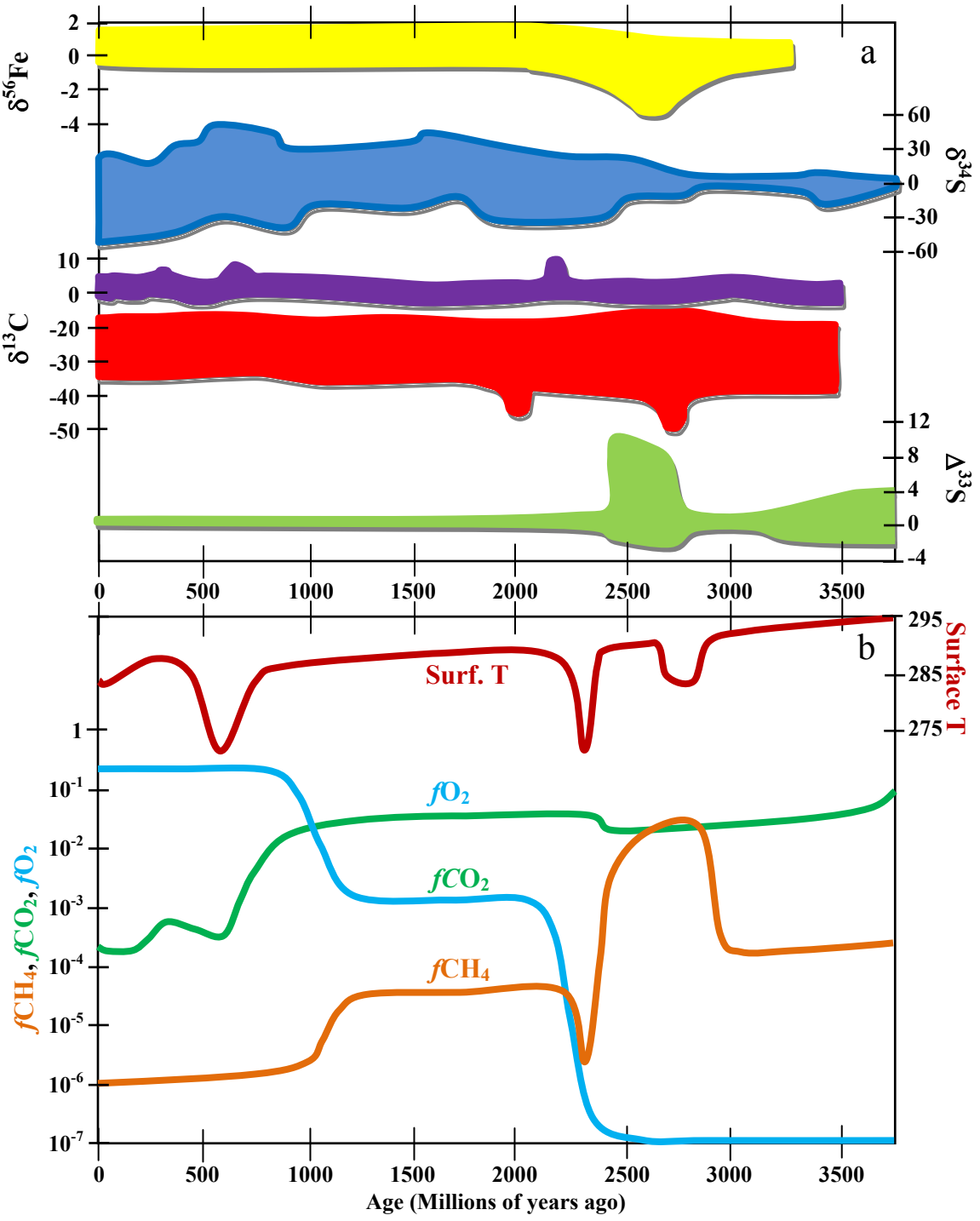

Figure 5-5: (a) Evolution of ranges of $\delta^{56}Fe$ of pyrites (yellow), $\delta^{34}S$ of sedimentary sulfides (blue), $\delta^{13}C$ of carbonates (purple), $\delta^{13}C$ of organic matter (red), and $\Delta^{33}S$ of sediments (green). (b) Evolution of major atmospheric species and surface temperature, derived from consideration of data plotted in (a).

According to Kharecha et al. (2005), a biosphere comprised solely of methanogens would have led to $f\mathrm{CH_4}$ of ~70-350 ppm, depending on the amount of H_2 in the atmosphere. Thus, $f\mathrm{CH_4} \sim 10^{-4}$ at 3.8 Ga. There is no glacial debris in rocks older than 3.0 Ga, although there are not many samples from that time. If the climate was indeed glacier-free, surface temperatures must have been at least a few degrees warmer than they are on the modern Earth. For $f\mathrm{CH_4} \sim 10^{-4}$, a surface temperature of 293K would only be possible if pCO_2 was greater than 0.1 atm. The warm temperatures at this time would have caused increased weathering rates, which in turn would have slowly drawn down CO_2. This would have led to slight decreases to CH_4 and surface T.

The first significant changes to the system would have resulted from the advent of oxygenic photosynthesis. There is evidence for the evolution of this metabolism by ~2.9 Ga from the presence of 2α-methylhopanes in kerogens from rocks of that age (BROCKS et al., 2003; SUMMONS et al., 1999). Oxygenic photosynthesizing bacteria would have dramatically increased the flux of organic material available for acetogens and methanotrophs, and thereby increased the flux of CH_4 to the atmosphere. Therefore, the addition of this metabolism to the biosphere would have led to higher CH_4 concentrations, albeit temporarily (see below). If CH_4 concentrations rose to levels approaching those of CO_2, an organic haze would have formed. The model results presented in Chapter 3 show how such a haze could have decreased the atmospheric production of $\Delta^{33}S$. It is not unreasonable that CH_4 fluxes would have increased by an order of magnitude as a result of the increase in primary productivity (KHARECHA et al., 2005). According to the model results in Chapter 3, for $f\mathrm{CH_4} \sim 10^{-1.8}$ and $f\mathrm{CO_2} \sim 10^{-1.1}$, the number of S-MIF-producing reactions in the atmosphere would have been reduced by

a factor of ~3. Extrapolations based on climate models that use the photochemical results from Chapter 4 predict that the average surface temperature for these conditions would be ~285-290K, close to modern-day value (HAQQ-MISRA et al., submitted to *Astrobiology*). Thus, this atmospheric composition can also explain the glaciations reported at ~2.9 Ga (CROWELL, 1999; NISBET et al., 1993; YOUNG et al., 1998) that suggest the presence of approximately modern day temperatures.

The advent of oxygenic photosynthesis would have had one more immediate consequence: the gradual increase of oceanic SO_4^- concentrations. The newfound source of oxidants to the system would have caused oxidation of reduced S in sediments, thereby causing an increase in riverine SO_4^- flux. In turn, this would have allowed for increased methanotrophy through sulfate reduction. Evidence for the presence of sulfate reducers at this time is provided by co-variations of Fe and S isotopes from pyrites in the ~2.7 Ga Belingwe Formation {Archer, 2006 #396} and the slight increase in the spread of $\delta^{34}S$ values at the time. Evidence for the presence of methanogens includes the presence of 3β-methylhopanes in kerogens from ~2.7 Ga sediments in the Pilbara Craton (EIGENBRODE et al., 2001), and the decrease in $\delta^{13}C$ values of organic matter in rocks from ~2.8 to ~2.6 Ga. The increase in methanotrophy would have decreased the net flux of CH_4 to the atmosphere, thereby thinning the organic haze established after the advent of oxygenic photosynthesis. Although the change in CH_4 flux may have been gradual, the calculations presented in Chapters 3 and 4 show that small changes in CH_4 concentration can cause dramatic changes to tropospheric chemistry. As a result, the change from glacial, low-$\Delta^{33}S$ conditions to warm, high-$\Delta^{33}S$ conditions could have been rapid. The

photochemical results in Chapters 3 and 4 and recent climate calculations show that an atmospheric composition of $f\mathrm{CH_4} \sim 10^{-2.8}$, $f\mathrm{CO_2} \sim 10^{-1.3}$ would explain both the high $\Delta^{33}\mathrm{S}$ values and the glacier-free climate present between 2.7 and 2.4 Ga.

The changes to the surface environment that occurred at ~2.4 Ga make all previous (and subsequent) changes pale in comparison. At this point, $\mathrm{SO_4^-}$ concentrations had increased enough to prevent $\mathrm{SO_4^-}$ from limiting methanotrophy, as evidenced by the increase in the spread of $\delta^{34}\mathrm{S}$ values at 2.4 Ga. This would have led to a dramatic decrease in $\mathrm{CH_4}$ concentrations, thereby plummeting temperatures and triggering the global glaciations at the time (BEKKER et al., 2005; ROSCOE, 1969). Photochemical calculations show this would have set the stage for the rise of $\mathrm{O_2}$, something only possible when $\mathrm{CH_4}$ concentrations were low. As a result of the higher $\mathrm{O_2}$ concentrations, the geochemistry of the surface would have been drastically altered. For example, the $\Delta^{33}\mathrm{S}$ signature would have collapsed as the $\mathrm{O_2/O_3}$ shield decreased S-MIF production and increased redox reactions decreased S-MIF preservation. For related reasons, $\mathrm{CH_4}$ concentrations would have recovered, albeit to lower levels: $\mathrm{O_2}$ and $\mathrm{O_3}$ would have shielded $\mathrm{CH_4}$ from UV photolysis, but the recovery of $\mathrm{CH_4}$ would have been incomplete because of larger oxidative sinks. The partial recovery of $\mathrm{CH_4}$ would have allowed surface temperatures to recover, leading to a stable, oxidized surface environment. Over time, the oceans would have become oxidized. As a result, Fe solubility would have decreased, causing a decrease in the flux of Fe to the surface where it could be fractionated (Section 5.2.1). Thus, regardless of the fractionation mechanism, $\delta^{56}\mathrm{Fe}$ should have been limited as Fe concentrations dropped. A number of other changes to the

bulk chemistry in the sedimentary record also resulted, providing abundant evidence for this oxidation event (HOLLAND, 1984).

5.4 Future Work

While the above story is a self-consistent way of describing the available geochemical data, there are potential problems with it. The $\Delta^{33}S$ predictions in Chapter 3 and the climate calculations that depend on the organic photochemistry in Chapter 4 are both functions of a potentially over-simplified treatment of organic haze particles. Currently, the code has one size particle at each altitude, whereas an actual atmosphere would have a distribution of particle sizes. The treatment haze formation chemistry may also be inaccurate, and haze formation pathways (and haze optical properties) are based on an atmosphere with far less O atoms and oxidizing radicals than would have been present in an Archean atmosphere. Fortunately, laboratory experiments have commenced that examine the haze formation rates and optical properties under potential Archean atmospheres (TRAINER et al., 2004; TRAINER et al., 2006).

There are also holes in our knowledge of many of the isotopic systems used to derive this evolution sequence. Despite the efforts at predictions of S-MIF production and preservation, no theoretical study has incorporated both aspects of $\Delta^{33}S$ chemistry because production could not be quantified in terms of $\Delta^{33}S$. The reason for this is there is no published first-principles description of S-MIF formation processes, even though certain reactions have been identified as a prerequisite for the signal. However, Lyons (2006) has proposed self-shielding similar to the type that creates MIF of O in interstellar

clouds (LYONS and YOUNG, 2005) may be the cause of Archean S-MIF. If this is the case, it may be possible to quantify the $\Delta^{33}S$ created on the atmospheric level, and track its preservation using the same photochemical code used by Pavlov and Kasting (2002) to measure preservation.

Similar problems exist with the $\delta^{56}Fe$ record. Pyrite formation is a major control on Fe isotope cycling throughout Earth history, yet one of the unknowns in the Fe isotope systematics is the amount of fractionation during formation of pyrite. Because the Fe isotopic composition of pyrite is what defines the different Stages in the history of Fe isotopes, and because of the influence pyrite formation has on the source of Fe to the Earth's oceans, understanding fractionation during this pyrite formation is crucial to understanding the Fe cycling of sediments of all ages. While fractionation during formation of FeS has been measured (BUTLER et al., 2005), the fractionation during formation of pyrite from FeS is still unknown. However, it may be possible to model this important reaction through use of periodic calculations such as VASP (Vienna Ab-initio Simulation Package). If that can be done, models of the Archean oceans can be created that include isotopic fractionations. Then, predictions can be made for the amount of $\delta^{56}Fe$ for different biospheres, Fe fluxes, and oceanic redox conditions.

REFERENCES

Accelrys I. (2003) Cerius2.

Albrecht-Gary A. M. and Crumbliss A. L. (1998) Coordination chemistry of siderophores: Thermodynamics and kinetics of iron chelation and release. In *Metal Ions in Biological Systems, Vol 35*, pp. 239-327.

Anbar A. D. (2004) Iron stable isotopes: beyond biosignatures. *Earth and Planetary Science Letters* **217**(3-4), 223-236.

Anbar A. D., Jarzecki A. A., and Spiro T. G. (2005) Theoretical investigation of iron isotope fractionation between Fe(H2O)(3+)(6) and Fe(H2O)(2+)(6) : Implications for iron stable isotope geochemistry. *Geochimica Et Cosmochimica Acta* **69**(4), 825-837.

Anbar A. D., Roe J. E., and Nealson K. H. (2000) Nonbiological fractionation of iron isotopes. *Science* **288**(5463), 126-128.

Anderegg G., Leplatte.F, and Schwarzenbach G. (1963) Hydroxamatkomplexe .3. Eisen(Iii)-Austausch Zwischen Sideraminen Und Komplexonen - Diskussion Der Bildungskonstanten Der Hydroxamatkomplexe. *Helvetica Chimica Acta* **46**(4), 1409-&.

Arthur M. A. M. (2000) *Volcanic contributions to the carbon and sulfur geochemical cycles and global change. Encyclopedia of volcanoes*.

Barreto W. J., Barreto S. R. G., Ponzoni S., Kawano Y., Di Mauro E., Magosso H. A., and Silva W. P. (2005) Preparation and characterization of a stable semiquinone-iron complex. *Monatshefte Fur Chemie* **136**(5), 701-712.

Battistuzzi F. U., Feijao A., and Hedges S. B. (2004) A genomic timescale of prokaryote evolution: insights into the origin of methanogenesis, phototrophy, and the colonization of land. *Bmc Evolutionary Biology* **4**.

Beard B. L. and Johnson C. M. (1999) High precision iron isotope measurements of terrestrial and lunar materials. *Geochimica Et Cosmochimica Acta* **63**(11-12), 1653-1660.

Beard B. L. and Johnson C. M. (2004) Fe isotope variations in the modern and ancient earth and other planetary bodies. In *Geochemistry of Non-Traditional Stable Isotopes*, Vol. 55, pp. 319-357.

Beard B. L. and Johnson C. M. (2005) Inter-mineral Fe isotope variations in mantle-derived rocks and implications for the Fe geochemical cycle (vol 68, pg 4727, 2004). *Geochimica Et Cosmochimica Acta* **69**(21), 5161-5161.

Beard B. L., Johnson C. M., Cox L., Sun H., Nealson K. H., and Aguilar C. (1999) Iron isotope biosignatures. *Science* **285**(5435), 1889-1892.

Beard B. L., Johnson C. M., Von Damm K. L., and Poulson R. L. (2003) Iron isotope constraints on Fe cycling and mass balance in oxygenated Earth oceans. *Geology* **31**(7), 629-632.

Becke A. D. (1997) Density-functional thermochemistry .5. Systematic optimization of exchange-correlation functionals. *Journal of Chemical Physics* **107**(20), 8554-8560.

Bekker A., Holland H. D., Wang P. L., Rumble D., Stein H. J., Hannah J. L., Coetzee L. L., and Beukes N. J. (2004) Dating the rise of atmospheric oxygen. *Nature* **427**(6970), 117-120.

Bekker A., Kaufman A. J., Karhu J. A., and Eriksson K. A. (2005) Evidence for Paleoproterozoic cap carbonates in North America. *Precambrian Research* **137**(3-4), 167-206.

Berresheim H. and Jaeschke W. (1983) The Contribution of Volcanos to the Global Atmospheric Sulfur Budget. *Journal of Geophysical Research-Oceans and Atmospheres* **88**(NC6), 3732-3740.

Best S. P., Armstrong R. S., and Beattie J. K. (1980) Infrared Metal-Ligand Vibrations of Hexaaquametal(III) Ions in Alums. *Inorganic Chemistry* **19**(7), 1958-1961.

Best S. P., Beattie J. K., and Armstrong R. S. (1984) Vibrational Spectroscopic Studies of Trivalent Hexa-Aqua-Cations - Single-Crystal Raman-Spectra between 275 and 1200 cm-1 of the Cesium Alums of Titanium, Vanadium, Chromium, Iron, Gallium, and Indium. *Journal of the Chemical Society-Dalton Transactions*(12), 2611-2624.

Binkley J. S., Pople J. A., and Hehre W. J. (1980) Self-Consistent Molecular-Orbital Methods .21. Small Split-Valence Basis-Sets for 1st-Row Elements. *Journal of the American Chemical Society* **102**(3), 939-947.

Binning R. C. and Curtiss L. A. (1990) Compact Contracted Basis-Sets for 3rd-Row Atoms - Ga-Kr. *Journal of Computational Chemistry* **11**(10), 1206-1216.

Blaudeau J. P., McGrath M. P., Curtiss L. A., and Radom L. (1997) Extension of Gaussian-2 (G2) theory to molecules containing third-row atoms K and Ca. *Journal of Chemical Physics* **107**(13), 5016-5021.

Bluth G. J. S., Schnetzler C. C., Krueger A. J., and Walter L. S. (1993) The Contribution of Explosive Volcanism to Global Atmospheric Sulfur-Dioxide Concentrations. *Nature* **366**(6453), 327-329.

Borgias B., Hugi A. D., and Raymond K. N. (1989) Isomerization and Solution Structures of Desferrioxamine-B Complexes of Al-3+ and Ga-3+1. *Inorganic Chemistry* **28**(18), 3538-3545.

Boukhalfa H. and Crumbliss A. L. (2002) Chemical aspects of siderophore mediated iron transport. *Biometals* **15**(4), 325-339.

Brantley S. L., Liermann L., and Bullen T. D. (2001) Fractionation of Fe isotopes by soil microbes and organic acids. *Geology* **29**(6), 535-538.

Brantley S. L., Liermann L. J., Guynn R. L., Anbar A., Icopini G. A., and Barling J. (2004) Fe isotopic fractionation during mineral dissolution with and without bacteria. *Geochimica Et Cosmochimica Acta* **68**(15), 3189-3204.

Brocks J. J., Buick R., Logan G. A., and Summons R. E. (2003) Composition and syngeneity of molecular fossils from the 2.78 to 2.45 billion-year-old Mount Bruce Supergroup, Pilbara Craton, Western Australia. *Geochimica Et Cosmochimica Acta* **67**(22), 4289-4319.

Brocks J. J., Logan G. A., Buick R., and Summons R. E. (1999) Archean molecular fossils and the early rise of eukaryotes. *Science* **285**(5430), 1033-1036.

Burdett J. W., Arthur M. A., and Richardson M. (1989) A Neogene Seawater Sulfur Isotope Age Curve from Calcareous Pelagic Microfossils. *Earth and Planetary Science Letters* **94**(3-4), 189-198.

Butler I. B., Archer C., Vance D., Oldroyd A., and Rickard D. (2005) Fe isotope fractionation on FeS formation in ambient aqueous solution. *Earth and Planetary Science Letters* **236**(1-2), 430-442.

Cances E., Mennucci B., and Tomasi J. (1997) A new integral equation formalism for the polarizable continuum model: Theoretical background and applications to isotropic and anisotropic dielectrics. *Journal of Chemical Physics* **107**(8), 3032-3041.

Canfield D. E. (2001) Biogeochemistry of sulfur isotopes. *Rev. Mineral. Geochem* **43**, 607-636.

Canfield D. E. (2005) The early history of atmospheric oxygen: Homage to Robert A. Garrels. *Annual Review of Earth and Planetary Sciences* **33**, 1-36.

Carpenter J. E. and Weinhold F. (1988) Analysis of the Geometry of the Hydroxymethyl Radical by the Different Hybrids for Different Spins Natural Bond Orbital Procedure. *Theochem-Journal of Molecular Structure* **46**, 41-62.

Catling D. C., Claire M. W., and Zahnle K. J. (2007) Anaerobic methanotrophy and the rise of atmospheric oxygen. *Philosophical Transactions of the Royal Society A: Mathematical, Physical and Engineering Sciences* **365**(1856), 1867-1888.

Catling D. C., Zahnle K. J., and McKay C. P. (2001) Biogenic methane, hydrogen escape, and the irreversible oxidation of early Earth. *Science* **293**(5531), 839-843.

Cheah S. F., Kraemer S. M., Cervini-Silva J., and Sposito G. (2003) Steady-state dissolution kinetics of goethite in the presence of desferrioxamine B and oxalate ligands: implications for the microbial acquisition of iron. *Chemical Geology* **198**(1-2), 63-75.

Claire M. W., Catling D. C., and Zahnle K. J. (2006) Biogeochemical modelling of the rise in atmospheric oxygen. *Geobiology* **4**(4), 239-269.

Claypool G. E., Leventhal J. S., and Goldhaber M. B. (1980) Geochemical Effects of Early Diagenesis of Organic-Matter, Sulfur, and Trace-Elements in Devonian Black Shales, Appalachian Basin. *Aapg Bulletin-American Association of Petroleum Geologists* **64**(5), 692-692.

Cloud P. (1972) Working Model of Primitive Earth. *American Journal of Science* **272**(6), 537-548.

Croal L. R., Johnson C. M., Beard B. L., and Newman D. K. (2004) Iron isotope fractionation by Fe(II)-oxidizing photoautotrophic bacteria. *Geochimica Et Cosmochimica Acta* **68**(6), 1227-1242.

Crosby H. A., Johnson C. M., Roden E. E., and Beard B. L. (2005) Coupled Fe(II)-Fe(III) electron and atom exchange as a mechanism for Fe isotope fractionation during dissimilatory iron oxide reduction. *Environmental Science & Technology* **39**(17), 6698-6704.

Crowell J. C. (1999) Pre-Mesozoic ice ages; their bearing on understanding the climate system *Memoir - Geological Society of America* **192**(106).

Crumbliss A. L. (1991) Aqueous solution equilibrium and kinetic studies of iron siderophore and model siderophore complexes. In *CRC Handbook of Microbial Iron Chelates* (ed. G. Winkelmann), pp. 177–235. CRC Press.

Cundari T. R. and Stevens W. J. (1993) Effective Core Potential Methods for the Lanthanides. *Journal of Chemical Physics* **98**(7), 5555-5565.

Dauphas N. and Rouxel O. (2006) Mass spectrometry and natural variations of iron isotopes. *Mass Spectrometry Reviews* **25**(4), 515-550.

Dhungana S., White P. S., and Crumbliss A. L. (2001) Crystal structure of ferrioxamine B: a comparative analysis and implications for molecular recognition. *Journal of Biological Inorganic Chemistry* **6**(8), 810-818.

Ditchfield R., Hehre W. J., and Pople J. (1971) *A. J. Chem. Phys.* **54**, 724

Dobbs K. D. and Hehre W. J. (1986) Molecular-Orbital Theory of the Properties of Inorganic and Organometallic Compounds 4 - Extended Basis-Sets for 3rd-Row and 4th-Row, Main-Group Elements. *Journal of Computational Chemistry* **7**(3), 359-378.

Dobbs K. D. and Hehre W. J. (1987a) Molecular-Orbital Theory of the Properties of Inorganic and Organometallic Compounds .5. Extended Basis-Sets for 1st-Row Transition-Metals. *Journal of Computational Chemistry* **8**(6), 861-879.

Dobbs K. D. and Hehre W. J. (1987b) Molecular-Orbital Theory of the Properties of Inorganic and Organometallic Compounds .6. Extended Basis-Sets for 2nd-Row Transition-Metals. *Journal of Computational Chemistry* **8**(6), 880-893.

Edwards D. C., Nielsen S. B., Jarzecki A. A., Spiro T. G., and Myneni S. C. B. (2005) Experimental and theoretical vibrational spectroscopy studies of acetohydroxamic acid and desferrioxamine B in aqueous solution: Effects of pH and iron complexation. *Geochimica Et Cosmochimica Acta* **69**(13), 3237-3248.

Eigenbrode J. L., Freeman K. H., Brocks J. J., Summons R. E., and Logan G. A. (2001) Late Archean Biomarkers of Carbonate and Shale Lithologies from the Hamersley Basin, Pilbara Craton, Western Australia. *Eleventh Annual V. M. Goldschmidt Conference*, 3461.

Evers A., Hancock R. D., Martell A. E., and Motekaitis R. J. (1989) Metal-Ion Recognition in Ligands with Negatively Charged Oxygen Donor Groups - Complexation of Fe(Iii), Ga(Iii), in(Iii), Al(Iii), and Other Highly Charged Metal-Ions. *Inorganic Chemistry* **28**(11), 2189-2195.

Farquhar J., Bao H. M., and Thiemens M. (2000) Atmospheric influence of Earth's earliest sulfur cycle. *Science* **289**(5480), 756-758.

Farquhar J., Savarino J., Airieau S., and Thiemens M. H. (2001) Observation of wavelength-sensitive mass-independent sulfur isotope effects during SO2 photolysis: Implications for the early atmosphere. *Journal of Geophysical Research-Planets* **106**(E12), 32829-32839.

Farquhar J. and Wing B. A. (2003) Multiple sulfur isotopes and the evolution of the atmosphere. *Earth and Planetary Science Letters* **213**(1-2), 1-13.

Farquhar J., Wing B. A., McKeegan K. D., Harris J. W., Cartigny P., and Thiemens M. H. (2002) Mass-independent sulfur of inclusions in diamond and sulfur recycling on early earth. *Science* **298**(5602), 2369-2372.

Forrest J. and Newman L. (1977) Ag-110 Microgram Sulfate Analysis for Short Time Resolution of Ambient Levels of Sulfur Aerosol. *Analytical Chemistry* **49**(11), 1579-1584.

Foster J. P. and Weinhold F. (1980) Natural Hybrid Orbitals. *Journal of the American Chemical Society* **102**(24), 7211-7218.

Francl M. M., Pietro W. J., Hehre W. J., Binkley J. S., Gordon M. S., Defrees D. J., and Pople J. A. (1982) Self-Consistent Molecular-Orbital Methods .23. a Polarization-Type Basis Set for 2nd-Row Elements. *Journal of Chemical Physics* **77**(7), 3654-3665.

Frisch M. J., Trucks G. W., Schlegel H. B., Scuseria G. E., Robb M. A., Cheeseman J. R., Montgomery J., J. A., Vreven T., Kudin K. N., Burant J. C., Millam J. M., Iyengar S. S., Tomasi J., Barone V., Mennucci B., Cossi M., Scalmani G., Rega N., Petersson G. A., Nakatsuji H., Hada M., Ehara M., Toyota K., Fukuda R., Hasegawa J., Ishida M., Nakajima T., Honda Y., Kitao O., Nakai H., Klene M., Li X., Knox J. E., Hratchian H. P., Cross J. B., Bakken V., Adamo C., Jaramillo J., Gomperts R., Stratmann R. E., Yazyev O., Austin A. J., Cammi R., Pomelli C., Ochterski J. W., Ayala P. Y., Morokuma K., Voth G. A., Salvador P., Dannenberg J. J., Zakrzewski V. G., Dapprich S., Daniels A. D., Strain M. C., Farkas O., Malick D. K., Rabuck A. D., Raghavachari K., Foresman J. B., Ortiz J. V., Cui Q., Baboul A. G., Clifford S., Cioslowski J., Stefanov B. B., Liu G., Liashenko A., Piskorz P., Komaromi I., Martin R. L., Fox D. J., Keith T., Al-Laham M. A., Peng C. Y., Nanayakkara A., Challacombe M., Gill P. M. W., Johnson B., Chen W., Wong M. W., Gonzalez C., and Pople J. A. (2004) Gaussian 03, Revision C.02. CT.

Goldblatt C., Lenton T. M., and Watson A. J. (2006) Bistability of atmospheric oxygen and the Great Oxidation. *Nature* **443**(7112), 683-686.

Gordon M. S. (1980) The Isomers of Silacyclopropane. *Chemical Physics Letters* **76**(1), 163-168.

Gordon M. S., Binkley J. S., Pople J. A., Pietro W. J., and Hehre W. J. (1982) Self-Consistent Molecular-Orbital Methods .22. Small Split-Valence Basis-Sets for 2nd-Row Elements. *Journal of the American Chemical Society* **104**(10), 2797-2803.

Graf H. F., Feichter J., and Langmann B. (1997) Volcanic sulfur emissions: Estimates of source strength and its contribution to the global sulfate distribution. *Journal of Geophysical Research-Atmospheres* **102**(D9), 10727-10738.

Habicht K. S., Gade M., Thamdrup B., Berg P., and Canfield D. E. (2002) Calibration of sulfate levels in the Archean Ocean. *Science* **298**(5602), 2372-2374.

Hariharan P. C. and Pople J. A. (1972) Effect of D-Functions on Molecular-Orbital Energies for Hydrocarbons. *Chemical Physics Letters* **16**(2), 217.

Hariharan P. C. and Pople J. A. (1973) Influence of Polarization Functions on Molecular-Orbital Hydrogenation Energies. *Theoretica Chimica Acta* **28**(3), 213-222.

Hay P. J. and Wadt W. R. (1985) Abinitio Effective Core Potentials for Molecular Calculations - Potentials for the Transition-Metal Atoms Sc to Hg. *Journal of Chemical Physics* **82**(1), 270-283.

Hayes J. M. (1983) Geochemical evidence bearing on the origin of aerobiosis, a speculative hypothesis (ed. J. W. Schopf), pp. 291-301. Princeton Univ. Press.

Hayes J. M. (1994) *Global methanotrophy at the Archean-Preoterozoic transition*. Columbia University Press.

Hehre W. J., Radom L., Schleyer P. V., and Pople J. (1985) *Ab initio molecular orbital theory*. John Wiley & Sons.

Hernlem B. J., Vane L. M., and Sayles G. D. (1996) Stability constants for complexes of the siderophore desferrioxamine B with selected heavy metal cations. *Inorganica Chimica Acta* **244**(2), 179-184.

Hinrichs K. U. (2001) An era of methanotrophy at 2.7 Gyr--a reassessment of the mechanism. *Eleventh Annual V. M. Goldschmidt Conference*.

Holland H. D. (1984) *The Chemical Evolution of the Atmosphere and Oceans*. Princeton University Press.

Holland H. D. (1994) Early Proterozoic atmospheric change. Early Life on Earth. In *Early Life on Earth: Nobel Symposium no. 84* (ed. S. Bengtson), pp. 237-244. Columbia University Press.

Holmen B. A. and Casey W. H. (1996) Hydroxamate ligands, surface chemistry, and the mechanism of ligand-promoted dissolution of goethite alpha-FeOOH(s). *Geochimica Et Cosmochimica Acta* **60**(22), 4403-4416.

Holmen B. A., TejedorTejedor M. I., and Casey W. H. (1997) Hydroxamate complexes in solution and at the goethite-water interface: A cylindrical internal reflection Fourier transform infrared spectroscopy study. *Langmuir* **13**(8), 2197-2206.

Hu G. X., Rumble D., and Wang P. L. (2003) An ultraviolet laser microprobe for the in situ analysis of multisulfur isotopes and its use in measuring Archean sulfur isotope mass-independent anomalies. *Geochimica Et Cosmochimica Acta* **67**(17), 3101-3118.

Icopini G. A., Anbar A. D., Ruebush S. S., Tien M., and Brantley S. L. (2004) Iron isotope fractionation during microbial reduction of iron: The importance of adsorption. *Geology* **32**(3), 205-208.

Jaber M., Bertin F., and Thomasdavid G. (1980) Application of Infrared and Raman Spectrometry to Study on Complexes in Aqueous-Solution - Fe(III)-H2C2O4. *Canadian Journal of Chemistry-Revue Canadienne De Chimie* **58**(12), 1220-1228.

Jarzecki A. A., Anbar A. D., and Spiro T. G. (2004) DFT analysis of Fe(H2O)(6)(3+) and Fe(H2O)(6)(2+) structure and vibrations; implications for isotope fractionation. *Journal of Physical Chemistry A* **108**(14), 2726-2732.

Johnson C. M. and Beard B. L. (2006) Stable isotope geochemistry of transitional elements provides new insights into biogeochemical cycles: Examples from the Fe isotope system. *GSA Today* **16**(11), 4–10.

Johnson C. M., Beard B. L., Roden E. E., Newman D. K., and Nealson K. H. (2004) Isotopic constraints on biogeochemical cycling of Fe. In *Geochemistry of Non-Traditional Stable Isotopes*, Vol. 55, pp. 359-408.

Johnson C. M., Roden E. E., Welch S. A., and Beard B. L. (2005) Experimental constraints on Fe isotope fractionation during magnetite and Fe carbonate

formation coupled to dissimilatory hydrous ferric oxide reduction. *Geochimica Et Cosmochimica Acta* **69**(4), 963-993.

Johnston D. T., Wing B. A., Farquhar J., Kaufman A. J., Strauss H., Lyons T. W., Kah L. C., and Canfield D. E. (2005) Active microbial sulfur disproportionation in the Mesoproterozoic. *Science* **310**(5753), 1477-1479.

Kasting J. F. (1993) Earths Early Atmosphere. *Science* **259**(5097), 920-926.

Kasting J. F. (2006) Earth sciences - Ups and downs of ancient oxygen. *Nature* **443**(7112), 643-645.

Kasting J. F. and Howard M. T. (2006) Atmospheric composition and climate on the early Earth. *Philosophical Transactions of the Royal Society B-Biological Sciences* **361**(1474), 1733-1741.

Kasting J. F., Howard M. T., Wallmann K., Veizer J., Shields G., and Jaffres J. (2006) Paleoclimates, ocean depth, and the oxygen isotopic composition of seawater. *Earth and Planetary Science Letters* **252**(1-2), 82-93.

Kasting J. F., Zahnle K. J., and Walker J. C. G. (1983) Photochemistry of Methane in the Earths Early Atmosphere. *Precambrian Research* **20**(2-4), 121-148.

Kharecha P., Kasting J. F., and Siefert J. L. (2005) A coupled atmosphere-ecosystem model of the early Archean Earth. *Geobiology* **3**, 53-76.

Kiss T. and Farkas E. (1998) Metal-binding ability of desferrioxamine B. *Journal of Inclusion Phenomena and Molecular Recognition in Chemistry* **32**(2-3), 385-403.

Knauth L. P. and Lowe D. R. (2003) High Archean climatic temperature inferred from oxygen isotope geochemistry of cherts in the 3.5 Ga Swaziland Supergroup, South Africa. *Geological Society of America Bulletin* **115**(5), 566-580.

Koch W. and Holthausen M. C. (2000) A Chemist's Guide to Density Functional Theory. Wiley-VCH.

Krishnan R., Binkley J. S., Seeger R., and Pople J. A. (1980) Self-Consistent Molecular-Orbital Methods .20. Basis Set for Correlated Wave-Functions. *Journal of Chemical Physics* **72**(1), 650-654.

Kubicki J. D., Sykes D., and Rossman G. R. (1993) Calculated Trends of Oh Infrared Stretching Vibrations with Composition and Structure in Aluminosilicate Molecules. *Physics and Chemistry of Minerals* **20**(6), 425-432.

Kurzak B., Kozlowski H., and Farkas E. (1992) Hydroxamic and Aminohydroxamic Acids and Their Complexes with Metal-Ions. *Coordination Chemistry Reviews* **114**(2), 169-200.

Lee C. T., Yang W. T., and Parr R. G. (1988) Development of the Colle-Salvetti Correlation-Energy Formula into a Functional of the Electron-Density. *Physical Review B* **37**(2), 785-789.

Leong J. and Raymond N. (1975) Coordination Isomers of Biological Iron Transport Compounds .4. Geometrical Isomers of Chromic Desferriferrioxamine-B. *Journal of the American Chemical Society* **97**(2), 293-296.

Lovelock J. E. (1988) *The Ages of Gaia: A Biography of Our Living Earth*. W.W. Norton & Company, Inc.

Lyons J. R. (2006) Gas-phase Mechanisms of Sulfur Isotope Mass-independent Fractionation. *American Geophysical Union*(2006 Fall Meeting), abstract #V11C-0599.

Lyons J. R. and Young E. D. (2005) CO self-shielding as the origin of oxygen isotope anomalies in the early solar nebula. *Nature* **435**(7040), 317-20.

Massie S. T. and Hunten D. M. (1981) Stratospheric Eddy Diffusion-Coefficients from Tracer Data. *Journal of Geophysical Research-Oceans and Atmospheres* **86**(NC10), 9859-9868.

Matthews A., Morgans-Bell H. S., Emmanuel S., Jenkyns H. C., Erel Y., and Halicz L. (2004) Controls on iron-isotope fractionation in organic-rich sediments (Kimmeridge Clay, Upper Jurassic, southern England). *Geochimica Et Cosmochimica Acta* **68**(14), 3107-3123.

McKay C. P., Pollack J. B., and Courtin R. (1991) The Greenhouse and Antigreenhouse Effects on Titan. *Science* **253**(5024), 1118-1121.

McLean A. D. and Chandler G. S. (1980) Contracted Gaussian-Basis Sets for Molecular Calculations .1. 2nd Row Atoms, Z=11-18. *Journal of Chemical Physics* **72**(10), 5639-5648.

Mojzsis S. J., Arrhenius G., McKeegan K. D., Harrison T. M., Nutman A. P., and Friend C. R. L. (1996) Evidence for life on Earth before 3,800 million years ago. *Nature* **384**(6604), 55-59.

Mojzsis S. J., Coath C. D., Greenwood J. P., McKeegan K. D., and Harrison T. M. (2003) Mass-independent isotope effects in Archean (2.5 to 3.8 Ga) sedimentary sulfides determined by ion microprobe analysis. *Geochimica Et Cosmochimica Acta* **67**(9), 1635-1658.

Mojzsis S. J., Harrison T. M., and Pidgeon R. T. (2001) Oxygen-isotope evidence from ancient zircons for liquid water at the Earth's surface 4,300 Myr ago. *Nature* **409**(6817), 178-181.

Newman M. J. and Rood R. T. (1977) Implications of Solar Evolution for Earths Early Atmosphere. *Science* **198**(4321), 1035-1037.

Nisbet E. G., Bickle M. J., Martin A., and Orpen J. L. (1993) Sedimentology of the Brooklands Formation, Zimbabwe; development of an Archaean greenstone belt in a rifted graben. *Special Publication - Geological Society of Zimbabwe* **2**, 87-120.

NIST. (1998) NIST Critically Selected Stability Constants of Metal Complexes Database (ed. U. S. D. o. Commerce.).

Ohmoto H., Watanabe Y., and Ikemi H. (2005) The absence of mass independent fractionation of sulfur isotopes in Archean sedimentary rocks: An insignificant phenomenon? *Geochimica Et Cosmochimica Acta* **69**(10), A450-A450.

Ohmoto H., Watanabe Y., Ikemi H., Poulson S. R., and Taylor B. E. (2006) Sulphur isotope evidence for an oxic Archaean atmosphere. *Nature* **442**(7105), 908-911.

Ohmoto H., Watanabe Y., and Kumazawa K. (2004) Evidence from massive siderite beds for a CO2-rich atmosphere before, 1.8 billion years ago. *Nature* **429**(6990), 395-399.

Ohrstrom L. and Michaud-Soret I. (1999) Fe-catecholate and Fe-oxalate vibrations and isotopic substitution shifts from DFT quantum chemistry. *Journal of Physical Chemistry A* **103**(2), 256-264.

Ono S., Beukes N. J., Rumble D., and Fogel M. L. (2006a) Early evolution of atmospheric oxygen from multiple-sulfur and carbon isotope records of the 2.9 Ga

Mozaan Group of the Pongola Supergroup, Southern Africa. *South African Journal of Geology* **109**(1-2), 97-108.

Ono S., Eigenbrode J. L., Pavlov A. A., Kharecha P., Rumble D., Kasting J. F., and Freeman K. H. (2003) New insights into Archean sulfur cycle from mass-independent sulfur isotope records from the Hamersley Basin, Australia. *Earth and Planetary Science Letters* **213**(1-2), 15-30.

Ono S., Wing B., Johnston D., Farquhar J., and Rumble D. (2006b) Mass-dependent fractionation of quadruple stable sulfur isotope system as a new tracer of sulfur biogeochemical cycles. *Geochimica Et Cosmochimica Acta* **70**, 2238-2252.

Papineau D., Mojzsis S. J., Coath C. D., Karhu J. A., and McKeegan K. D. (2005) Multiple sulfur isotopes of sulfides from sediments in the aftermath of Paleoproterozoic glaciations. *Geochimica Et Cosmochimica Acta* **69**(21), 5033-5060.

Papineau D., Mojzsis S. J., and Schmitt A. K. (2007) Multiple sulfur isotopes from Paleoproterozoic Huronian interglacial sediments and the rise of atmospheric oxygen. *Earth and Planetary Science Letters* **255**(1-2), 188-212.

Pavlov A. A., Brown L. L., and Kasting J. F. (2001a) UV shielding of NH3 and O-2 by organic hazes in the Archean atmosphere. *Journal of Geophysical Research-Planets* **106**(E10), 23267-23287.

Pavlov A. A., Hurtgen M. T., Kasting J. F., and Arthur M. A. (2003) Methane-rich Proterozoic atmosphere? *Geology* **31**(1), 87-90.

Pavlov A. A. and Kasting J. F. (2002) Mass-independent fractionation of sulfur isotopes in Archean sediments: Strong evidence for an anoxic Archean atmosphere. *Astrobiology* **2**(1), 27-41.

Pavlov A. A., Kasting J. F., Brown L. L., Rages K. A., and Freedman R. (2000) Greenhouse warming by CH4 in the atmosphere of early Earth. *Journal of Geophysical Research-Planets* **105**(E5), 11981-11990.

Pavlov A. A., Kasting J. F., Eigenbrode J. L., and Freeman K. H. (2001b) Organic haze in Earth's early atmosphere: Source of low-C-13 Late Archean kerogens? *Geology* **29**(11), 1003-1006.

Peters M., Farquhar J., and H. S. (2006) Mass Independent Fractionation of Sulphur Isotopes in Precambrian Sedimentary Rocks: Indicator for Changes in Atmospheric Composition and the Operation of the Global Sulphur Cycle. *Eos Trans. AGU* **86**(52), Fall Meeting Suppl., Abstract PP41D-07.

Phillips G. N., Law J. D. M., and Myers R. E. (2001) Is the redox state of the Archean atmosphere constrained? *SEG Newsletter* **47**, 1.

Pietro W. J., Francl M. M., Hehre W. J., Defrees D. J., Pople J. A., and Binkley J. S. (1982) Self-Consistent Molecular-Orbital Methods .24. Supplemented Small Split-Valence Basis-Sets for 2nd-Row Elements. *Journal of the American Chemical Society* **104**(19), 5039-5048.

Polyakov V. B. (1997) Equilibrium fractionation of the iron isotopes: Estimation from Mossbauer spectroscopy data. *Geochimica Et Cosmochimica Acta* **61**(19), 4213-4217.

Polyakov V. B. and Mineev S. D. (1999) Mossbauer spectroscopy as applied to isotopic geochemistry: I. Equilibrium fractionation of iron isotopes. *Geokhimiya*(8), 858-870.

Polyakov V. B. and Mineev S. D. (2000) The use of Mossbauer spectroscopy in stable isotope geochemistry. *Geochimica Et Cosmochimica Acta* **64**(5), 849-865.

Rappe A. K., Casewit C. J., Colwell K. S., Goddard W. A., and Skiff W. M. (1992) UFF, a Full Periodic-Table Force-Field for Molecular Mechanics and Molecular-Dynamics Simulations. *Journal of the American Chemical Society* **114**(25), 10024-10035.

Rappe A. K. and Goddard W. A. (1991) Charge Equilibration for Molecular-Dynamics Simulations. *Journal of Physical Chemistry* **95**(8), 3358-3363.

Rassolov V. A., Pople J. A., Ratner M. A., and Windus T. L. (1998) 6-31G* basis set for atoms K through Zn. *Journal of Chemical Physics* **109**(4), 1223-1229.

Rassolov V. A., Ratner M. A., Pople J. A., Redfern P. C., and Curtiss L. A. (2001) 6-31G*basis set for third-row atoms. *Journal of Computational Chemistry* **22**(9), 976-984.

Redlich O. (1935) A general relationship between the oscillation frequency of isotropic molecules - (with remarks on the calculation of harmonious force constants). *Zeitschrift Fur Physikalische Chemie-Abteilung B-Chemie Der Elementarprozesse Aufbau Der Materie* **28**(5), 371-382.

Reed A. E. and Clark T. (1988) A Natural Bond Orbital Analysis of the Bonding in Solvated Electrons within a Localized Electron Model. *Faraday Discussions*, 365-372.

Reed A. E. and Weinhold F. (1983) Natural Bond Orbital Analysis of near-Hartree-Fock Water Dimer. *Journal of Chemical Physics* **78**(6), 4066-4073.

Reed A. E., Weinstock R. B., and Weinhold F. (1985) Natural-Population Analysis. *Journal of Chemical Physics* **83**(2), 735-746.

Roscoe S. M. (1969) Huronian rocks and uraniferous conglomerates in the Canadian Shield. *Geological Survey of Canada*.

Rouxel O. J., Bekker A., and Edwards K. J. (2005) Iron isotope constraints on the Archean and Paleoproterozoic ocean redox state. *Science* **307**(5712), 1088-1091.

Rye R., Kuo P. H., and Holland H. D. (1995) Atmospheric Carbon-Dioxide Concentrations before 2.2-Billion Years Ago. *Nature* **378**(6557), 603-605.

Sagan C. and Chyba C. (1997) The early faint sun paradox: Organic shielding of ultraviolet-labile greenhouse gases. *Science* **276**(5316), 1217-1221.

Schaftenaar G. and Noordik J. H. (2000) Molden: a pre- and post-processing program for molecular and electronic structures. *J. Comput.-Aided Mol. Design* **14** 123-134.

Schauble E. A. (2004) Applying stable isotope fractionation theory to new systems. In *Geochemistry of Non-Traditional Stable Isotopes*, Vol. 55, pp. 65-111.

Schauble E. A., Rossman G. R., and Taylor H. P. (2001) Theoretical estimates of equilibrium Fe-isotope fractionations from vibrational spectroscopy. *Geochimica Et Cosmochimica Acta* **65**(15), 2487-2497.

Schidlowski M. (2001) Carbon isotopes as biogeochemical recorders of life over 3.8 Ga of Earth history: evolution of a concept. *Precambrian Research* **106**(1-2), 117–134.

Schidlowski M., Hayes J. M., and Kaplan I. R. (1983) Isotopic inferences of ancient biochemistries; carbon, sulfur, hydrogen, and nitrogen (ed. J. W. Schopf). Princeton Univ. Press.

Schlesinger G. and Miller S. L. (1983) Prebiotic Synthesis in Atmospheres Containing Ch4, Co, and Co2 .2. Hydrogen-Cyanide, Formaldehyde and Ammonia. *Journal of Molecular Evolution* **19**(5), 383-390.

Sharma M., Polizzotto M., and Anbar A. D. (2001) Iron isotopes in hot springs along the Juan de Fuca Ridge. *Earth and Planetary Science Letters* **194**(1-2), 39-51.

Sheldon N. D. (2006) Precambrian paleosols and atmospheric CO2 levels. *Precambrian Research* **147**(1-2), 148-155.

Sima J. and Makanova J. (1997) Photochemistry of iron(III) complexes. *Coordination Chemistry Reviews* **160**, 161-189.

Stephens P. J., Devlin F. J., Chabalowski C. F., and Frisch M. J. (1994) Ab-Initio Calculation of Vibrational Absorption and Circular-Dichroism Spectra Using Density-Functional Force-Fields. *Journal of Physical Chemistry* **98**(45), 11623-11627.

Stevens W. J., Basch H., and Krauss M. (1984) Compact Effective Potentials and Efficient Shared-Exponent Basis-Sets for the 1st-Row and 2nd-Row Atoms. *Journal of Chemical Physics* **81**(12), 6026-6033.

Stevens W. J., Krauss M., Basch H., and Jasien P. G. (1992) Relativistic Compact Effective Potentials and Efficient, Shared-Exponent Basis-Sets for the 3rd-Row, 4th-Row, and 5th-Row Atoms. *Canadian Journal of Chemistry-Revue Canadienne De Chimie* **70**(2), 612-630.

Summons R. E., Jahnke L. L., Hope J. M., and Logan G. A. (1999) 2-Methylhopanoids as biomarkers for cyanobacterial oxygenic photosynthesis. *Nature* **400**(6744), 554-557.

Taylor S. R. and McLennan S. M. (1995) The Geochemical Evolution of the Continental-Crust. *Reviews of Geophysics* **33**(2), 241-265.

Teutsch N., von Gunten U., Porcelli D., Cirpka O. A., and Halliday A. N. (2005) Adsorption as a cause for iron isotope fractionation in reduced groundwater. *Geochimica Et Cosmochimica Acta* **69**(17), 4175-4185.

Tian F., Toon O. B., Pavlov A. A., and De Sterck H. (2005) A hydrogen-rich early Earth atmosphere. *Science* **308**(5724), 1014-1017.

Trainer M. G., Pavlov A. A., Curtis D. B., McKay C. P., Worsnop D. R., Delia A. E., Toohey D. W., Toon O. B., and Tolbert M. A. (2004) Haze aerosols in the atmosphere of early earth: Manna from heaven. *Astrobiology* **4**(4), 409-419.

Trainer M. G., Pavlov A. A., DeWitt H. L., Jimenez J. L., McKay C. P., Toon O. B., and Tolbert M. A. (2006) Organic haze on Titan and the early Earth. *Proceedings of the National Academy of Sciences of the United States of America* **103**(48), 18035-18042.

Ueno Y., Yamada K., Yoshida N., Maruyama S., and Isozaki Y. (2006) Evidence from fluid inclusions for microbial methanogenesis in the early Archaean era. *Nature* **440**(7083), 516-519.

Urey H. C. (1947) The Thermodynamic Properties of Isotopic Substances. *Journal of the Chemical Society*(MAY), 562-581.

Wachters A. J. (1970) Gaussian Basis Set for Molecular Wavefunctions Containing Third-Row Atoms. *Journal of Chemical Physics* **52**(3), 1033-&.

Walker J. C. G. (1977) *Evolution of the Atmosphere*. Macmillan.

Walker J. C. G. and Brimblecombe P. (1985) Iron and Sulfur in the Pre-Biologic Ocean. *Precambrian Research* **28**(3-4), 205-222.

Walker J. C. G., Hays P. B., and Kasting J. F. (1981) A Negative Feedback Mechanism for the Long-Term Stabilization of Earths Surface-Temperature. *Journal of Geophysical Research-Oceans and Atmospheres* **86**(NC10), 9776-9782.

Walker J. C. G., Klein C., Schidlowski M., Schopf J. W., Stevenson D. J., and Walter M. R. (1983) Environmental evolution of the Archean-early Proterozoic Earth (ed. J. W. Schopf). Princeton Univ. Press.

Watanabe Y., Naraoka H., and Ohmoto H. (2006) Mass independent fractionation of sulfur isotopes during thermochemical reduction of native sulfur, sulfite and sulfate by amino acids. *EOS (Joint Assembly Suppl.)* **78**(36), V42A-02.

Watson A. J. and Lovelock J. E. (1983) Biological Homeostasis of the Global Environment - the Parable of Daisyworld. *Tellus Series B-Chemical and Physical Meteorology* **35**(4), 284-289.

Weinhold F. and Landis C. R. (2001) Natural Bond Orbitals and Extenstions of Localized Bonding Concepts. *Chemistry Education: Research and Practice in Europe* **2**(2), 91-104.

Welch S. A., Beard B. L., Johnson C. M., and Braterman P. S. (2003) Kinetic and equilibrium Fe isotope fractionation between aqueous Fe(II) and Fe(III). *Geochimica Et Cosmochimica Acta* **67**(22), 4231-4250.

Whitehouse M. J. and Kamber B. S. (2006) Micro-scale (SIMS) sulphur isotope evidence for late archean rise in shallow oceanic free oxygen. *Geochimica Et Cosmochimica Acta* **70**(18), A699-A699.

Whitehouse M. J., Kamber B. S., Fedo C. M., and Lepland A. (2005) Integrated Pb- and S-isotope investigation of sulphide minerals from the early Archaean of southwest Greenland. *Chemical Geology* **222**(1-2), 112-131.

Wiederhold J. G., Kraemer S. M., Teutsch N., Borer P. M., Halliday A. N., and Kretzschmar R. (2006) Iron isotope fractionation during proton-promoted, ligand-controlled, and reductive dissolution of goethite. *Environmental Science & Technology* **40**(12), 3787-3793.

Wiesli R. A., Beard B. L., and Johnson C. M. (2004) Experimental determination of Fe isotope fractionation between aqueous Fe(II), siderite and "green rust" in abiotic systems. *Chemical Geology* **211**(3-4), 343-362.

Wilson E. B., Decius J. C., and Cross P. C. (1980) *Molecular vibrations: the theory of infrared and Raman vibrational spectra*. Dover Publications.

Woese C. R. (1987) Bacterial Evolution. *Microbiological Reviews* **51**(2), 221-271.

Xue H., Tong K. L., Marck C., Grosjean H., and Wong J. T. F. (2003) Transfer RNA paralogs: evidence for genetic code-amino acid biosynthesis coevolution and an archaeal root of life. *Gene* **310**, 59-66.

Yamaguchi K. E., Johnson C. M., Beard B. L., and Ohmoto H. (2005) Biogeochemical cycling of iron in the Archean-Paleoproterozoic Earth: Constraints from iron

isotope variations in sedimentary rocks from the Kaapvaal and Pilbara Cratons. *Chemical Geology* **218**(1-2), 135-169.

Young G. M., von Brunn V., Gold D. J. C., and Minter W. E. L. (1998) Earth's oldest reported glaciation: Physical and chemical evidence from the Archean Mozaan Group (similar to 2.9 Ga) of South Africa. *Journal of Geology* **106**(5), 523-538.

Zahnle K. J. (1986) Photochemistry of Methane and the Formation of Hydrocyanic Acid (Hcn) in the Earths Early Atmosphere. *Journal of Geophysical Research-Atmospheres* **91**(D2), 2819-2834.

Zahnle K. J., Claire M. W., and Catling D. C. (2006) The loss of mass-independent fractionation in sulfur due to a Palaeoproterozoic collapse of atmospheric methane. *Geobiology* **4**(4), 271–283.

Shawn D. Domagal-Goldman Curriculum Vitae

EDUCATION

Pennsylvania State University, University Park, PA
Ph.D. candidate in Astrobiology and Geosciences, degree expected August 2007

University of Rochester, Rochester, NY
M.S. in Geochemistry, May 2002
Advisor: A.D. Anbar
Master's Paper: *Modeling Net Primary Production in the Archean as a Function of Temperature*

B.S. in Physics, May 2001
Advisor: A.D. Anbar
Senior Thesis: *Using Fe Isotope Ratios in Banded Iron Formations as a Potential Geothermometer*

AWARDS

"Best Post-Comps Talk" Award, 2005 Department of Geosciences Grad. Colloquium

PUBLICATIONS IN PREPARATION

Domagal-Goldman S.D. and J.D. Kubicki. Quantum Mechanical Modeling of Equilibrium Isotope Fractionation of Iron Between Organic and Inorganic Complexes: (submitted to *Geochimica et Cosmochimica Acta*)

Domagal-Goldman S.D., D.T. Johnson, J. Farquhar, and J.F. Kasting. Organic Haze, Glaciations, and Multiple Sulfur Isotopes in the Mid-Archean Era. (submitted to *Earth and Planetary Science Letters*)

Domagal-Goldman S.D., J.D. Kubicki, K.W. Paul, and D.L. Sparks. Molecular Modeling of the Fe(III)-Desferrioxamine B Siderophore Complex – Electronic Structure, IR Vibrational Frequencies, and Equilibrium Fractionation in Solution. (submitted to *Geochimica et Cosmochimica Acta*).

ABSTRACTS & PRESENTATIONS

Goldman, S.D. and Kasting, J.F. Fall 2006 Deines Lecture (S MIF)
Domagal-Goldman, S.D. and Kasting, J.F. 2006 AbSciCon (S MIF) talk
Domagal-Goldman, S.D. and Kubicki, J.D. 2006 AbSciCon (Fe isotopes) talk
Goldman, S.D. and Kasting, J.F. Fall 2005 AGU (S MIF) talk
Goldman S.D., and Kubicki, J.D. Spring 2005 Grad colloquium (Fe isotopes) talk
Goldman S.D., and Kubicki, J.D. 2005 ECSS (Fe isotopes) talk
Goldman S.D., and Kasting, J.F. 2005 NAI General Meeting (U solubility) poster
Goldman S.D., and Kasting, J.F. 2004 Grad colloquium (Fe solubility) poster
Goldman S.D., and Kasting J.F. 2004 AbSciCon (Fe solubility) talk
Goldman S.D., and Kasting J.F. 2004 AbGradCon (Fe stability) poster
Goldman S.D., and Kubicki J.D. 2003 NAI General Meeting (Fe isotopes) poster